UNIVERSITÀ POLITECNICA DELLE MARCHE

FACOLTÀ DI INGEGNERIA

Master's Degree in Biomedical Engineering

Modeling Coronary Artery Resistance for the Numerical Simulation of the Aortic-Root Fluid-Dynamics and Coronary Perfusion

Advisor:

Prof. Gianluca Zitti

Candidate:

Meri Gjika

Co-Advisor:

Prof. Laura Burattini

Dr. Seyyed Mahmoud Mousavi

Academic Year 2023/2024

Abstract

Coronary arteries are vital vessels which provide nutrition and oxygen to the heart muscle. Understanding their function requires the understanding of the fluid dynamics of blood flow within these vessels. The aim of this work is the development of a computational model capable to reproduce correctly the coronary arteries hemodynamics, based on the parameterization of the resistance encountered by flowing blood. To do this, experimental data from an in vitro model of the ascending aortic root are used to obtain the quantitative characterization of the resistance to be implemented in the computational model. To include such characteristics, the 2-element and 3-element Windkessel models are employed to define outflow boundary conditions at the coronaries' outlet.

Initially, the literature research delves into coronary physiology to better understand the anatomical and mechanical properties of the coronary arteries, as well as the normal flow pattern and pressure pattern within them.

Subsequently, it focuses on the modeling methods, exploring various models applied in cardiovascular system, particularly the Windkessel-type models and their implementation in computational fluid dynamics (CFD). The advantage of using these models is their good capability in simulating real phenomenon.

Thereafter, the in vitro model and its data are thoroughly analyzed and the resistance values for the left coronary artery (R_{LCA}) and right coronary artery (R_{RCA}) are estimated in several significant phases of the cardiac cycle. The use of piecewise-constant resistance parameterization in the Windkessel model, considering the mean value of the resistance in R_{LCA} out of the contraction 1.35 mmHg/(ml/min) and during the contraction 2400 mmHg/(ml/min). Instead, a unique mean value of the R_{RCA} during the whole cardiac cycle systole, equal to 2.17 mmHg/(ml/min) can be considered to model the RCA resistance.

To validate the resistance parametrization, the work involved two simulations: one using directly as boundary conditions the experimental data time series, and a second simulation in which for the coronary-arteries flow boundary conditions are estimated using the Windkessel models with the obtained resistance parameters. An optimization process is used to determine the model compliance, not measured experimentally. The results of the simulations shows that the outlet pressure at the coronaries, does not replicate exactly the measured pressure. This because the flow is governed by the pressure gradient and influenced by the modeled resistance.

In spite of these discrepancies, the computational model is capable of modeling accurately some hydrodynamics structure in the Valsalva Sinuses and in the coronary arteries, supporting the use of Windkessel-type boundary conditions, based on pressure measurements.

Content

Introduction

Coronary arteries are the blood vessels that provide oxygen and nutrition to the heart muscle. They originate from the base of the aorta in area called the sinuses of Valsalva. The right coronary artery (RCA) arises from the right sinus of Valsalva and it supplies blood to the right part of the heart (right atrium and right ventricle) and part of the septum, while the left coronary artery (LCA) arises from the left sinus and supplies blood to the left part of the heart. Coronary blood flow is crucial in coronary perfusion, representing only a small fraction of 5% of the total cardiac output, consequently myocardial oxygen consumptions from the heart is notably high. The coronary blood flow both in the LCA and RCA in healthy subject is characterized by a recognizable pattern of a small peak during systole followed by a more pronounced and prolonged peak during diastole (Saldin, 2018).

Cardiovascular diseases, particularly coronary artery disease (CAD), are one the global health challenges, being also one of the primary causes of mortality and morbidity in the world. The well understanding of the complex hemodynamics within the aortic root and coronary arteries is important for better diagnose and treatment of the CAD. For an efficient heart muscle functioning is highly important the well-functioning of the coronaries and their dependance from the aortic root (Taegtmeyer, 2006).

The modelling of the flow pattern and pressure distribution in the coronaries and aortic root can be highly accurate if there is the possibility to represent the resistance that the flow encounters while passing in the coronaries. Therefore, advanced models (lamped parameter models) have been proposed from different authors in literature, these new models include not only coronary artery resistance but also arterial bed compliance, capillaries resistance and intramyocardial pressure present during ventricular contraction in the systolic phase.

The primary objective of this thesis is to develop a computational model that accurately represents the coronary artery resistance and its impact in the aortic root fluid dynamics and coronary perfusion in an in vitro ascending aorta model. By formulating boundary conditions based on an electrical analogical model, synthesizing findings from suitable literature and incorporating experimental data acquired using the laboratory model, this research aim to enable comprehensive simulations using Computational Fluid Dynamics (CFD). Specifically, this work has been oriented toward the determination of the lumped parameters of a Windkessel model based on experimental data, and subsequently evaluate the reliability of this model throughout numerical simulations.

For this goal to be achieved, it is essential to delve deeply in the anatomy and physiology of the cardiovascular system and in particular the coronary artery. It includes the well understanding of the histology and mechanical properties of the coronaries. To better understand the physiological condition of the coronary arteries it is important also to have some hinds in what happens in pathophysiological case, like CAD. Many of the existing models of the coronary arteries represent a pathophysiological condition. Existing methodologies for modelling blood flow within the coronary arteries are fundamental for this research. CFD is one of the most powerful tools for modeling simulating the complex flow pattern such as the one of blood in the cardiovascular system. In CFD details on the fluid dynamics account for factors such as vessel geometry, blood viscosity etc. In the case of this work to represent the coronary circulation was essential the incorporation of electrical models, boundary condition, that represent in an analogues way what happens with the fluid. The combination of the CFD modeling with electrical models provide a comprehensive approach for the study of the coronary arteries behavior.

The experimental data acquired from the in vitro model are useful to understand the accuracy and reliability of the simulated model. A novelty of these experimental is the provision of synchronized measurements of pressure and flow in the coronary arteries, which have not been previously available in literature. The analysis of the obtained results leads in the identification of important factors that influence coronary blood flow and how the aortic root influence it. These experimental data were utilized to determine the resistance parameters for a Windkessel model. For instance, simulations can predict the resistance between LCA and RCA, as well as across different clinical scenarios. Making it possible to give ideas on how the treatments and diagnosis used till now can be optimized and shifted to a more patient specific case.

As it will be described in the sections to follow, the accurate modelling of the coronary artery resistance is crucial in the understanding and simulating of the hemodynamics of the cardiovascular system. This thesis aims to developing a computational model that integrates coronary artery resistance in the context of aortic root fluid behavior and coronary perfusion. By combining the computational simulations with the in vitro experimental data and electrical models in the boundary conditions, the research tries to provide a deeper understating of the coronary hemodynamics.

I Section: The Anatomy and Physiology of the Cardiovascular System

The cardiovascular system, also known as circulatory system, is a crucial organ system responsible for the distribution nutrients, oxygen, metabolic substances, and eliminating metabolic waste from the body. This system has a vital importance for cellular communication and defending the organism against external agents. The cardiovascular system consists of the heart, blood vessels and blood. Hearts responsibility is to pump the blood in a close-loop system constituted by the vessels. This one-way close-loop system ensures that blood flows along specific pathways rather than freely within a cavity.

1.1. The Heart

The heart is the central organ of the cardiovascular system, generating the force necessary to propel the blood through the blood vessels. It is located within the thoracic cavity (chest cavity), specifically in the mediastinum, it is slightly shifted towards the left side of the mediastinum. In males, the heart weights approximately 300 -350 grams, and in females it typically weights around 250 – 300 grams (Saldin, 2018). In Figure 1 is shown the heart in situ.

1.1.1 Heart Anatomy

The heart is enveloped by a double-layered membrane called the pericardium. The pericardium consists of two layers: the outer layer known as the parietal pericardium and the inner layer known as the visceral pericardium. Between these layers lies a thin, transparent fluid called pericardial fluid, which lubricates the parietal pericardium. The lubrification fluid ensures that during the rhythmic beats of the heart within the sac, minimal friction is present (Saldin, 2018).

The forceful propulsion of the blood through the vasculature is made possible by the composition of the heart walls, which are mainly composed of a cardiac muscle, called myocardium. The myocardium cells are known as myocytes or cardiomyocytes. These cardiomyocytes can be grouped into bundles around the heart forming a spiral structure known as the myocardial vortex (Gjika, 2022).

The myocytes can be distinguished in three main types: working myocardium, nodal cells, conduction tissue. Nodal cells, in particular, have the ability to transmit electrical signals. This

property is essential for initiation and coordination of the heart rhythmic contractions, enabling it to function as a pump. The heart also contains supportive structures of collagen and elastic fibers, that together constitute what is known as fibrous skeleton, with function to control the opening and closing of the heart valves (Saldin, 2018) & (Gjika, 2022).

The surface of the heart features several important sulci (furrows) that delineate its various chambers and major blood vessels. Three are the main grooves observed on the heart surface (Klabunde, 2011):

- Atrioventricular Groove (Coronary Sulcus) is the most prominent groove on the heart's surface, encircling the heart like a crown. It contains the coronary blood vessels (left and right coronary artery and their accompanying veins) but also separates the atria from the ventricles.
- Anterior Interventricular Groove (Anterior Interventricular Sulcus) runs in the anterior surface of the heart, providing a boundary between the left and right ventricles.
- Posterior Interventricular Groove (Posterior Interventricular Sulcus) runs in the back surface of the heart, providing a separation between the left and right ventricles.

The septum divides the heart in two halves, right half and left half. It also prevents the blood of the right half from mixing with the one of the left half. Each half of the heart consists of two chambers: an upper chamber called atrium (plural: *atria)* and a lower chamber called ventricle (plural: *ventricles*). The portion of septum that separates the atria is referred as interatrial septum while the portion of the septum separating the ventricles is known as the intraventricular septum. So overall the heart consists of four chambers (Saldin, 2018) & (Stanfield, 2012).

The atrium and ventricle in the left side of the heart make up the left heart while the atrium and ventricle in the right side of the heart make up the right heart. The atria receive the blood that comes from the vasculature, while the ventricles receive blood from the atria and then generate a force required to propel blood away from the heart, through the blood vessels. The right and left heart function as separate pumps, efficiently circulating blood throughout the body (Stanfield, 2012). In Figure 2, an anatomical image of the heart is presented, offering views of the heart's base from both a posterior and posterior-inferior perspective. While Figure 3 displays a plane section of the heart, allowing visualization of the atria, ventricles, and septum (including the interatrial and intraventricular septum).

The blood in the right atrium comes from three main sources: the superior vena cava, inferior vena cava, and the coronary sinus. Due to the possible communication between atria and ventricles, blood from the right atrium reaches the right ventricle passing through the tricuspid valve. Blood is then pumped into the pulmonary artery passing through the pulmonary semilunar valve. Conversely, the left atrium receives the blood from the pulmonary veins (two veins for each lung), which then flows towards the left ventricle through the mitral valve. During ventricular contraction, blood is ejected from the left ventricle into the aorta via the aortic semilunar valve (Stanfield, 2012) & (Saldin, 2018).

The heart valves are mechanical valves, and controlling their opening and closing is crucial for their proper function. Nearby tissues play a significant role in this process. In the ventricles, papillary muscles contract during a ventricular contraction, helping in keeping the valves closed and preventing blood from flowing back into the atria. Additionally, chordae tendineae are present in the ventricles. Their primary role is to prevent valve prolapse and regulate valve opening. Valve behavior during diastole[1] and systole[2] is crucial for the heart's function. During diastole, the AV valves open passively to allow blood flow into the ventricles. About 80% of this flow is passive, while the remaining 20% is due to atrial contraction (atrial kick). During systole, the semilunar valves close to prevent blood from returning to the ventricles, while the AV valves also close to prevent backflow into the atria (Saldin, 2018) & (Stanfield, 2012). Figure 4 provides an anatomical depiction of the heart valves in both systole and diastole.

[1] Diastole refers to the phase of the cardiac cycle when the heart muscle relaxes and refills with blood.
[2] Systole is the phase of the cardiac cycle when the heart muscle contracts, pumping blood out of the chambers and into the arteries.

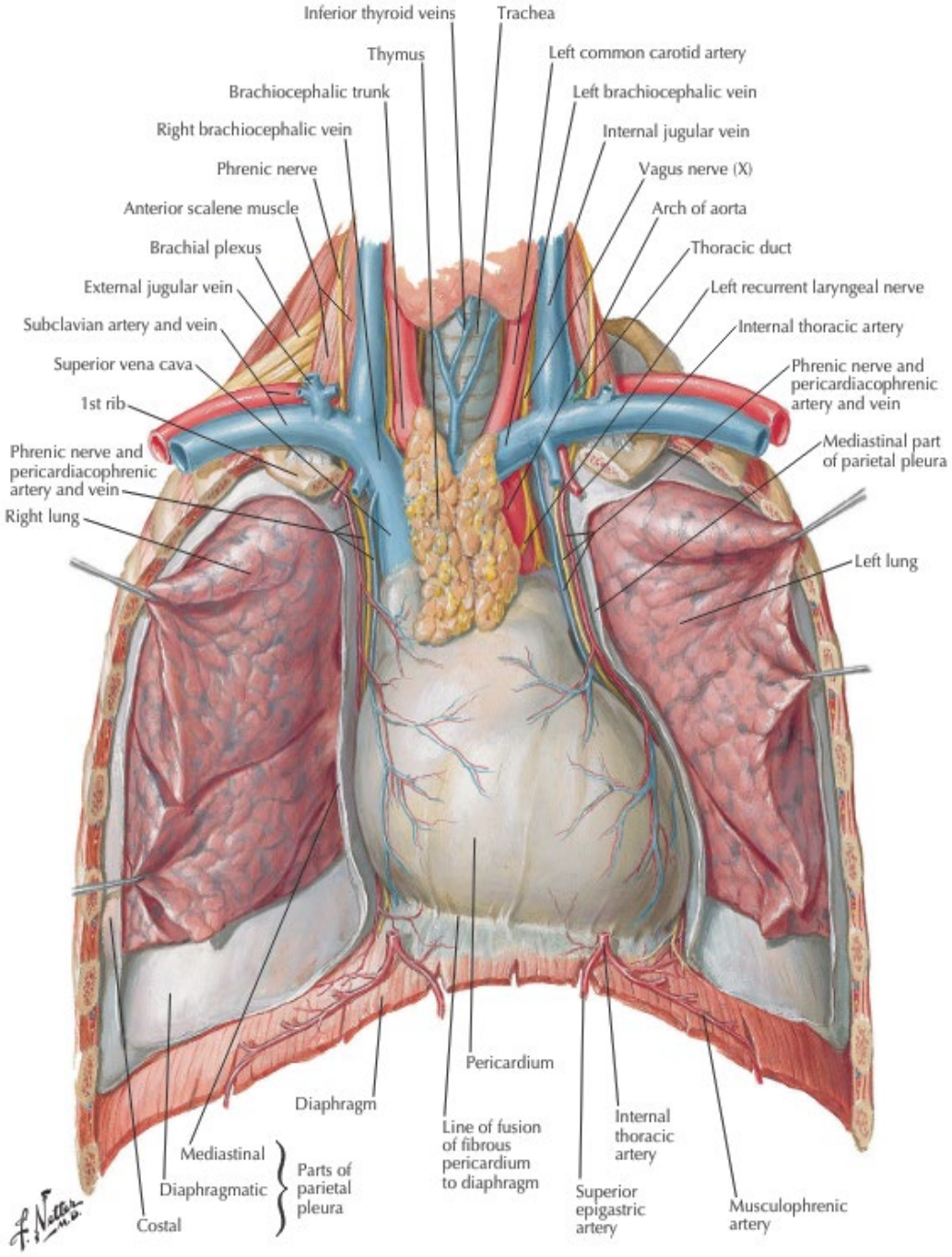

Figure 1: Heart external view, in its natural anatomical position (heart in situ). Source, Atlas of Human Anatomy from Frank H. Netter 6th edition, Plate 209 *(Netter, 2014)*.

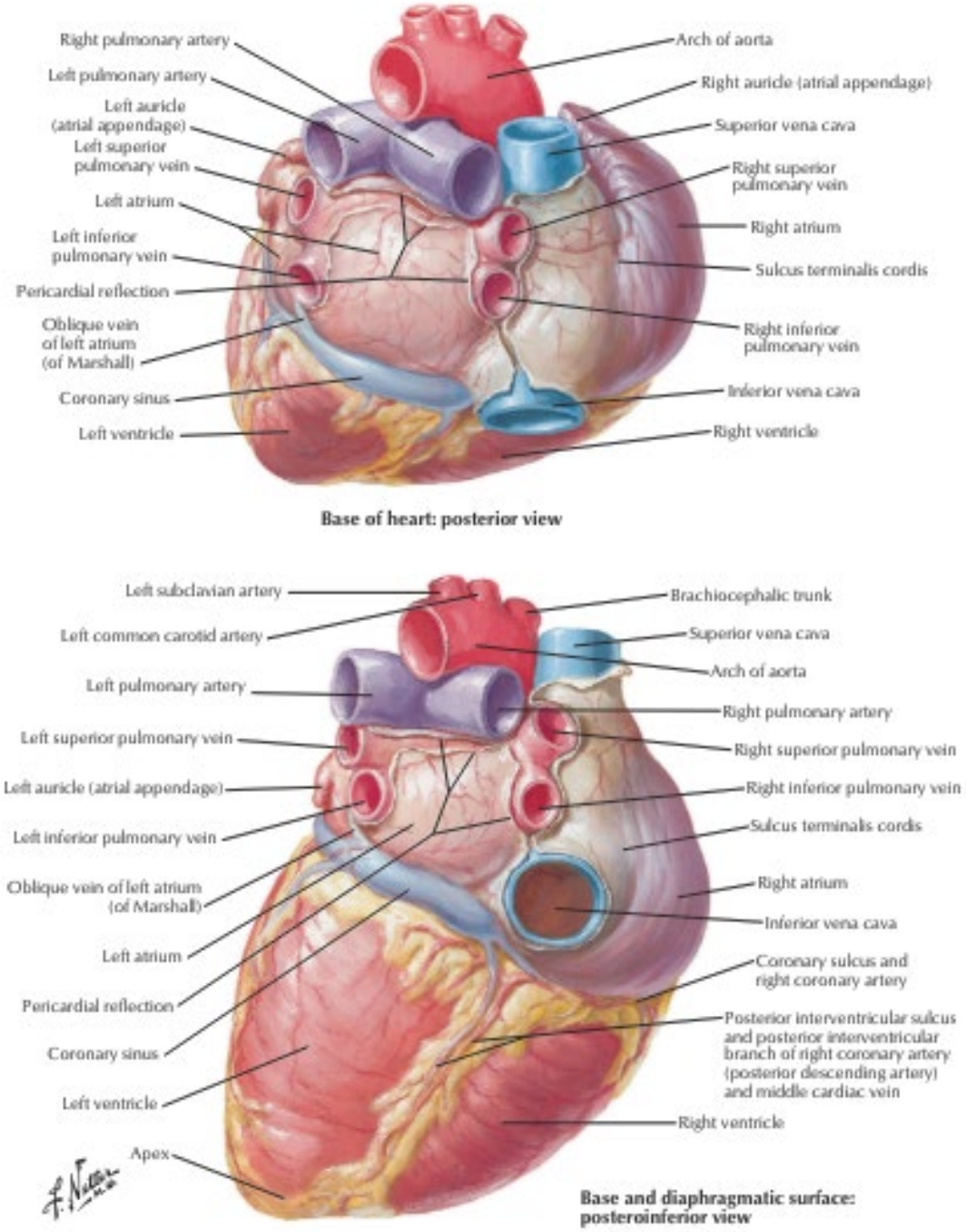

Figure 2: A posterior view of the base of the heart and a posteroinferior view of the base and diaphragmatic surface. Source, Atlas of Human Anatomy from Frank H. Netter 6th edition, Plate 211 *(Netter, 2014)*.

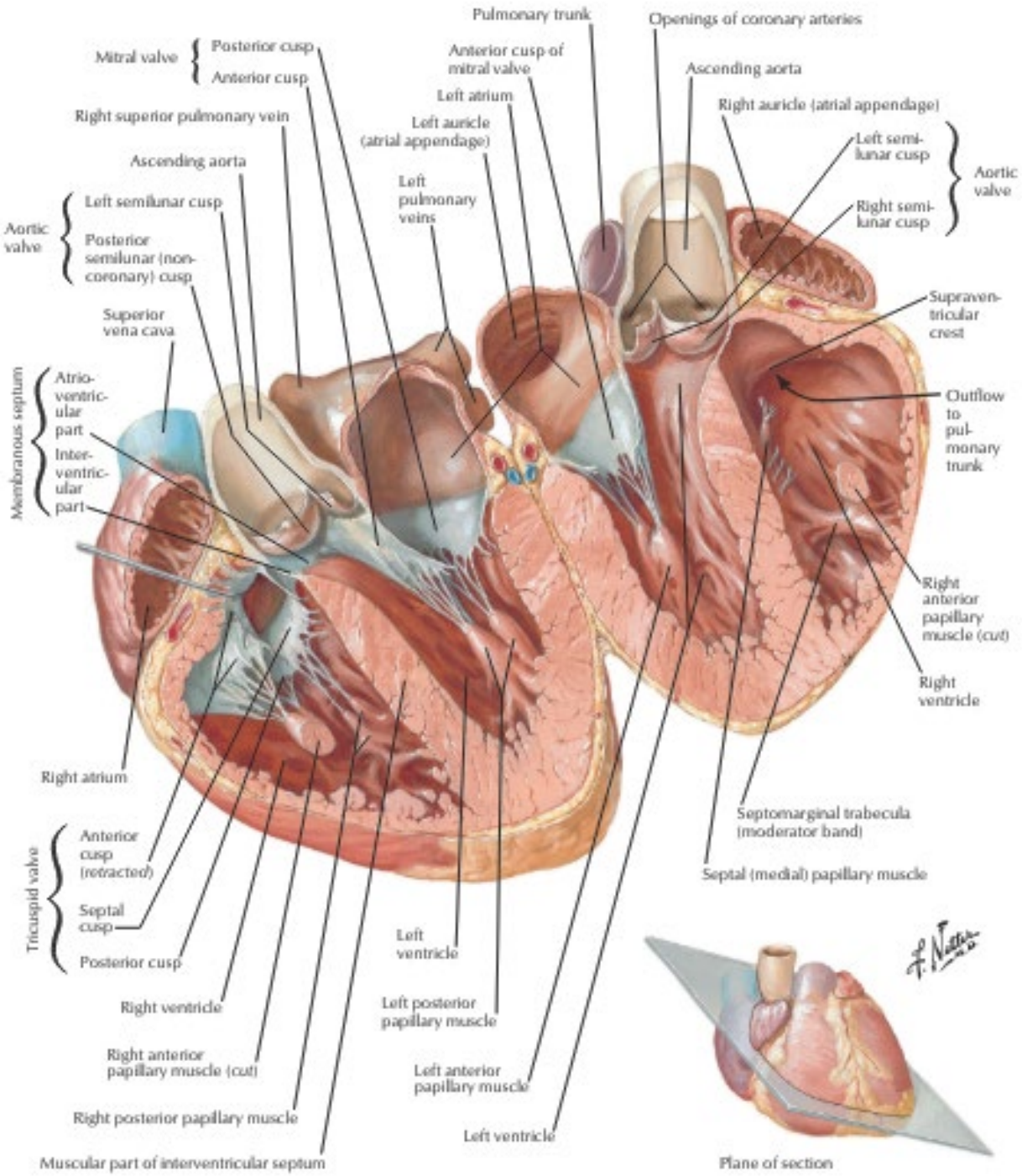

Figure 3: A plane section of the heart, enabling visualization of the heart chambers, including the atria and ventricles. Source, Atlas of Human Anatomy from Frank H. Netter 6th edition, Plate 221 *(Netter, 2014)*.

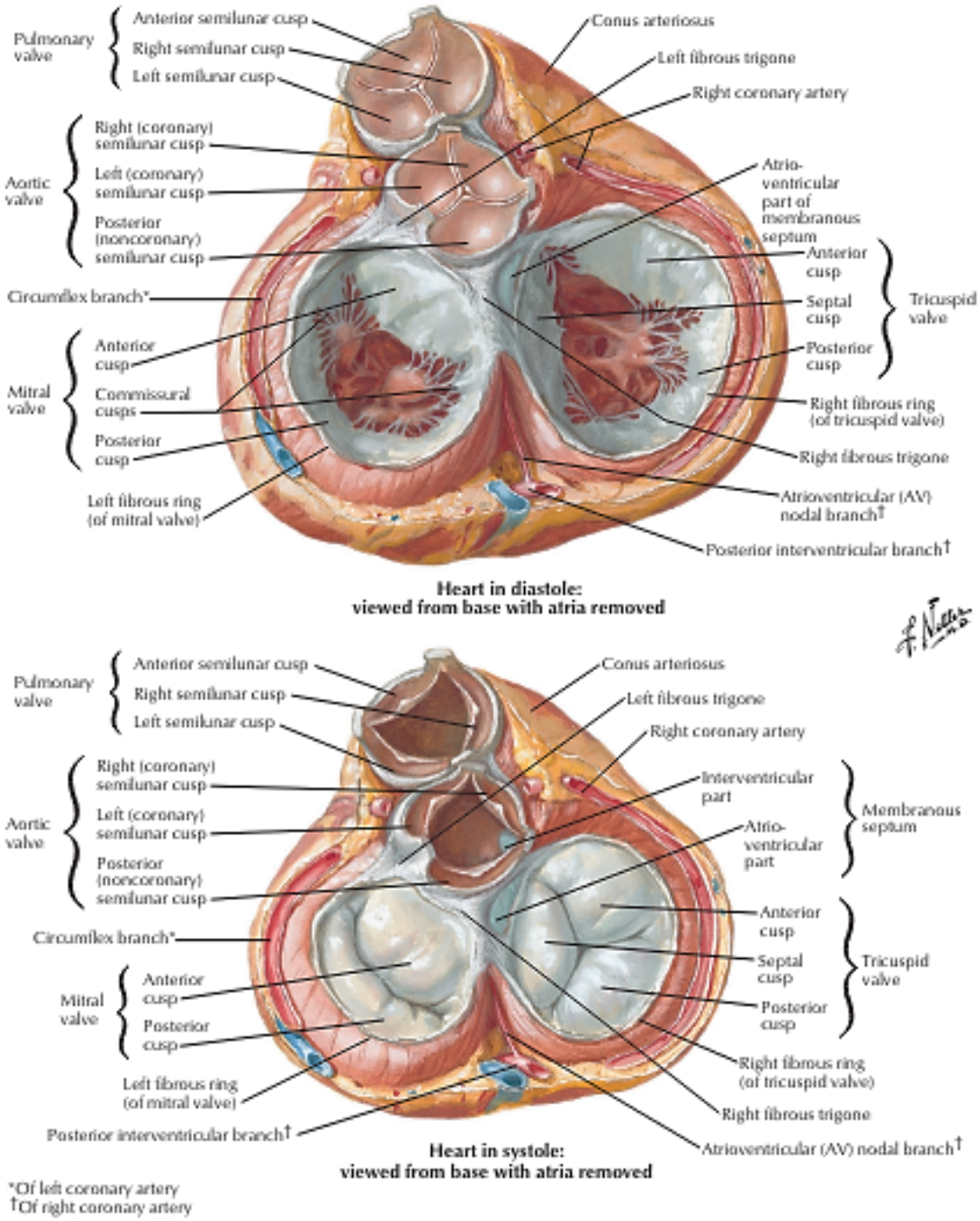

Figure 4: The heart valves, during diastole and systole, viewed from base with atria removes. Source, Atlas of Human Anatomy from Frank H. Netter 6th edition, Plate 2019 *(Netter, 2014)*.

1.2 Blood Circulation

The circulation of blood in the body comprises two interconnected pathways: systemic circulation and pulmonary circulation.

Systemic circulation begins as oxygen-rich blood is pumped from the left ventricle through the aorta, body's largest artery. As the blood flows through the aorta, it passes into the ascending or descending aorta, rapidly forming an extensive network of vessels that reach every corner of the body. These arteries gradually decrease in size, becoming smaller in diameter passing from arteries to arterioles, which further divide into tiny capillaries. Once the blood reaches the capillary bed oxygen and nutrition are distributed to the organs and tissues. After exchanging carbon dioxide for oxygen, the blood returns back to the heart, through a series of vessels that gradually increase in size. Small vessels called venules collect the blood from the capillary bed and start merging into larger vessels called veins. These veins converge as they travel back to the heart, eventually emptying into the heart's right atrium through major veins like the superior and inferior vena cava (Saldin, 2018) & (Stanfield, 2012).

Concurrently, pulmonary circulation starts from the right ventricle, where deoxygenated blood is pumped into the pulmonary artery, leading to the lungs for oxygenation. After exchanging carbon dioxide for oxygen in the pulmonary capillaries, oxygenated blood returns to the left atrium through the four pulmonary veins (Saldin, 2018) & (Stanfield, 2012).

In addition to systemic and pulmonary circulation, the coronary circulation provides vital blood supply to the heart muscle. Coronary arteries deliver oxygenated blood to the heart, while coronary veins drain deoxygenated blood from the myocardium. This blood returns to the right atrium through the coronary sinus, running parallel to the coronary arteries (Saldin, 2018) & (Stanfield, 2012).

Overall, the circulation of blood in the body forms a continuous loop known as the vasculature, ensuring efficient distribution of oxygen and nutrients to tissues and organs, while facilitating the removal of metabolic waste products. The vasculature plays a crucial role in maintaining the body's overall function and homeostasis (Saldin, 2018) & (Stanfield, 2012).

1.2.1 Coronary Artery Anatomy

The coronary arteries originate from the base of the aorta, behind the aortic leaflets, in a region named the sinuses of Valsalva. They course along the surface of the heart, branching extensively

with the main branches being the left coronary artery (LCA) and the right coronary artery (RCA). These arteries are responsible for supplying oxygen- rich blood to the myocardium. The small arteries penetrate the epicardium reaching the myocardium, ensuring adequate perfusion (Stanfield, 2012) & (Romagnoli, 2022).

The coronary dominance is defined based on the distribution of the coronary arteries. In clinical practice, the determination of coronary dominance relies on identifying the coronary artery responsible for giving rise to the posterior interventricular branch, which supplies blood to specific regions of the left ventricle. The coronary dominance is divided in three types; right dominance, left dominance and codominance. Right dominance is established when the posterior branch originates from the RCA, a scenario encountered in 80-90% of individuals. Left dominance manifests when the posterior branch stems from the LCA, 10-15% of cases. Codominance is recognized when the posterior branch arises from the RCA, yet the posterior wall of the left ventricle receives blood supply from the LCA, a configuration observed in approximately 5% of cases (Stanfield, 2012) & (Loukas, 2013).

The left coronary artery (LCA) arises from the left sinus of Valsalva and follows anteriorly to the left, extending towards the sternocostal surface of the heart (Figure 5). It bifurcates after 1 to 2 cm in two main branches, the circumflex artery and the left anterior descending artery. The circumflex artery lies on the left atrioventricular groove, providing blood to the left atrium and posterior and lateral parts of the left ventricle. The left anterior descending artery, also known as anterior intraventricular branch, supplies blood to the anterolateral papillary muscle and descends along the anterior intraventricular sulcus to the apex of the heart. The circumflex artery further branches into; atrial branches and obtuse marginal branches 1, 2 and 3. While the left anterior descending artery gives rise to the diagonal branches and the septal branches (Stanfield, 2012) & (Loukas, 2013).

The coronary veins complement the arterial system of the veins. Coronary venous drainage primarily occurs through the coronary sinus, located in the atrioventricular groove on the posterior aspect of the heart. The coronary sinus comprises the great cardiac vein, middle cardiac vein, small cardiac vein, posterior vein of the left ventricle and oblique vein of left atrium. It serves as the primary conduit for venous drainage from the myocardium, emptying into the right atrium. Additionally, a minor portion of venous drainage occurs via the anterior cardiac veins which directly drains into the right atrium, and through the Thebesian veins, valveless veins within the

myocardium, which drain to all four chambers of the heart (Stanfield, 2012). Figure 6 shows the coronary arteries and cardiac veins.

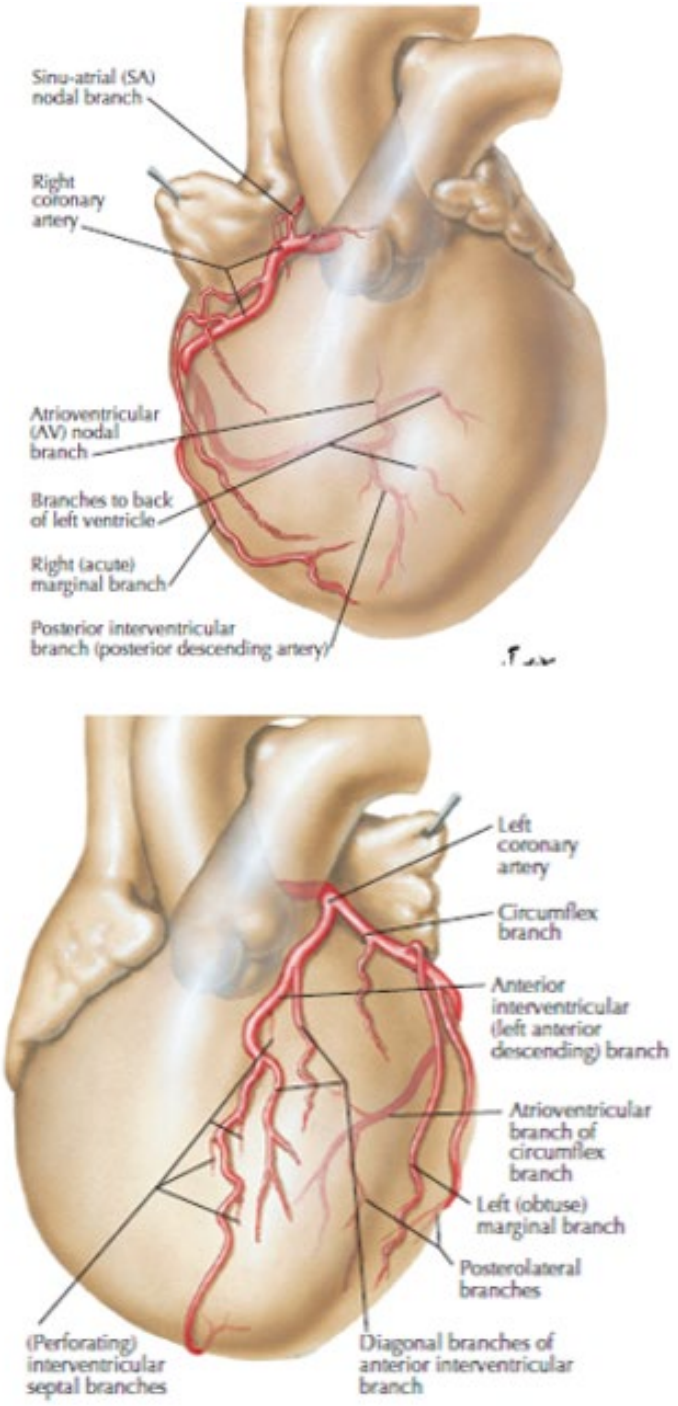

Figure 5: Panel on the top shows the RCA and its branches, while the panel on the bottom shows the LCA, with the corresponding branches. Source, Atlas of Human Anatomy from Frank H. Netter 6th edition, Plate 216 *(Netter, 2014)*.

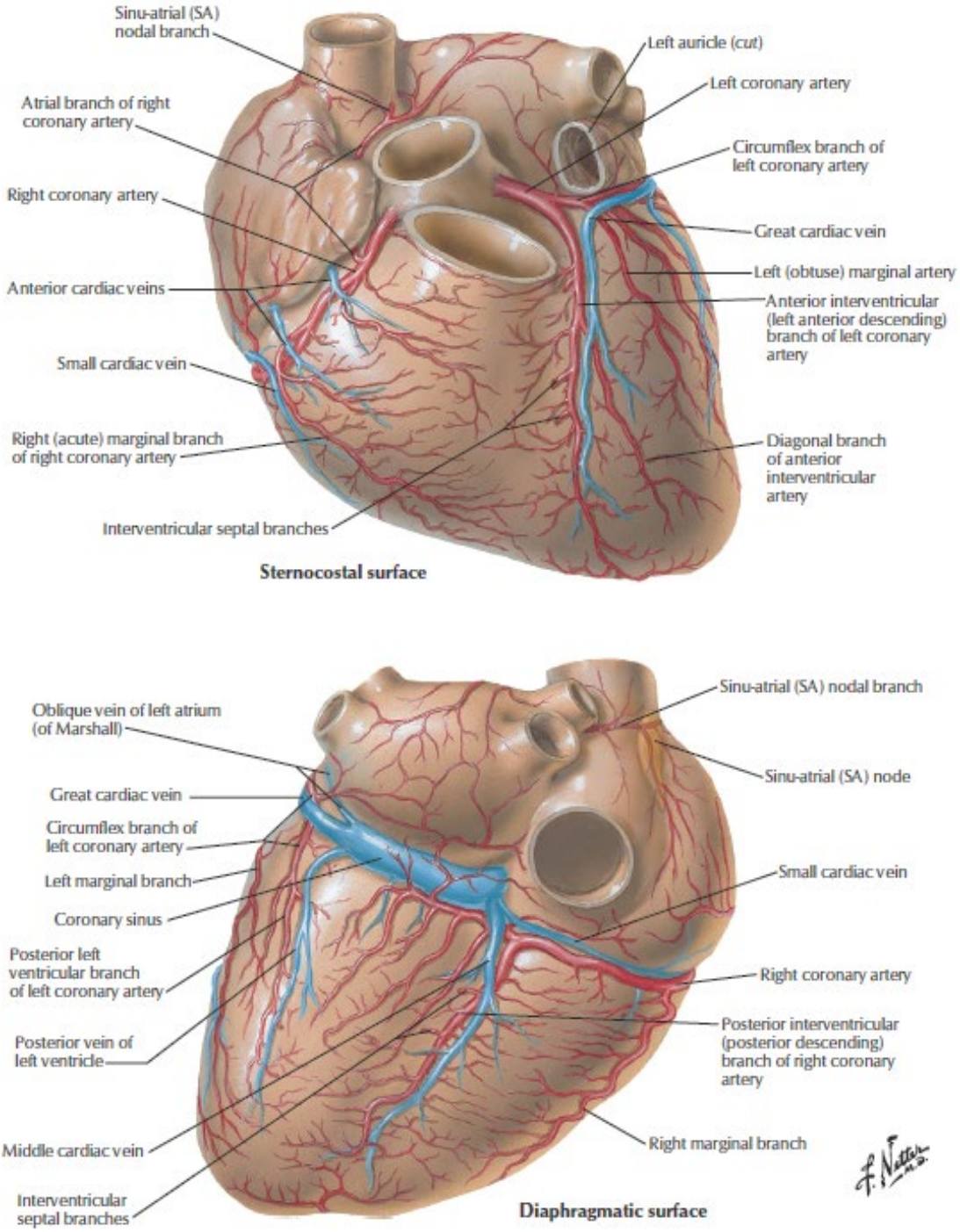

Figure 6: The coronary artery in red and cardiac veins in blue on the sternocostal surface of the heart (1st panel) and on the diaphragmatic surface of the heart (2nd panel). Source, Atlas of Human Anatomy from Frank H. Netter 6th edition, Plate 215 *(Netter, 2014)*.

1.2.1.1 Coronary Blood Flow

Coronary blood flow is a critical component of myocardial perfusion, comprising a small fraction, approximately 5%, of the total cardiac output directed through the coronary circulation. This flow exhibits distinctive biphasic characteristics: a minor peak during systole followed by a more pronounced and prolonged peak during diastole. A brief period of minimal flow between these phases facilitates clear delineation of the two peaks (Yartsev, 2013).

In 1976, Hoffman and Buckberg (Hoffman, 1976) illustrated this phenomenon by integrating left ventricular pressure (LV) and aortic pressure with coronary blood flow (Figure 7). This depiction stemmed from measurements conducted on the human ventricle at the time. Prior to this, in 1935, Gregg et al. (Gregg, 1937) provided detailed insights into phasic coronary blood flow in both the LCA and RCA (Figure 8). Their research aimed to ascertain whether coronary flow during normal conditions diminishes or halts during systole, or conversely, accelerates. These findings, derived from invasive experiments on canines, closely mirrored human cardiac physiology, offering distinctive characteristics for understanding coronary flow patterns.

Left ventricular coronary flow (Figure 9) demonstrates unique temporal patterns: a notable decrease during isometric contraction, potentially reaching negative values; a rapid surge in early systole, peaking synchronously with the peak aortic pressure; a substantial decline coinciding with reduced aortic pressure, occasionally dropping below baseline; a sharp rise during isovolumetric relaxation; maximal flow during mid-diastole; and a gradual decrease in late diastole in response to diastolic pressure gradients. The increased internal pressure during left ventricular systole elevates systolic coronary resistance, thereby diminishing coronary blood flow during this phase. Consequently, left ventricular perfusion primarily optimizes during diastole.

Similarly, right ventricular coronary flow exhibits analogous dynamics but typically experiences higher flow rates during ventricular systole due to lower systolic chamber pressures. This ensures equitable perfusion throughout both systolic and diastolic phases, reducing dependence on diastolic filling time and making it less susceptible to heart rate fluctuations.

It is widely acknowledged that approximately 75% of left ventricular blood flow occurs during diastole, while the right ventricle receives around 50%. These proportions reflect the division

of the cardiac cycle into systolic and diastolic phases, highlighting the dynamic nature of cardiac blood flow rather than a constant rate. Goodwill et al. (Goodwill, 2018) indicated a variability in flow rates, suggesting ranges of 50-100 mL/min/100g for the left ventricle and 30-60 ml/min/100g for the right ventricle.

Understanding the dynamic nature of coronary blood flow across cardiac phases is crucial for comprehending myocardial perfusion dynamics and their clinical implications in cardiovascular physiology and pathology.

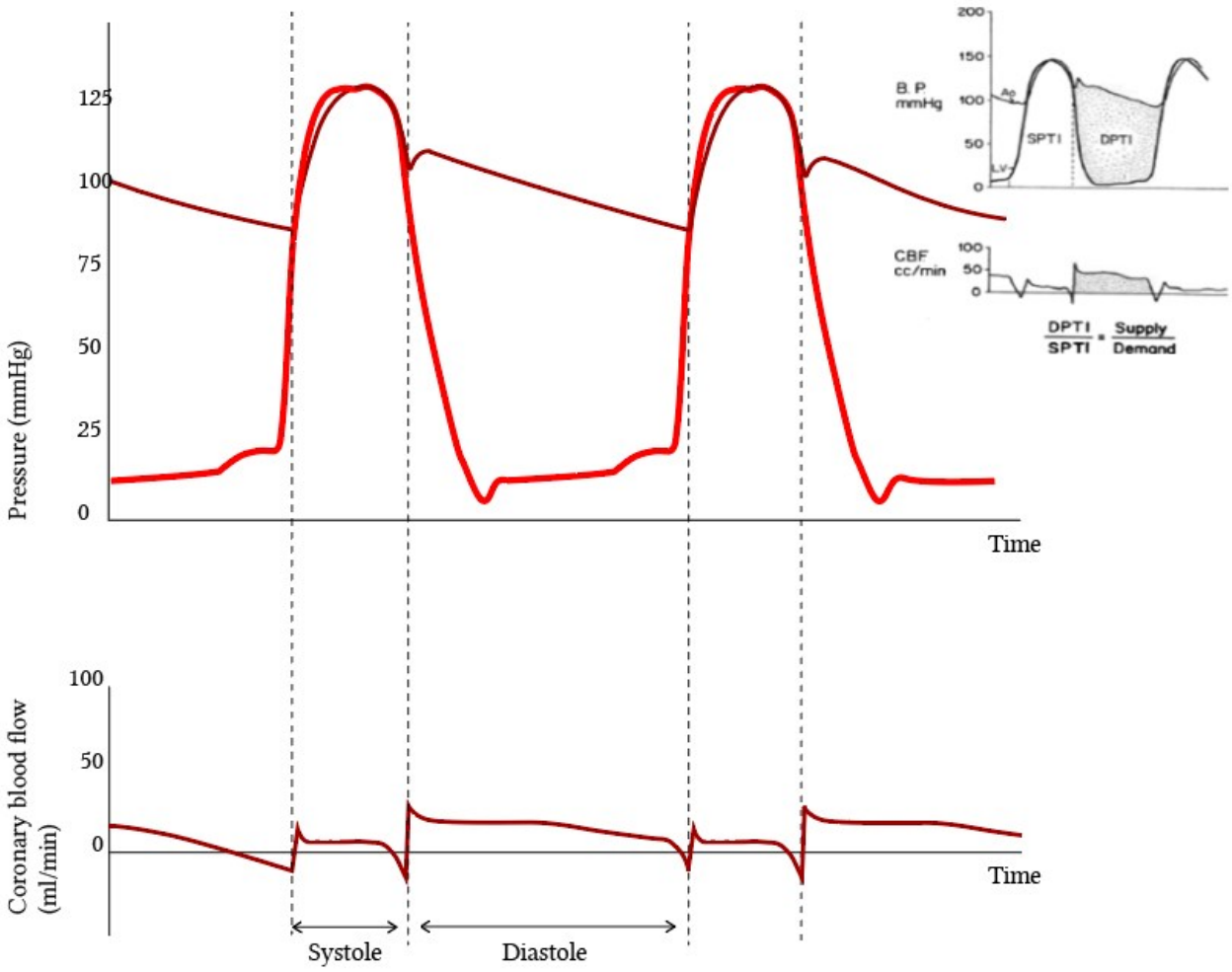

Figure 7: Hoffman and Buckberg diagram. First panel: In dark red the pressure in the aorta, in red the pressure in the left ventricle (LV). Second panel: coronary blood flow at the same time of the pressure in the above plot. The systolic and diastolic phases of a single cardiac cycle are delineated *(Netter, 2014)*.

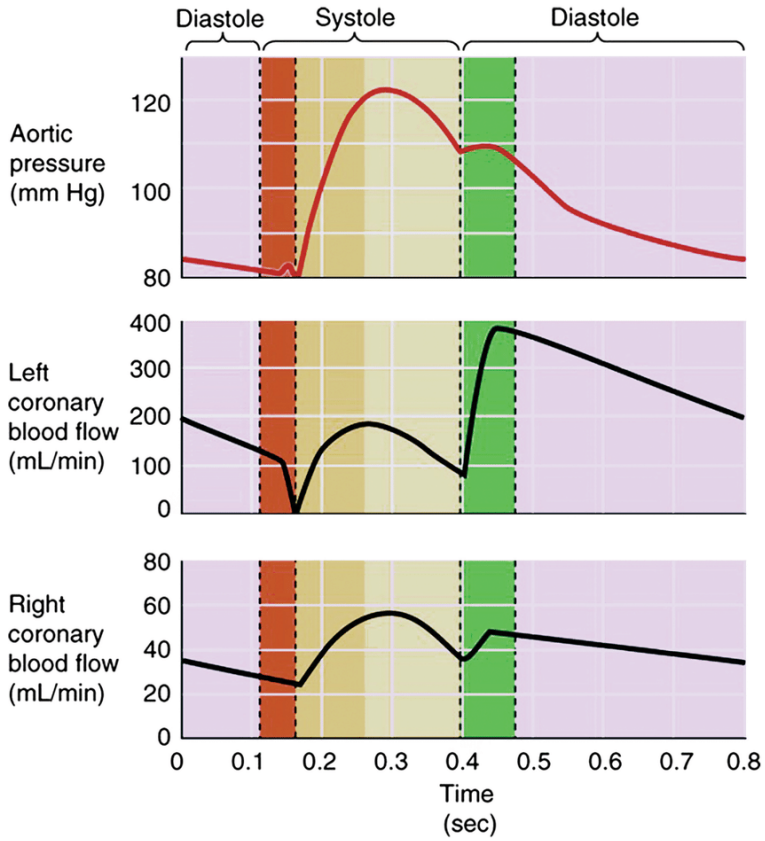

Figure 8: Flow-dynamics of the LCA and RCA. First panel: Aortic pressure during a cardiac cycle. Second panel: LCA flow during a cardiac cycle. Third panel: RCA flow during a cardiac cycle. Note the time is normalized *(Koeppen, 2010)*.

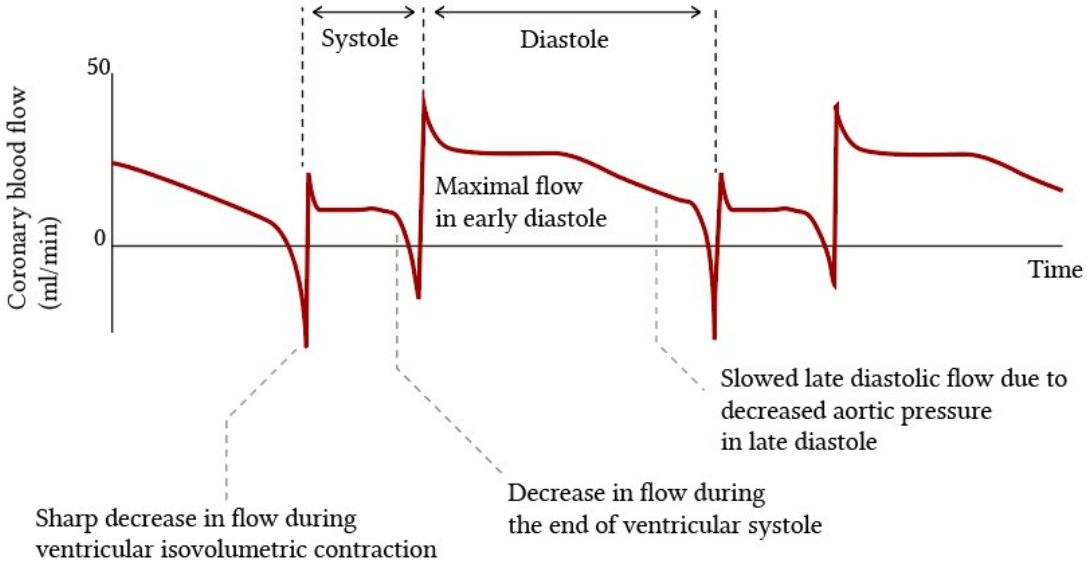

Figure 9: Coronary flow characteristics *(Yartsev, 2013)*.

1.2.1.2 Coronary Blood Flow Regulation and Diastolic Perfusion

At rest, the coronary flow typically ranges from 200 to 250 ml per minute, which accounts for approximately 5% of the total cardiac output. Concurrently, myocardial oxygen consumption is notably high, averaging around 8 ml of oxygen per minute per 100 grams of myocardial tissue. To meet this demand, the heart employs two adaptive mechanisms (Taegtmeyer, 2006):

- Dense network of capillaries: characterized by a high capillarity to cardiomyocyte ratio and short diffusion distances, ensures efficient oxygen delivery. Cardiac muscle exhibits a significantly higher capillary density, ranging from 3000 to 4000 per square millimeter compared to skeletal muscle.

- High Oxygen Extraction Ratio: the heart exhibits a remarkably high oxygen extraction ratio, typically ranging from 60% to 75%, compared to the whole-body oxygen extraction ratio of approximately 25%. Consequently, to augment oxygen delivery to the myocardium, coronary blood flow must increase.

The predominance of diastolic coronary perfusion refers to the fact that the majority of blood flow through the coronary arteries occurs during diastole, when the heart relaxes and arterial pressure decreases. This is particularly crucial for the epicardial arteries, which are exposed to compression forces during systole. Consequently, during systole, coronary arteries may be compressed by surrounding tissues, partially limiting blood flow, whereas during diastole, coronary arteries dilate, increasing blood flow to the cardiac (Goodwill, 2018).

The regulation of coronary blood flow is directly linked with oxygen demand, driven by the heart’s exceptionally high basal oxygen consumption. The blood flow in the coronaries is determined by several factors (Goodwill, 2018):

Coronary perfusion pressure (CPP): is a critical parameter in cardiovascular physiology, reflecting the pressure gradient that drives blood flow to the myocardium, particularly during diastole. During systole, the heart's contraction compresses intramuscular blood vessels, significantly reducing blood flow to the left ventricle due to the high pressure generated Blood flow to the left ventricular myocardium is diminished during this phase and resumes during diastole when the heart muscle relaxes and the vessels reopen. CPP can be calculated as the difference between the aortic diastolic pressure and the left ventricular end-diastolic pressure (LVEDP). A decrease

in aortic diastolic pressure or an increase in LVEDP reduces CPP, leading to diminished coronary blood flow. In contrast, the right ventricle and atria typically maintain lower pressures compared to the left ventricle, resulting in less reduction in coronary blood flow during systole due to less compression of their coronary vessels. Thus, ensuring adequate CPP is vital for maintaining sufficient myocardial perfusion, particularly under conditions of increased cardiac demand or compromised cardiac function.

- Perfusion time: increased heart rate reduces diastolic time more than systolic time, thereby decreasing coronary blood flow.

- Vessel wall diameter: the diameter of vessels influences coronary flow. Smaller arteries and arterioles serve as the primary sites of vascular resistance and, consequently, the main regulators of blood flow.

1.2.2 Coronary Artery Histology

The coronary arteries wall consists of three layers: the tunica intima (inner layer), tunica media (middle layer), and tunica adventitia (outer layer) (Saxton, 2023) & (Chen, 2016). The tunica intima is the innermost layer of the arteries, consisting of the endothelium, sub-endothelium, and the internal elastic lamina. This layer acts as a barrier facilitating smooth blood flow while also engaging in other cellular functions. Any breach in the endothelial lining exposes blood to the subendothelial layer, initiating the clotting process. Under the sub-endothelium lies a substantial internal elastic lamina. Tunica intima has a variable thickness, expressed as a ratio of media thickness which ratio in normal conditions varies from 0.1 to 1. Being really thin, this inner layer does not contribute to the mechanical properties of the vessel wall (Saxton, 2023).

The tunica media is situated in the middle layer of the arteries. It comprises layers of smooth muscle cells arranged in hexagonal pattern to optimize contractility. Typically, there are approximately five layers of smooth muscle, accompanied by minimal elastic fibers, collagen, and proteoglycans. A prominent external elastic lamina is usually only observable in larger arteries. This tunica has a fundamental role in physiology under normal hemodynamic load. Its thickness is on average 200 μm. Even though in case of pathology like atherosclerosis it is thinner with an average value of 80 μm (Saxton, 2023) & (Chen, 2016).

The tunica adventitia constitutes the outer connective tissue layer that supports the artery, protecting the vessel wall from over-stretching as well as avoid external mechanical forces to

ruin the vessel wall. It is composed of loose connective tissue containing fibroblasts, collagen, elastin fibers as well as vessels and nerves. Elastin fibers run parallel to collagen fibers but exhibit a secondary orientation, forming a mesh-like structure. As we move toward the outer adventitia, collagen bundles gradually increase in thickness and become more randomly distributed. In contrast, elastin fibers are largely sparse in this region (Saxton, 2023) & (Chen, 2016).

1.2.3 Mechanical Properties of Normal Coronary Arteries

The mechanical properties of coronary arteries refer to their physical characteristics and behavior in response to mechanical forces. Investigations into the mechanical properties of human coronary arteries, reveal a nuanced understanding of these vessels' behavior under physiological and pathological conditions. The intricate mechanical nature of coronary arteries is characterized by nonlinear, anisotropic, and viscoelastic properties. Comprising three distinct layers the tunica intima, tunica media, and tunica adventitia coronary arteries exhibit a sophisticated structural organization. The coronary arteries anisotropic behavior primarily is due to the orientation and arrangement within the walls. This anisotropic behavior is crucial for the proper functioning of coronary arteries. It allows the arteries to adapt to the dynamic mechanical forces exerted by blood flow and cardiac contractions in different directions. Such insights are paramount for developing targeted diagnostic and therapeutic interventions to mitigate cardiovascular risk and improve patient outcomes (Claes, 2010) & (Chen H. G., 2016).

Some of the key mechanical properties of coronary arteries include (Claes, 2010):

- Elasticity: coronary arteries possess elasticity, allowing them to expand and contract in response to changes in blood pressure and flow.

- Compliance: refers to the ability of arteries to expand and accommodate changes in blood volume without a significant increase in pressure. Coronary arteries exhibit a certain level of compliance, which is essential for buffering pulsatile blood flow and minimizing the workload on the heart.

- Stiffness: is the resistance of arteries to deformation under pressure. While some degree of stiffness is necessary for arterial function, excessive stiffness (arterial stiffness) can impair vascular function and increase the risk of cardiovascular diseases such as hypertension and atherosclerosis.

- Strength: coronary arteries need to withstand the mechanical stresses imposed by blood flow and cardiac contractions. They possess inherent strength to resist deformation and maintain structural integrity, preventing rupture or damage.

- Viscoelasticity: coronary arteries exhibit viscoelastic behavior, meaning their mechanical properties depend on both elastic and viscous components. This property allows arteries to absorb energy and dissipate mechanical stress, contributing to their ability to withstand repeated cycles of deformation.

Understanding the mechanical properties of coronary arteries is crucial for assessing cardiovascular health, diagnosing arterial diseases, and developing therapeutic interventions aimed at preserving arterial function and preventing adverse cardiovascular events (Claes, 2010).

1.2.4 Investigating Coronary Artery Disease (CAD)

Coronary artery disease (CAD), also known as ischemic heart disease, results from the building up of plaque within the arteries that supply blood to the heart. This plaque, primarily consisting of cholesterol deposits, leads to a condition called atherosclerosis, where the arterial walls narrow progressively. The narrowing reduces blood flow, which can partially or completely block arteries, causing various symptoms and complications (Libby, 2005) & (Centers for Disease Control and Prevention, 2024). The diagnosis of CAD often involves a series of tests such as electrocardiograms, echocardiograms, stress tests, chest X-rays, and invasive procedures like cardiac catheterization and coronary angiography. CAD represents a significant health challenge, requiring a multifaceted approach that includes prevention, early detection, and comprehensive management strategies to mitigate its impact and improve patient outcomes ((Libby, 2005) & (Zhonghua, 2014).

In recent years, the role of blood flow and shear stress has gained significant attention as a complementary explanation for plaque formation. Blood flow affects the vessel wall through shear stress, influencing endothelial cell behavior, including morphological and physiological changes. Low and oscillatory shear stress are major characteristics of the hemodynamic environment in regions opposite arterial flow dividers, which are prone to atherosclerosis. Methods for in vivo estimation of wall shear stress include acquiring three-dimensional (3D) reconstructions of vessel volume using either invasive modalities such as intravascular

ultrasound and invasive coronary angiography, or less-invasive techniques like coronary computed tomography angiography and cardiac magnetic resonance angiography. These techniques apply numerical methods, known as computational fluid dynamics (CFD), to calculate flow within the reconstructed arterial volume. The 3D reconstruction of the coronary artery tree, followed by numerical simulation using CFD based on individual patient data, is increasingly used to study hemodynamics and predict the behavior of blood flow inside coronary arteries. In the recent year the CFD applications has become of high interest in the prevention and diagnosis of CAD, focusing on the biomechanics of atherosclerotic plaques, detection of high-risk coronary plaques, and plaque progression, with the goal of identifying high-risk patients to reduce cardiac mortality (Zhonghua, 2014).

1.2.4.1 Sudden Cardiac Death

Sudden cardiac death (SCD) stands as a complex and life-threatening event, on various aspects of human health and society. Its ramifications extend far beyond the individual affected, reaching into medical, economic, and social spheres. Globally, an estimated 4 million cases of SCD occur annually, underscoring its significant burden on public health systems and communities worldwide. One of the most unsettling aspects of SCD is its often-unforeseen nature, with approximately 50% of cases manifesting as the first indication of an underlying cardiac condition. This aspect accentuates the formidable challenge of early detection and prevention, as individuals may not exhibit prior symptoms or indications of cardiovascular risk (Obrova, 2022).

Despite considerable advancements in healthcare, survival rates following out-of-hospital cardiac arrest remain dishearteningly low. This sobering reality highlights the urgent need for robust prevention strategies to mitigate the incidence and impact of SCD. Implantable cardioverter-defibrillators (ICDs) have emerged as a cornerstone in this effort, capable of delivering life-saving interventions in cases of arrhythmias. However, the efficacy of such devices hinges on the accurate identification of individuals at high risk of SCD, a task that continues to pose significant challenges to clinicians and researchers alike. A deeper understanding of the underlying mechanisms of SCD is imperative for the development of targeted prevention and intervention strategies (Obrova, 2022).

Central to the pathology of SCD are the coronary arteries, which play a pivotal role in supplying oxygenated blood to the heart muscle. Occlusion or obstruction of these vessels, typically due to atherosclerosis or thrombosis, can precipitate myocardial infarction, a leading cause of SCD.

The sudden interruption of blood flow to the heart muscle deprives it of essential nutrients and oxygen, triggering a cascade of events culminating in cardiac arrest and, ultimately, death (Obrova, 2022).

Moreover, structural abnormalities of the coronary arteries, such as CAD or congenital anomalies, can predispose individuals to arrhythmias and sudden cardiac events. These conditions may disrupt the normal electrical conduction of the heart, leading to irregular heartbeats that can culminate in SCD if left unchecked (Obrova, 2022).

Given the intricate interplay between coronary health and cardiac function, preventing SCD requires a holistic strategy that tackles both the structural hemodynamic and electrical aspects of cardiovascular well-being.

II Section: Modeling of Blood Flow in Coronary Artery

In this section, the focus will be on existing modeling techniques and their application in the cardiovascular system. This includes details on a literature review, on models of the coronary artery that have already been implemented, along with details on the conditions required to make these models feasible.

2.1 Models

Model is a representation of a system or process, providing a theoretical description that may help in the understanding how the system or process works, or how it might work. In other words, a model is an approximation of the reality. The extent to which the model represents the real behavior of the system dependents on the level of detail included. Models find application in everyday life and in different scientific contexts (Vynnycky, 2010). Thus, in research it has been shown that the goal is to use simple models that effectively represent the system of interest (Prinz, 2023).

The use of biomedical models dates back centuries. In the early 20th century, simple mathematical models were used to understand basic biological processes. By the mid-20th century, the first compartmental models in pharmacokinetics were developed. The advent of computer technology at the end of the 20th century allowed for a more complex simulations and at the same time new imaging technologies provided higher accuracy and deeper inside into physiological modeling. In 21st century, modeling approach in biomedical field have aimed to integrate knowledge from models to achieve personalized medicine. Modern models focus on detection, prevention and personalization of the system (BMJ, 2005).

Models based on the modeling approach used to obtain them can be categorized in following categories;

- Animal Models: used for preclinical testing, mainly on new drugs, and also to understand diseases mechanisms. The choice of animal depends on the research being conducted, in general are preferred to be used mice, rats, rabbits, dogs (Mukherjee, 2022).

- In Vitro Models: also known as laboratory models, these are created in controlled environments. The first in vitro models were the cell cultures, but the term has now generalized to include also other research fields (Wang, 2015).
- Imaging – Based Models: these models utilize advancements in imaging techniques to obtain a detailed anatomical and physiological representations (Zhang, 2017).
- Mathematical Models: used to describe or predict processes through equations and computations (Segel, 1989).
- Computational Models: involve complex algorithms and simulations to predict the behavior of systems under various conditions (West, 2017).
- Electrical Models: are used to simulate and study the electrical properties of a system, such as cardiac rhythms (FitzHugh, 1961).

In cardiology, modeling has become into an indispensable tool, providing invaluable insights into cardiac function, disease progression, and treatment optimization. These models have transcended their traditional role only in research environments and have seamlessly integrated into clinical practice, enriching diagnostic and therapeutic approaches. Through sophisticated computational algorithms, models simulate intricate cardiac dynamics, allowing to understand of physiological processes and predictive analyses of disease trajectories. Moreover, they serve as platforms for personalized medicine, enabling tailored treatment strategies that account for individual patient characteristics and pathologies (Niederer, 2019).

2.1.1 Computational Fluid Dynamics (CFD) Modeling

Computational fluid dynamics (CFD) modeling is a modeling approach based on the principles of fluid mechanics, utilizing numerical methods and algorithms to solve fluid flow problems. CFD is considered as a really important tool for more realistic representation of the reality. The three fundamental principles that govern fluid motion are (Wikipedia, 2024):

1. Conservation of Mass: Continuity Equation (White, 2005)

$$\frac{D\rho}{Dt} + \rho(\nabla \cdot \vec{v}) = 0 \tag{2.1}$$

where ρ is the density, $\vec{v}$ is the velocity and ∇ the gradient operator. If the density is constant the flow is incompressible and the continuity equation becomes the following

$$\nabla \cdot \vec{v} = 0 \tag{2.2}$$

2. Momentum Conservation: Navier – Stokes Equation (White, 2005)

$$\frac{\partial}{\partial t}(\rho\vec{v}) + \nabla \cdot (\rho\vec{v}\vec{v}) = -\nabla p + \nabla \cdot (\bar{\bar{\tau}}) + \rho\vec{g} \quad (2.3)$$

where p is the static pressure, $\bar{\bar{\tau}}$ is the viscus stress tensor and $\rho\vec{g}$ is the gravitational force per unit volume. and the principle of energy conservation. Eq. 2.3 for ensiling the study can be divided in 5 terms (White, 2005);

I.	Local changes in time	$\frac{\partial}{\partial t}(\rho\vec{v})$
II.	Momentum convection	$\nabla \cdot (\rho\vec{v}\vec{v})$
III.	Surface force	$-\nabla p$
IV.	Diffusion term	$\nabla \cdot (\bar{\bar{\tau}})$
V.	Mass force	$\rho\vec{g}$

3. Conservation of Energy: First Law of Thermodynamic Energy Equation, it states that the sum of work and heat added to the system will result in the increase of the energy in the system (White, 2005).

Within CFD, the Finite Volume Method (FVM) emerges as a widely-used numerical technique for solving the governing equations of fluid flow. The FVM decomposes the simulation domain into a discrete grid of control volumes and uses numerical integration of conservation equations within these volumes to approximate the solution of the problem. In other words, the FVM subdivides the domain where the flow occurs into discrete volumes called cells and solves the flow equations within each volume. This approach enables obtaining approximate solutions to the differential equations describing the flow, allowing for accurate evaluation of variables of interest such as velocity, pressure, and temperature within the domain of interest. Still there are two main error sources in FVM (Versteeg, 2007):

- Discretization error, generated by the interpolation of the variables on the cell surfaces.
- Linearization error, generated by the linearization method chosen to solve the nonlinear system.

The refinement of the mesh reduces the discretization error but this will not help in reducing the linearization error (Versteeg, 2007).

The most common CFD tools are based on the Navier-Stokes Eq. 2.2, which general form is explained briefly above, other terms are added or removed based on the physics that wants to be described. In the succeeding of the CFD is really important to proper place the operating conditions, numerical methods and also the physical considerations (Versteeg, 2007).

The CFD model code is mainly divided in three sections and each has its sub-sections (Versteeg, 2007) & (Ansys, n.d.):

1. Pre – processing
    A. Definition of the geometrical region of interest
    B. Meshing, sub-division of the geometry in cells
    C. Selection of the physical phenomena needed to be modelled
    D. Definition of fluid properties (constitutive equations)
    E. Specification of appropriate boundary conditions
2. Solver
    A. Integration of the governing equations over all the cells of the domain
    B. Conversion of the resulting integral equation into algebraic equations
    C. Solving the algebraic equations with an iterative method
3. Post – processing
    A. Visualization of the obtained data
    B. Dynamic display of the results
    C. Alphanumerical output for further changes.

One significant disadvantage of the field of CFD is its high computational expense, making its progress heavily dependent on advances in computing power such as cloud computing.

2.1.1.1 CFD in Cardiovascular System

Computational models are revolutionizing cardiology by integrating patient-specific diagnostic data with physiological and physical principles crucial for cardiac function. These models offer a unified framework to merge diverse patient data, enabling a deeper understanding of individual pathophysiology and tailored treatment strategies. By simulating cardiac dynamics, these models provide insights that may otherwise remain hidden or too difficult to be obtained. Unlike traditional empirical methods, computational models leverage cause-consequence relationships to personalize care, adjusting parameters to align model predictions with clinical measurements. As cardiology specific CFD models emerge as vital tools for optimizing the diagnosis but also the treatment of cardiac pathologies (Niederer S. A., 2019).

The core of CFD in cardiology are advanced mathematical algorithms and high-performance computing to simulate the behavior of blood as it travels through the intricate network of arteries, veins, and capillaries. By integrating patient-specific imaging data, such as magnetic

resonance imaging (MRI) or computed tomography (CT) scans, CFD models can accurately replicate the anatomical features and physiological conditions unique to each individual. These patient-specific simulations provide clinicians with invaluable insights into the hemodynamic characteristics of blood flow, including velocity profiles, pressure gradients, and shear stresses, which are critical for understanding the pathophysiology of various cardiovascular diseases (Morris, 2016).

Moreover, CFD plays a pivotal role in the optimization of interventional procedures. By simulating blood flow within coronary arteries or cardiac chambers, CFD enables clinicians to evaluate the hemodynamic performance of stents, valves, and other devices in silico, prior to their deployment in the clinical setting. These virtual simulations allow for the refinement of device designs, the identification of potential complications, and the customization of treatment strategies to suit the individual anatomical and physiological characteristics of each patient (Morris, 2016).

In essence, CFD represents a paradigm shift in cardiovascular medicine, empowering researchers and clinicians alike with powerful computational tools to unravel the mysteries of blood flow dynamics and revolutionize the diagnosis, treatment, and management of cardiovascular disease (Morris, 2016).

2.1.2 Electrical Modeling of the Cardiovascular System

Electrical modeling of the cardiovascular system involves representing the cardiovascular circulation using electrical circuit analogies. The lamped models have been used for over a century to simulate the operation of the cardiovascular system, and for simplicity such models can be represented by electrical circuits. Doing so it helps in understanding the hemodynamic properties and the functional behavior of the cardiovascular system. In an electrical representation the compartments in general include resistors, capacitors and inductors (Ghasemalizadeh, 2014) & (Westerhof, 2010).

Main components and their electrical analogues (Abdolrazaghi, 2010)

- **Pressure (P) → Voltage (V):** In the cardiovascular system, blood pressure is analogous to voltage in an electrical circuit. P represents the force exerted by the blood against the walls of the blood vessels.

- **Blood Flow (Q)→ Current (I):** Blood flow is analogous to electrical current. Q represents the movement of blood through the vessels.
- **Vascular resistance →Resistance (R)**: R impedes the flow. In the cardiovascular system, this is the vascular resistance offered by the blood vessels to the flow of blood.
- **Compliance → Capacitance (C)**: Capacitance in electrical systems stores charge, whereas compliance in the cardiovascular system represents the ability of blood vessels to expand and store blood.
- **Inertia of Blood → Inductance (L)**: Inductance in electrical circuits opposes changes in current, while the inertia of blood resists changes in blood flow.

By focusing on distinct segments of the cardiac circulation, employing physiological metrics such as pressure and flow, and finding ways to include also additional analogues, one can comprehensively elucidate the hemodynamics of circulation utilizing the above-mentioned electrical components. This approach not only allows for a nuanced understanding of cardiovascular dynamics but also facilitates the integration of multifaceted physiological measures into the conceptual framework of electrical modeling. This methodological versatility not only enhances our ability to capture the intricacies of cardiovascular dynamics but also underscores the robustness and adaptability of electrical modeling in depicting complex physiological phenomena.

2.1.2.1 Windkessel Model

Windkessel model derives its name from the Windkessel effect, a common term used in medical field to describe the arterial blood pressure waveform pattern in terms of interaction with the stroke volume and the compliance characterizing the aorta and large elastic arteries, as well as the resistance of smaller vessels like arteries or even arterioles. The term Windkessel is German for “air chamber”, but it generally directly implies elastic reservoir. The first simulation of the Windkessel effect in blood flow was performed by Hales in 1733 with a formal formulation of it provided later by Otto Frank in 1899 (Ghitti, 2020). Windkessel models are also referred to as lamped parameter models, which are simplified representation of complex physical systems divided into discrete components with assumed uniform properties. These models have found applications in analyzing hemodynamics systems by treating them as networks of interconnected components with distinct, averaged properties (Doeblin, 1998).

The Windkessel model serves as a fundamental framework for simulating an arterial vessel by considering its resistance and compliant characteristics. Throughout a cardiac cycle, encompassing systolic and diastolic phases, the left ventricle experiences high pressure during systole, facilitating the opening of the aortic valve and the flow of blood through the aorta. Conversely, in the diastolic phase, the aortic valve closes. In a hypothetical scenario where the aorta is a rigid pipe, blood flow would be restricted to 100% in the systolic phase and 0% in the diastolic phase. However, the aorta possesses an elastic nature, leading to expansion of its walls in the systolic phase due to pressure and contraction in the diastolic phase. Consequently, blood flows through the aorta in both systolic and diastolic phases, resulting in the smoothing out of the pulsatile nature of the heart. The Windkessel model tries to mimic this by modelling an arterial vessel with a resistance and a compliance. The resistance represents the distal vessels in the bloodstreams, such as the arterioles and capillaries, while the compliance represents the elasticity of the larger blood vessels.

The Windkessel model is based on the principle of mass conservation, where the outflow to the periphery (Qp) and the stored volume in the aorta (Qa) is the same as the inflow (Q). Applying the mass conservation, the following differential equation is obtained:

$$Q = Qa + Qp = \frac{\partial \mathrm{V}}{\partial \mathrm{p}} \frac{\partial \mathrm{p}}{\partial \mathrm{t}} + p/R \tag{2.4}.$$

In this equation, the stored volume (Qa) is described as the volume change over time, equivalent to the volume change over the pressure times the pressure changes over time. The change of volume over pressure is the arterial compliance. The peripheral outflow (Qp) is described as the pressure (p) divided by the peripheral resistance (R):

$$Q = C \frac{\partial \mathrm{p}}{\partial \mathrm{t}} + p/R \tag{2.5}.$$

Eq. (2.5) can be compared with the electronical analogue in which Q is the current (I), pressure p the potential, compliance C is the electrical capacitor (c) where electric charge is stored, and the peripheral resistance R is the resistor (Jørgensen).

The simplest Windkessel model is the 0-dimentional (0D) model, which represent the compliance of the blood vessel wall, the blood flow resistance, and the inertia through the cardiovascular system. A graphic representation of this viscoelastic model is shown in Figure 10. The literature also describes other Windkessel models with higher number of components, namely 2-element, 3-element and 4-element Windkessel model (Figure 11). These models are

widely applied and show good results in reproducing the pressure waves of the arterial tree (Westerhof N. E., 1971).

In general scenario of the Windkessel model, the following electrical correspondence could be written:

$$P = QR \quad \Leftrightarrow \quad V = IR \tag{2.6}$$

$$Q = C\frac{dP}{dt} \quad \Leftrightarrow \quad I = c\frac{dV}{dt} \tag{2.7}.$$

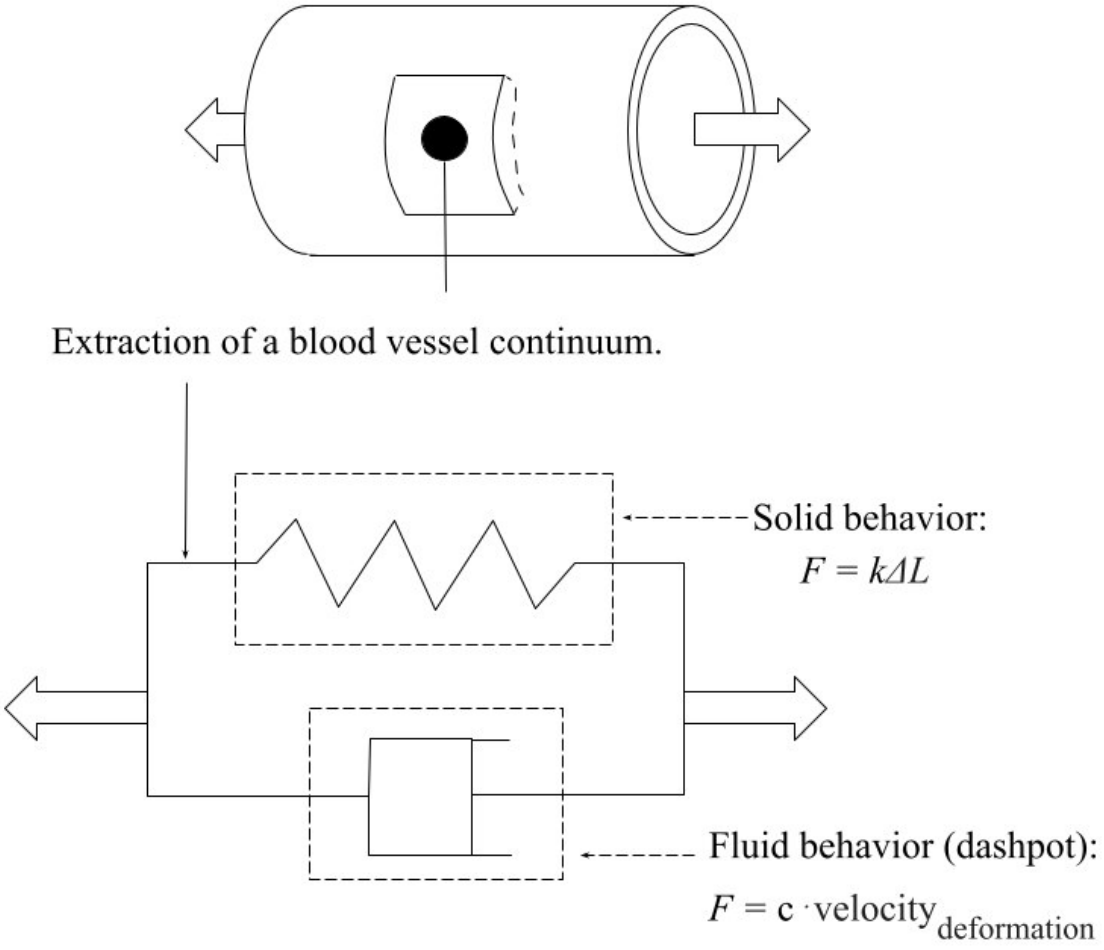

Figure 10: Kelvin – Voigt viscoelastic model for vessel wall, characterized by a parallel circuit of the spring and the dashpot. The spring represents the solid wall while the dashpot the fluid behavior. k is the stiffness coefficient characterizing the spring and c is the damping coefficient of the dashpot (*Pirola*, 2019).

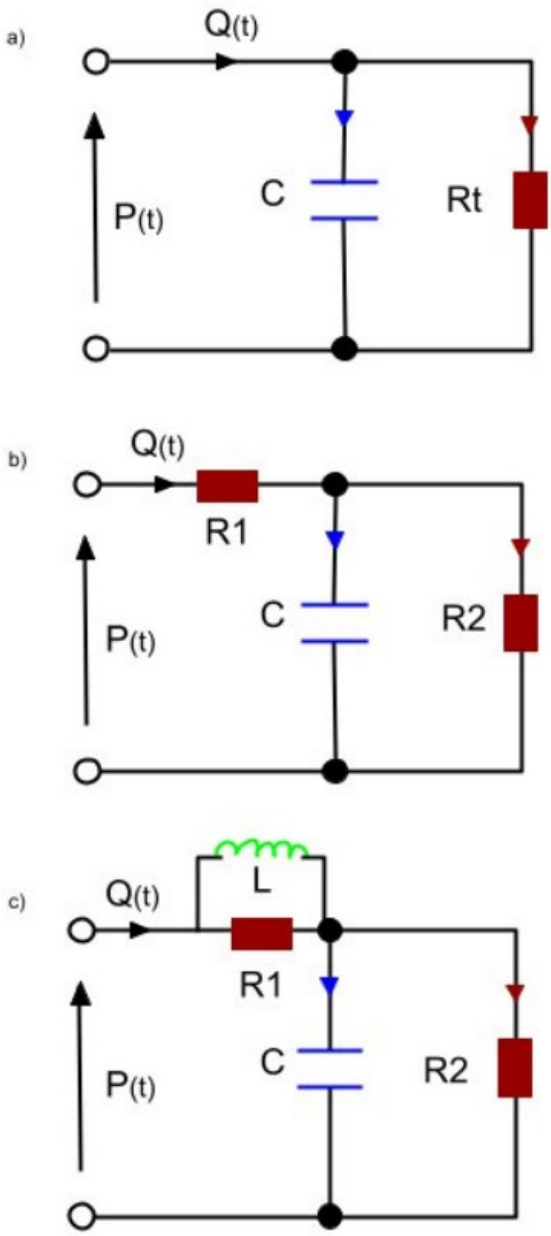

Figure 11: Electrical circuit analogs of 2-element, 3-element, and 4-element Windkessel models, respectively represented in panels a, b and c. Q(t) is the blood flow, P(t) is the pressure, C is a capacitor, Rt, R1, and R2 are resistors, and L is an inductor *(Pirola, 2019)*.

For the 3-element Windkessel model, with two resistors and a capacitor in electrical analogue, the following equations can be derived:

$$Q = \frac{P_1}{R_1} = \frac{P_2}{R_2} + C\frac{dP_2}{dt} \tag{2.8}$$

$$P = P_1 + P_2 + P_{out} \tag{2.9}.$$

where P_1 is the P in correspondence of R_1 and P_2 *i*s the P in correspondence of R_2 *and* P_{out} is the P with no microcirculation.

Substituting Eq. 2.9 in Eq. 2.10 is obtained:

$$\frac{P_1}{R_1} = \frac{P - P_1 - P_{out}}{R_2} + C\left(\frac{dP_2}{dt} - \frac{dP_1}{dt} - \frac{dP_{out}}{dt}\right) \tag{2.10}$$

$$Q\left(1 + \frac{R_1}{R_2}\right) + CR_1\frac{dQ}{dt} = \frac{P - P_{out}}{R_2} + C\frac{dP}{dt} \tag{2.11}.$$

In Eq. 2.11 is expressed the existing relationship between Q, P using the pressure with no microcirculation (P_{out}), which in general is assumed to be 0, the two resistance (R_1, R_2) and the compliance (C) (Pirola, 2019). The electrical circuit corresponding to the above equations is depicted in Figure 12.

When applied the 3-element Windkessel model to a cardiovascular system, the total resistance is split into R_1, R_2. The proximal resistance (R_1) corresponds to the resistance close to the heart, while the distal resistance (R_2) corresponds to the resistance in the small capillaries.

The interest of using the Windkessel models lies in their applicability as boundary conditions, where the pressure at the boundary is contingent on the outlet flow rate. Utilizing information from the preceding timestep, new pressure and flow values are generated. To initialize the Windkessel model, an initial pressure and flow are required. The initial pressure is set to the diastolic blood pressure, taking the lowest present value at all outlets. The flow is assumed to be zero, for the time being that in the inlet boundary there is no flow present.

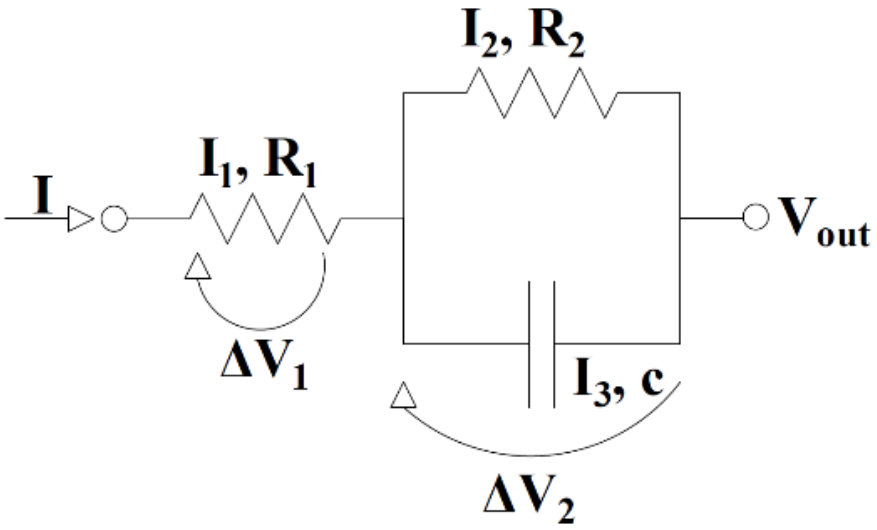

Figure 12: An electrical analogue of the 3 element Windkessel model.

2.2 Review of Coronary Artery Models in Literature

Coronary artery modeling is pivotal in the understanding of cardiovascular physiology and pathophysiology, disease diagnosing and planning treatment. Various models have developed in the years, each with unique approaches and application. This sub-section reviews and compares the different coronary artery models proposed in literature.

Computational Fluid Dynamics (CFD) Models

The critical role of CFD models in analyzing blood flow dynamics within the coronary arteries, is described by Alzhanov et al. (Alzhanov, 2023), which is essential for understanding cardiovascular disease such as atherosclerosis. The models mentioned in the study integrate precise arterial geometries and plaque characteristics, making it possible the simulation of local hemodynamics, including also the wall shear stress (Alzhanov, 2023). Utilizing advanced numerical techniques to solve the Navier-Stokes equations, these models incorporate computational grids derived from medical imaging data, ensuring fidelity in representing three-dimensional arterial structures. By simulating blood flow under various physiological conditions and pathological scenarios, such as the presence of stenosis or different plaque compositions, these CFD models provide insights into disease progression and the efficacy of therapeutic interventions. The study emphasizes the utility of CFD simulations in clinical decision-making and treatment planning for coronary artery disease, underscoring their role in advancing bioengineering applications in cardiovascular medicine (Alzhanov, 2023).

Patient-Specific Modeling

In 2010 Kim et al. published the development of a comprehensive method that integrated 3D models of the heart and arterial system to predict coronary flow and pressure (Kim, 2010). In this patient – specific model was included the interaction between the heart's contractile forces and the interaction coronary vessels, which plays an important role in a realistic simulation. The characteristic of this model was the use of a lumped parameter heart model coupled with a close-loop system to account for the intramyocardial pressure, giving in this way insights into individual patient conditions (Kim, 2010). In Figure 13 is shown the model with the electrical boundary condition analogy. Specifically, the coronary outlet model employed detailed computational fluid dynamics (CFD) techniques to simulate blood flow through specific

coronary arteries, considering factors such as vessel geometry, wall compliance, and hemodynamic conditions (Kim, 2010). The coronary resistance in this model was calculated by integrating data from invasive pressure and flow measurements. By integrating anatomical data from medical imaging modalities such as CT scans or MRI, the model accurately represented the patient-specific coronary anatomy, facilitating precise predictions of flow patterns and pressure gradients under varying physiological states (Kim, 2010).

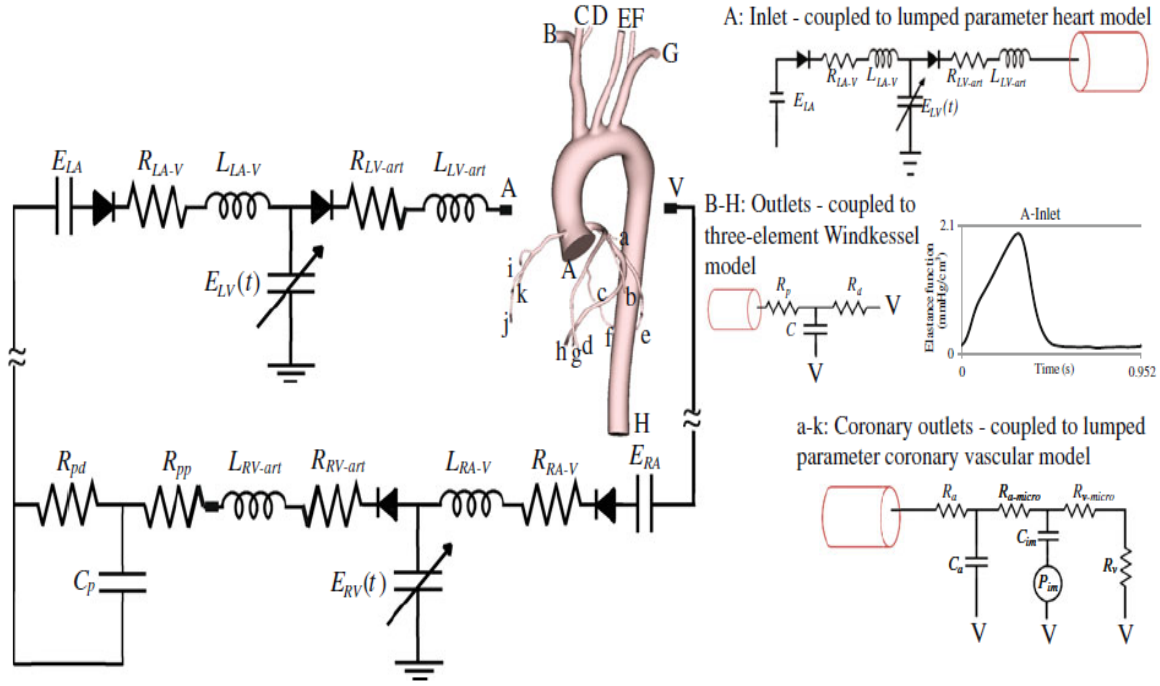

Figure 13: The integrated 3D models of the heart and arterial system to predict coronary flow and pressure developed by Kim et al. *(Kim, 2010)*.

Reduced-Order Models for Transstenotic Pressure

In the Journal of Biomechanical Engineering a reduced-order model (Figure 14) was presented which simplified the complex hemodynamics of blood flow through stenosed coronary arteries into a more manageable form. This model proposed by Mirramezani et al. (Mirramezani, 2019) focusing on the pressure drop across stenoses, in it is retains essential physiological details while reducing computational load. This approach could be particularly useful in clinical scenarios where quick, yet reliable, assessments of stenosis severity are required. The resistance values used in the model were derived from empirical data and simplified assumptions, ensuring that they reflect realistic physiological conditions while maintaining computational efficiency.

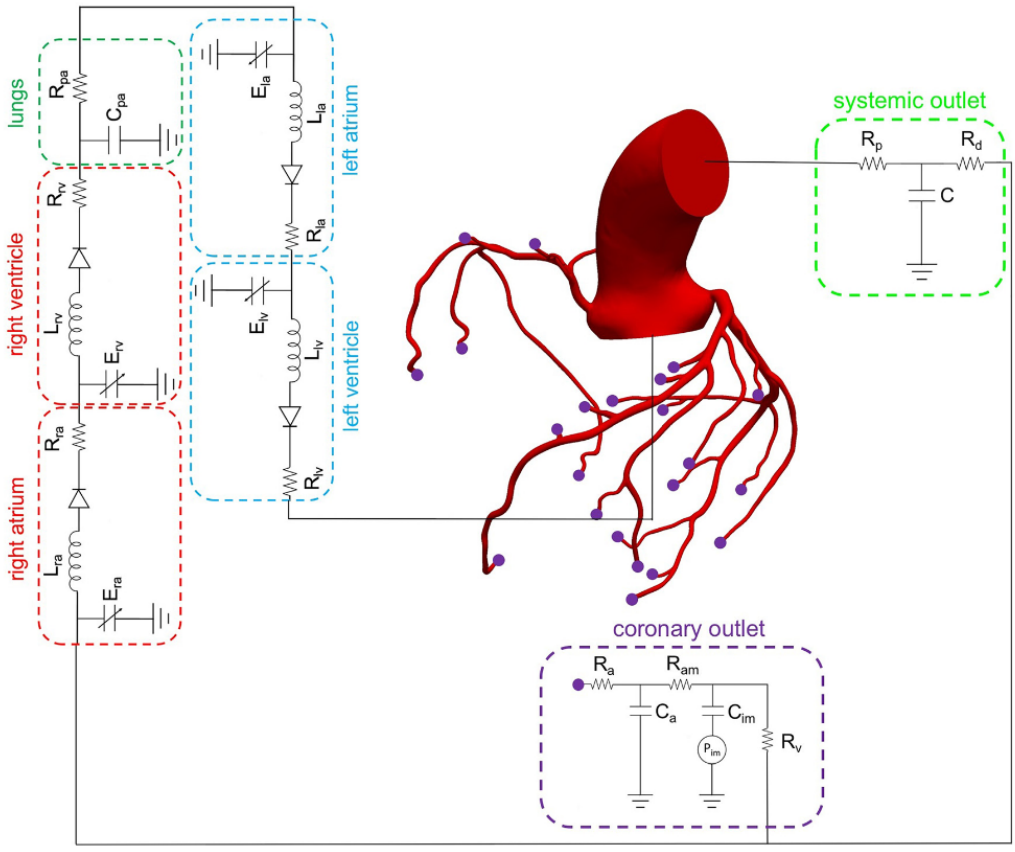

Figure 14: The Models boundary of the heart and arterial system to predict coronary flow and pressure proposed by Mirramezani et al. *(Mirramezani, 2019).*

Gaussian Process for Velocity Reconstruction in the Coronaries

A recent study explored the use of the Gaussian processes for the reconstruction of the velocity fields after coronary stenosis using positron emission particle tracking (PEPT). This model (0D model) emphasizes a non-invasive method to improve the accuracy of coronary flow measurement, leveraging advanced statistical techniques to reconstruct the complex flow patterns in stenotic regions. Using diagnostic imaging, this approach reduces dependence on direct measurement methods and enables more accurate assessments of coronary artery conditions. The resistance in coronary arteries was calculated by considering the specific geometrical and flow characteristics, which were crucial in determining the accurate velocity profiles in different coronary segments (Keramati, 2023).

Experimental Methods for Pressure Drop Evaluation

Seligman et al. in 2022 (Seligman, 2022) published their work on experimental models that replicate physiological conditions to study the hemodynamic effects of coronary stenosis. These models validate computational simulations, ensuring they accurately reflect real-life scenarios. One significant aspect of these experimental models is their ability to provide detailed insights into the resistance values that characterize the pressure drop across stenosed regions.

The study involves creating physical replicas of coronary arteries with varying degrees of stenosis and measuring the pressure and flow rates under controlled conditions. The resistance values obtained from these experiments are critical for validating computational models and ensuring their accuracy. For instance, Seligman et al. (Seligman, 2022) measured resistance values that help quantify the additional workload on the heart due to stenosis. By accurately measuring these parameters, researchers can better understand the hemodynamic impact of different degrees of stenosis and refine computational models to reflect these conditions accurately. The experimental setups often included the use of advanced imaging techniques to capture the flow dynamics within the model arteries. This data was then used to fine-tune computational simulations, ensuring that they can predict real-world scenarios with high fidelity. The resistance values derived from these experiments provide a benchmark against which computational models are validated, enhancing their reliability and applicability in clinical settings (Seligman, 2022).

Hemodynamic Characteristics in Coronary Heart Disease

Advanced imaging and CFD techniques were used to investigate the hemodynamic characteristics of patients with suspected coronary heart disease by Cao et al. By integrating these models with clinical imaging, the study highlights the importance of detailed hemodynamic analysis in guiding therapeutic decisions. The CFD models provide a comprehensive view of blood flow patterns, enabling early diagnosis and personalized treatment planning. This integration of imaging and computational modeling represents a significant advancement in non-invasive diagnostic techniques. The resistance values in these models were obtained through detailed analysis of flow and pressure data, ensuring that they accurately represent the physiological conditions of the patients. The model used to represent the boundary conditions at the aorta was a 3-element Windkessel model (Figure 15, Panel b) while for the coronaries was used a lamped parameter network (Figure 15, Panel c) (Cao, 2021).

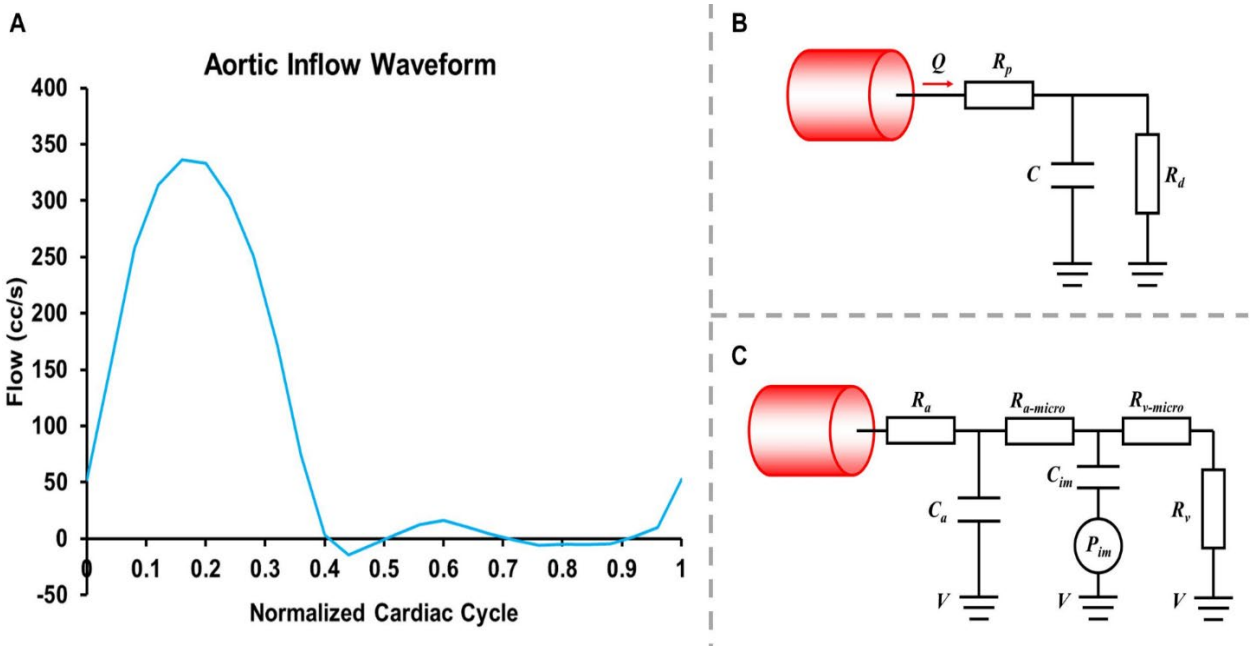

Figure 15: Inlet Flowrate wave (Panel A). Aortic boundary condition model (Panel B), where Rp is the viscous resistance of the downstream arterial vasculature and Rd the resistance of non-arterial circulation. Coronaries boundary condition (Panel C), where Ra is the arterial resistance, $R_{a\text{-micro}}$ the microcirculation resistance, and R_v is the venous resistance. C_a indicates the microcirculation compliance, C_{im} the myocardial compliance, and P_{im} is the intra-myocardial pressure *(Cao, 2021)*.

Impact of Hemodynamic Factors

In their study published in Circulation Research, Downey et al. (Downey, 1975) delve into the profound impact of hemodynamic factors on coronary artery disease. Employing advanced modeling techniques, the researchers meticulously analyze how blood flow dynamics, including shear stress and pulsatile flow, intricately influence the development and progression of atherosclerosis. Their findings underscore the critical role of understanding these hemodynamic influences in shaping arterial health. The study underscores the importance of these insights for developing effective preventive measures and therapeutic strategies aimed at mitigating the adverse effects of altered blood flow patterns. Moreover, the models developed in this research integrate detailed hemodynamic data to accurately calculate resistance values, which are crucial for predicting disease progression and optimizing treatment outcomes in clinical practice (Downey, 1975).

These are only some of the reviewed studies demonstrate the diversity and complexity of coronary artery models. From reduced-order and patient-specific models to CFD and experimental setups, each approach offers unique advantages and insights. Integrating these models could provide a comprehensive understanding of coronary hemodynamics, improving diagnosis, treatment, and prevention of cardiovascular diseases. Future research should focus on combining these methodologies to create hybrid models that leverage the strengths of each approach, ultimately enhancing the precision and effectiveness of cardiovascular healthcare.

III Section: In Vitro Coronary Artery Modeling

In vitro models are laboratory-based models studied under controlled environmental conditions. This section focuses on data measured in a laboratory coronary artery model by Mousavi (Mousavi S. M., 2024a), which reproduces the flow in the aortic root and the proximal parts of LCA and RCA, providing an opportunity for a detailed characterization of coronary artery resistances.

3.1 Description of the In Vitro Model

The in vitro model (Figure 16) comprises an anatomical mock-up model of human ascending aorta, replicating the aortic sinuses of Valsalva, LCA, RCA. The model is made of silicon, with dimensions derived from a literature analysis conducted by Mousavi to obtained normal values for the aorta in a healthy subject. To the model was integrated a three-leaflet bioprosthetic aortic valve, representing the aortic valve, ensuring realistic flow patterns in the aortic root. Physiological flow in the laboratory model is generated using a custom-designed pulsatory pump (pulse-duplicator system) (Zitti, 2023) & (Mousavi, 2024a).

The pulse-duplicator system is composed of a computer-controlled pulsatile pump (PD-1100, BDC Laboratories, Wheat Ridge, CO, USA) that simulates the left ventricle. A detailed description of the laboratory setup element is reported by Mousavi (Mousavi, 2024a). The pump is set to simulate cardiac rest conditions, included cardiac output, heart rate, and the ratio of systolic phase over the cardiac cycle period, details can be found at Mousavi et al. (Mousavi S. M., 15/09/2024-18/09/2024b).

The fluid circulating in the in vitro model is water. Since water's viscosity under normal conditions is three times smaller than blood, the pump rate was adjusted to one-third of the heart rate tom maintain similarity between the setup model and human anatomy. Pressure sensors are placed at the inlet aorta, LCA, RCA and outlet of the aorta, and a flow sensor measuring flow rate at the coronaries. During data acquisition, flow is measured at one coronary at a time.

To ensure consistent experimental conditions, a unique procedure was followed, including calibration of pressure sensors, iterative calibration of the setup resistances and compliance, and result measurements, until physiological pressure and flow were obtained to when the physiological pressure and flow were obtained. The novelty of this in vitro model is the synchronization of the measured values of pressure and flow.

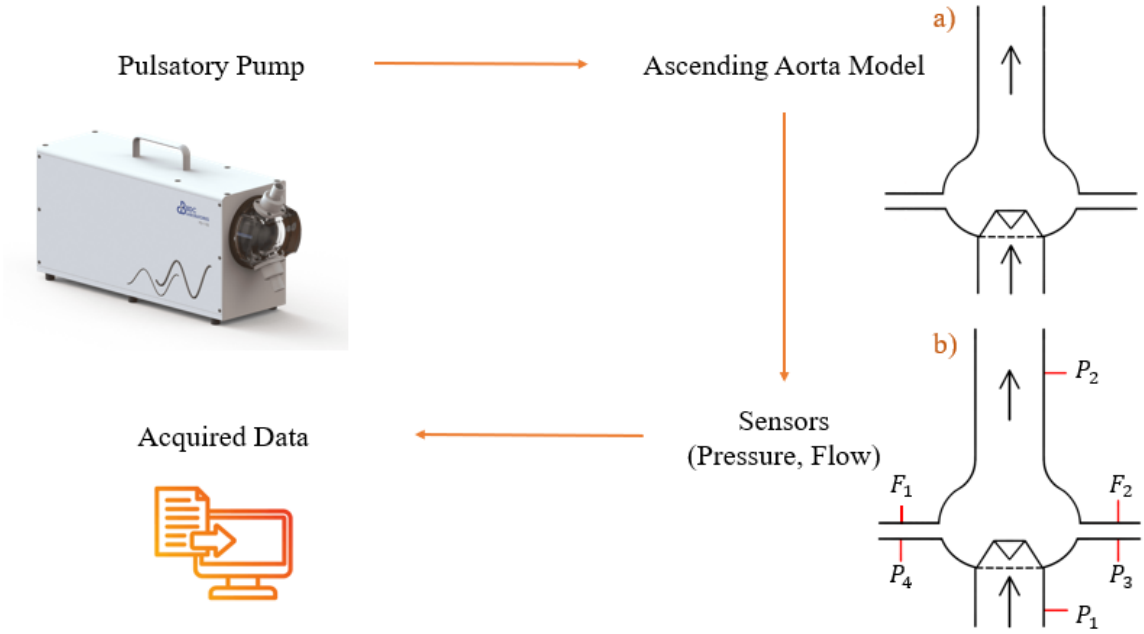

Figure 16: Schematic representation of the in vitro model components starting from the pulsatory pump and concluding with the acquired data using the pressure and flow sensors. Panel a: 2D illustration of the ascending aorta model. Panel b: red lines indicate where the pressure and flow sensors acquire data. P indicates the pressure sensor; P_1 (aorta inlet), P_2 (aorta outlet), P_3 (LCA), P_4 (RCA). F indicates flow sensors; F_1 (flow at the LCA) and F_2 (flow at the RCA).

3.2 Experimental Setup and Data Collection

Two data acquisitions were conducted to represent the healthy subject condition, each lasting for a specific duration of 15 seconds with a frequency of 2000 frames per second. Maintaining consistent experimental conditions between both acquisitions was paramount. The primary difference between these two sessions lay in the placement of the flow sensor, alternating between RCA or LCA positions to assess coronary flow dynamics.

During each session, data were simultaneously recorded and fed into a computer system. It included measurements from each pressure sensor, P_1 at the aorta inlet, P_2 at the aorta outlet, P_3 at LCA, P_4 at RCA, and the flow sensor, either F1 at LCA or F2 at RCA. The measured pressures from all four sensors are relative pressures[3]. Throughout this thesis, with the word pressure will refer to relative pressures unless otherwise specified. The recorded information was comprised in Excel files containing:

[3] Relative pressure indicates the pressure readings provided by the sensors are referenced relative to a specific baseline pressure. In this thesis, the baseline pressure is the atmospheric pressure.

- Time: recorded in seconds, marking the temporal sequence of measurements;
- Pressure: a colon for each pressure sensor measurement (P1, P2, P3, P4);
- Flow: a single colon per acquisition;
- Pump Feedback: although recorded, this data was not included in the subsequent analysis.

The experimental setup maintained consistent environmental variables and setup conditions across both data acquisition sessions, following the established protocol for the in vitro model.

3.3 Method for Data Analysis

The data acquired in a synchronized manner from the experimental model has been processed using a user-defined procedure implemented in the software MATLAB 2023b. First, for all the duration of the acquisition the data were divided in windows corresponding to each cardiac cycle. Given the extended duration of the acquired signals, four cardiac cycles were identified, each cycle with a duration of 2.6 s. To achieve this, the pressure waveform at the outlet of the aortic tube was employed considering its quasi-steady nature. Each cycle has been identified by pinpointing the minima of this waveform, corresponding to the transition from diastole to systole.

To follow for each signal across the cardiac cycle was performed the ensemble average, yielding, the averaged pressure at the aortic outlet, as well as the averaged pressures and flow for each coronary artery in their respective sessions. These ensembled average data, representing a typical cardiac cycle, were normalized into systolic and diastolic phases. The systole was considered to be only 30 % of the cardiac cycle while the diastole the remaining part taking as reference the article by Tortora et al. (Tortora, 2017).

Subsequently, the ensemble average has been calculated for pressure and flow signals across the cardiac cycles. This values where used to calculate the resistance of LCA (R_{LCA}) and RCA (R_{RCA}) throughout the cardiac cycle as the ratio of the pressure difference and the flow;

$$R_{LCA} = \frac{\Delta P_{LCA}}{Q_{LCA}} \tag{3.1}$$

$$R_{RCA} = \frac{\Delta P_{RCA}}{Q_{RCA}} \tag{3.2}$$

where Q_{LCA} and Q_{RCA} are the ensemble average flow of LCA and RCA respectively while ΔP_{LCA} and ΔP_{RCA} are the pressure gradient driving these flows. Such pressure gradients were

evaluated as the difference between the pressure value measured by the sensors placed in the coronaries (P_3 and P_4) and a reference pressure (P_{ref}), as also expressed in Eq. 3.3 and Eq. 3.4;

$$\Delta P_{LCA} = P_3 - P_{ref} \tag{3.3}$$

$$\Delta P_{RCA} = P_4 - P_{ref} \tag{3.4}.$$

The reference relative pressure was evaluated using Bernoulli's principle between a reference point representing the coronary outflow and the point where the tube simulates the coronary artery outflows in the atmosphere, obtaining;

$$P_{ref} = z\,\gamma \tag{3.5}$$

where z denotes the difference in altitude between the pressure transducer's location and the location of the outflow of the coronary tube in the atmosphere, while γ is the specific weight of the fluid. By definition, γ is the product of the gravitational acceleration (g) and the fluid density (ρ). Subsection 3.3.1 provides a detailed explanation of how the P_{ref} was obtained.

However, this procedure for the evaluation of the R_{LCA} is not valid for the entire cardiac cycle, due to a backflow during the first part of the systolic phase. To identify this phase the resistance has been evaluated using Eq. 3.1 and Eq. 3.2. The ensembled average waves of P and Q of LCA were filtered using a 4th-order Butterworth filter with a cutoff frequency of 70 Hz. The filtered signal of the evaluated resistance allowed for identification of the first and last divergent times of the resistance. The filtering of the data was applied also to the data needed to calculate the R_{RCA}.

3.3.1 A Method for Calculating the Reference Pressure using Bernoulli's Equation

For the calculation of the P_{ref} was used Bernoulli's Principle (D. A. Rubenstein, 2022), which states that for an incompressible, frictionless fluid, the total mechanical energy along a streamline is constant. Such principle represents the conservation of energy for flowing fluids and can be mathematically expressed as:

$$P + \frac{1}{2}\rho v^2 + \rho g z = constant \tag{3.6}$$

where P is the static pressure of the fluid, ρ the density of the fluid, v the flow velocity, g the acceleration of gravity and z the height about a reference point.

Dividing Eq. 3.6 by γ (where $\gamma = \rho g$) gives the following equation:

$$H = z + \frac{v^2}{2g} + \frac{P}{\gamma} \tag{3.7}$$

where H is the constant head. In the in vitro model, the area immediately downstream of the pressure sensor, corresponding to the coronaries and the point open to the atmosphere, are considered as two points for applying Bernoulli's equation. Applying the appropriate substitutions in Eq. 3.7 for these two points, is obtained;

$$H_{in} = 0 + \frac{v^2}{2g} + \frac{P_{ref}}{\gamma} \tag{3.8}$$

$$H_{atm} = z + \frac{v\prime^2}{2g} + \frac{P_{atm}}{\gamma} \tag{3.9}$$

where H_{in} is the initial position (near to the coronaries pressure sensor) and the reference point for the height is set such $z = 0$. While Eq. 3.9 corresponds to the point where the model is in direct contact with the atmospheric pressure (P_{atm}). Considering the relative pressure, the contribution of atmospheric pressure, $P_{atm,}$ Eq. 3.9 disappears:

$$H_{atm} = z + \frac{v\prime^2}{2g} \tag{3.10}$$

Because of continuity on a vessel with negligible variation of the cross-section area, it can be assumed that:

$$\frac{v^2}{2g} = \frac{v\prime^2}{2g} \tag{3.11}$$

According to Bernoulli's equation, it follows that:

$$H_{in} = H_{atm} \tag{3.12}$$

$$\frac{P_{ref}}{\gamma} = z \tag{3.13}$$

Substitution of Eq. 3.8 and Eq. 3.10 into Eq. 3.12 provides Eq. 3.13 from which P_{ref} can be derived, as introduced in Eq. 3.5 in the previous section.

3.4 Results

The measured values relative to LCA are reported in the first three panels of Figure 17 with different colors for each different cycle, while the ensemble averaged cycle is depicted in black. The time cycle is expressed on a normalized time scale from 0 to 1. The fourth panel of Figure 17 reports the resistance of the LCA (R_{LCA}) during for the ensemble average cycle, excluding the contraction phase.

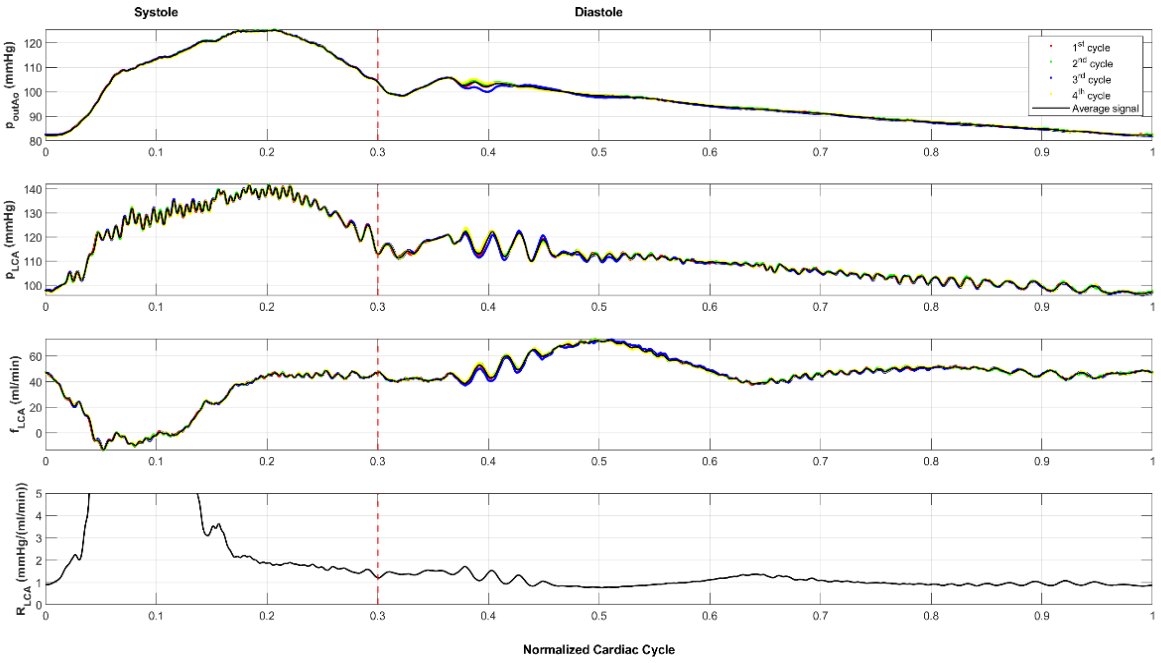

Figure 17: First panel: pressure at the outlet of the aorta (p_{outAo}). Second panel: pressure in the left coronary artery (p_{LCA}). Third panel: flow in the left coronary artery (f_{LCA}). Measured data for each cardiac cycle are represented by dots in four distinct colors. The ensemble averaged values, computed across all cycles, are depicted in black. Fourth panel: R_{LCA} throughout the cardiac cycle. The vertical dashed line gives the systolic and diastolic phases of the cardiac cycle.

Similarly, for RCA, Figure 18 presents the measured values across different cardiac cycles with the ensemble averaged cycle shown in black. This figure mirrors the structure of Figure 17, providing a comprehensive view of RCA behavior across the modelled cardiac cycle.

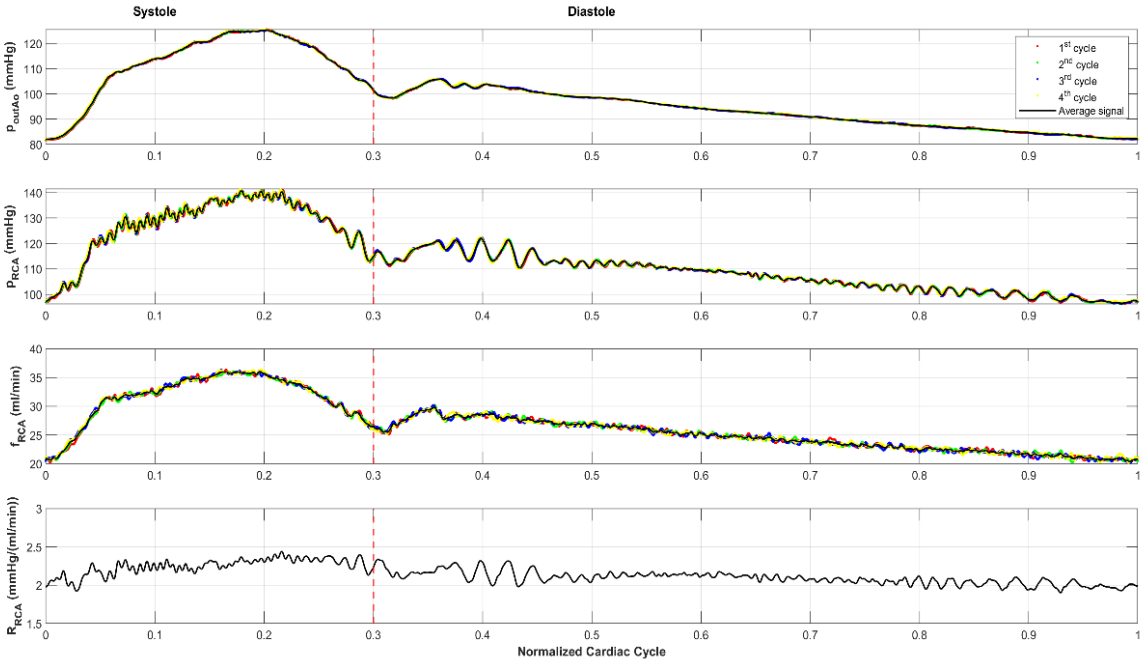

Figure 18: First panel: pressure at the outlet of the aorta (p_{outAo}). Second panel: pressure in the right coronary artery (p_{RCA}). Third panel: flow in the right coronary artery (f_{RCA}). Measured data for each cardiac cycle are represented by dots in four distinct colors. The ensemble averaged values, computed across all cycles, are depicted in black. Fourth panel: R_{RCA} throughout the cardiac cycle. The vertical dashed line gives the systolic and diastolic phases of the cardiac cycle.

Figure 17 and Figure 18 not only report in the first three panels the values of pressure in correspondence of the aorta and coronaries, as well as the flow in each coronary artery but also in the last panel, the resistance R_{LCA} and R_{RCA} respectively.

From Figure 17 it is worth noting that the pressure wave of the LCA follows the same pattern of the pressure wave at the output of the aorta, as expected physiologically. Meanwhile, the LCA flow decreases during systole, reaching a minimum at 0.067 of the cardiac cycle before increases again. This phenomenon observed from the experimental data is known as systolic compression or systolic impediment, which has as a result a backflow in the early systole phase. The backflow is attributed to the model's transmission of contraction effects to the distal LCA, thereby invalidation the reference pressure definition provided by Eq. 3.5. Physiologically, systolic compression occurs because during the contraction of the left ventricle, the intramural coronary vessels are compressed, reducing blood flow through the LCA, leading to really high values of the R_{LCA}.

The filtered signal of the evaluated resistance, obtained using the Butterworth filter of order 4 with a cutoff frequency equal to 70 Hz as explained in the previous subsection, facilitated the identification of the initial and final divergence points. Using the filtered signal of P and Q, the resistance was calculated, which helped pinpoint the first to maximum values corresponding exactly with the beginning and end divergency points. Specifically, these points correspond to the beginning of the isovolumetric contraction phase at time 0.042 of a normalized cardiac cycle and the end of the contraction at time 0.12 of a normalized cardiac cycle, spanning approximately one-third of the systole duration. This time information indicates that the contraction phase constitutes 26% of the entire systolic phase, and 7.8% of the entire normalized cardiac cycle.

Notably, the observed backflow did not align with the peak aortic pressure but with its rapid rise (Figure 17, first and third panel). What is also important is that the starting of the isovolumetric contraction phase leads to a surge in LCA pressure (second panel of Figure 17) and a subsequent reduction in LCA flow (third panel of Figure 17). Once the contraction phase was concluded, it is accompanied by a reversal phenomenon.

Similarly to what has been shown for the LCA in Figure 17, in Figure 18 is reported for RCA. It should be noted that, similar to LCA, the pressure in RCA follows a pattern similar to the pressure at the aorta outlet (first and second panel Figure 18). However, in this case, that same pattern is recognized also in the flow profile (third panel Figure 18). There is no influence of

any isovolumetric contraction, so the resistance for the RCA (R_{RCA}) as presented in panel 4 of Figure 18, was calculated using Eq. 3.2 defined in subsection 3.3. The evaluated R_{RCA} persisted within the range of 1.5 to 2.5 mmHg/(ml/min).

Following as reference the results of the article by Goodwill et al. (Goodwill, 2018), it was possible for the acquired data to show the relationship between pressure at the outlet of the aorta and flow in the RCA and LCA, illustrated in Figure 19. This figure visually represents how coronary blood flow in the LCA and RCA varies with changes in aortic outlet pressure, highlighting different phases of the cardiac cycle, described in detail in the figure capture. Figure 20 includes linear fitting lines for four specific phases of cardiac cycle, two relatives to RCA (diastolic and systolic phases, in cyan and magenta respectively) and other two relative to the LCA (systolic phase before and after the contraction, in black).

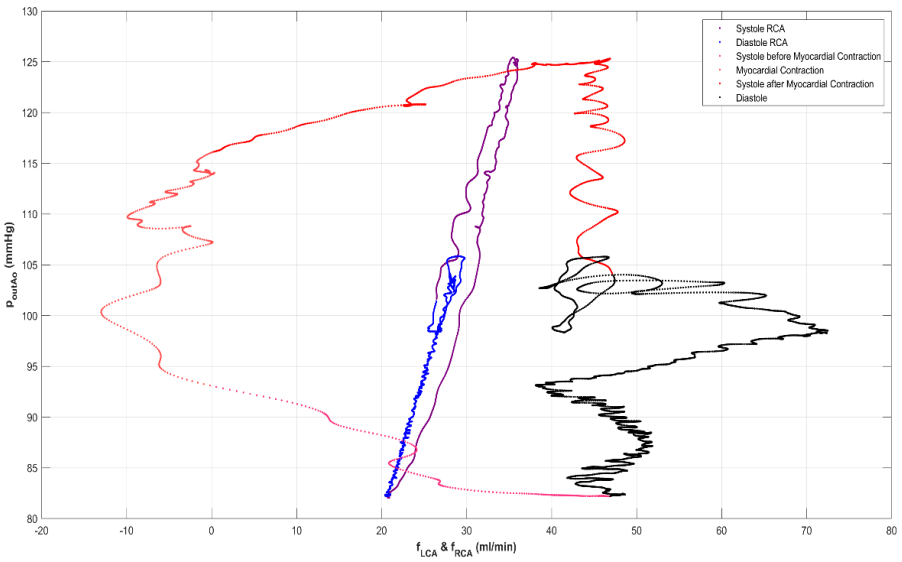

Figure 19: Illustration of the existing relationship between coronary blood flow in LCA (f_{LCA}) and RCA (f_{RCA}) with the aortic outlet pressure (p_{outAo}). In purple dotted line: Systole in RCA. In blue dotted line: Diastole in RCA. In pink dotted line: Systole before myocardial contraction in LCA. In light red dotted line: Myocardial contraction. In intense red dotted line: Systole after Myocardial contraction in LCA. In black dotted line: Diastole in LCA.

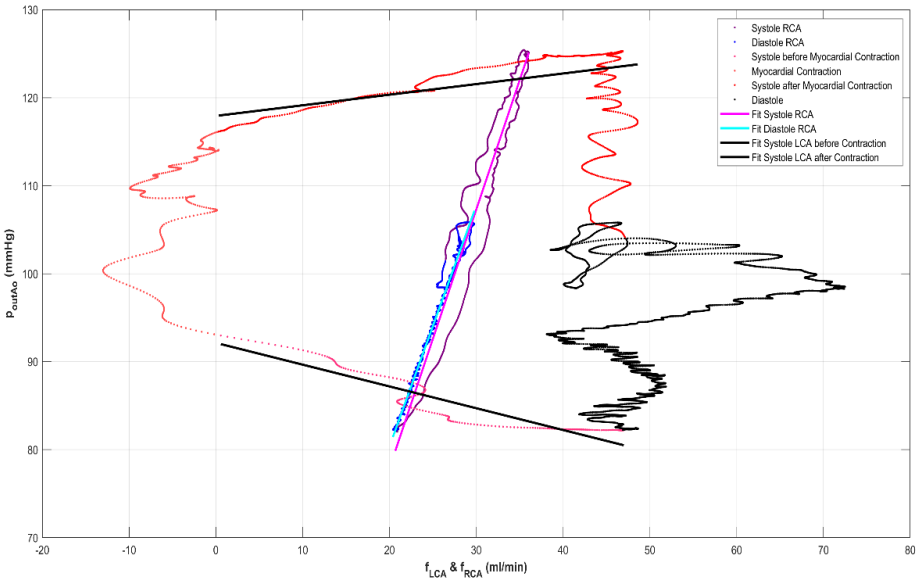

Figure 20: Illustration of the existing relationship between coronary blood flow in LCA (fLCA) and RCA (fRCA) with the aortic outlet pressure ($p$outAo). In purple dotted line: Systole in RCA. In blue dotted line: Diastole in RCA. In pink dotted line: Systole after Myocardial contraction in LCA. In black dotted line: Diastole in LCA. Linear fit lines are shown in different colors for different cardiac phases. Magenta line: fit for systole in RCA. Cyan line: fit for diastole in RCA. Two black lines: fit for LCA before and after the contraction phase.

In Table 1 are summarized the time-average values of the resistance obtained from both the LCA and RCA. The mean resistance values were specifically assessed during both the systolic and diastolic phase. Notably, for the LCA, a distinction was made between systole, distinguishing the phase when the myocardial contraction was observed and those when it was not.

Table 1 provides a comprehensive summary of the useful data crucial for defining, in the subsequent section of the thesis, a Windkessel-type boundary conditions, specifically for the computational model development.

Table 1: The Mean resistance value for the LCA and RCA.

LCA	Resistance	Mean Value (mmHg/(ml/min))
	Systole phase	18.75
	Systole phase (without myocardial contraction)	1.65
	Peak value during myocardial contraction	2400
	Diastole phase	1.05
RCA	Resistance	Mean Value (mmHg/(ml/min))
	Systole phase	2.25
	Diastole phase	2.09

3.5 Discussion and Interpretation

The results reported in the previous subsection (Results 3.4) come after an experimental data analysis performed in MATLAB 2023b. The goal of this analysis is to estimate the resistance faced by the fluid while passing in the coronary arteries tubes, in different phases, for possible application in electrical modeling for the coronary system. As described in subsection 3.2, a user-defined procedure was used to obtain the resistance for each coronary artery during a normalized cardiac cycle. The plot of the resistances for both coronary tubes are displayed in panel 4 of Figure 17 and Figure 18.

In the final panel of Figure 17, is depicted the $R_{LCA.}$ Analyzing the flow profile during the systole there is a range corresponding to the myocardial contraction, where the resistance value diverged significantly. This observation highlighted the inadequacy of applying the simple definition of the resistance expressed in Eq. 3.1 across the entire cardiac cycle. To emulate the R_{LCA} evaluated from laboratory measurement, it was necessary to distinguish the contraction phase and then calculate R_{LCA}, during and out of the contrition using Eq. 3.1. The evaluated R_{LCA} out of myocadiac contraction persisted within the range 1 to 2 mmHg/(ml/min), both during the systolic phase (out of the isovolumetric contraction), and during the diastolic phase. However, during the isovolumetric contraction, characterized by a swift increase in pressure followed by a rapid decline of the flow within the LCA, the R_{LCA} escalates markedly, peaking at values above 2400 mmHg/(ml/min) at time 0.1 of the normalized cardiac cycle, as reported in Table 1.

Regarding the RCA, there is no influence of the isovolumetric contraction. Therefore, the resistance for the RCA (R_{RCA}, presented in panel 4 of Figure 18) was calculated using Eq. 3.2 defined in subsection 3.3. The evaluated R_{RCA} remained within the range of 1.5 to 2.5 mmHg/(ml/min).

The relationship between the outlet pressure of the aorta and the coronary flow, illustrated in Figure 19 and Figure 20, is important to understand the impact that the aortic pressure has on the coronary flow. As expressed by Goodwill et al. (Goodwill, 2018), this relationship is consistently present and can be observed when data acquisition is synchronized. In this in vitro laboratory model, such synchronization is satisfied.

In Figure 19 the first thing to notice is the different shapes of aortic pressure and coronary arteries data. By applying a linear fitting curve to regions where the data distributions appear linear can be informative about how the resistance changes as shown in Figure 20. A linear

relationship between coronary artery flow and aortic pressure underscores the choice of a constant resistance in the computational model development phase. Since resistance is a key in the fluid computational model, it is essential to understand its behavior throughout the cardiac cycle and represent it accurately in the computational model to simulate realistic conditions.

For the RCA, during both systole and diastole, the distribution of the data in Figure 19 appears linear. Therefore, in Figure 20, two curves corresponding to each phase are overlapped on the data. It is noticeable that the two curves are almost overlapped so with similar slope. This indicates that a single constant resistance can be used to estimate the fluid structure interaction of the RCA with an electrical model, considering the time evolution of the resistance values for the entire cycle shown in panel 4 of Figure 18, the mean value of the entire cycle is well-suited for use in the computational model to define boundary conditions for the RCA.

For the LCA, the only parts of the data distribution where the linear fitting curve could be applied where during the systole, but out of the contraction, as depicted in Figure 20. Notably, the two fitting curves obtained have opposite slopes, with similar inclinations, suggesting that these two intervals are characterized by the same resistance, with flow in different directions. In fact, the beginning of the contraction can generate a short small backflow in the coronary. This graphic analysis of the relationship existing between the aortic pressure and the flow in the coronaries does not support the selection of a unique resistance within an electrical model to replicate the LCA behavior.

Since a single constant resistance is insufficient for the myocardial contraction phase, an additional resistance should be introduced to account for myocardial contraction. Like the RCA, Table 1 are provides the mean resistance values for the LCA, which will be instrumental during the model development phase. In the modeling phase for the contraction, the peak value during systole will be used but not only also the mean value of the resistance for all the cycle expects the myocardial contraction, and outside the contraction phase, only the mean value of the resistance for all the cycle expects the myocardial contraction.

In summary, in Table 1 are provided the following information, which used to define the boundary condition for the CFD model:

- the mean value of the R_{LCA} during the systole, equal to 18.75 mmHg/(ml/min) considering also the contraction phase,
- the mean value of the R_{LCA} out contraction the mean value, equal to 1.65 mmHg/(ml/min),

- the mean value of the R_{LCA} during diastole, equal to 1.05 mmHg/(ml/min),
- the mean value of the R_{RCA} during the systole, equal to 2.25 mmHg/(ml/min),
- the mean value of the R_{RCA} during the diastole, equal to 2.09 mmHg/(ml/min).

Overall, this detailed analysis of the coronary resistance across different cardiac phases is pivotal for developing a comprehensive and accurate computational model, which will enhance our understanding and simulation of coronary hemodynamics. the mean resistance values obtained for each phase will be elaborated in three key constant resistances, which will be used in two Windkessel-type models to estimate the coronary outflow as boundary condition for the simulation model. The three resistance values which will be used in the next section and that are calculated from the values in Table 1, are:

- for the RCA, the mean resistance value considers the entire cycle, averaging systolic resistance and diastolic one, equal to 2.17 mmHg/(ml/min),
- for the LCA during the myocardial contraction, the peak corresponding to the peak of the systole, equal to 2400 mmHg/(ml/min),
- for the LCA outside the myocardial contraction, the resistance value is the averaging systolic resistance outside the contraction and diastolic one, equal to 1.35 mmHg/(ml/min),

Moreover, understanding the dynamics of pressure and flow in the ascending aorta model can help in accurately modeling the physiological and responses of coronary circulation. By benefitting from synchronized measures, it was possible to explore potential relationships between the data and how these correlations influence the resistance encountered by the fluid flow through the coronary arteries.

IV Section: Model Development and Application

This section will describe the methodology for utilizing the results obtained from the experimental data in the previous section to set the boundary conditions for a CFD model of the in vitro laboratory setup described in Section III (3.1). Specifically, it will be discussed how to derive appropriate boundary conditions that align with the results observed in the laboratory model, ensuring an accurate representation within the CFD. Two numerical simulations will be compared: one using as boundary conditions directly the measured experimental data and another one with the proposed boundary conditions, based on the Windkessel parameterization, with the aim of validating the proposed boundary conditions.

In accordance with the CFD models described in Section II (2.1.1), the workflow will be defined in three key steps:

- Pre-Processing
- Solver
- Solution.

Each of these steps will be explained upon in dedicated subsections. These processes will be performed using the software Ansys 2024 R1, more specifically in the toolbox Ansys Fluent 2024 R1.

4.1 Pre-Processing

Definition of the Geometry

The pre-processing step starts with the definition of the 3D geometry representing the in vitro model, without the presence of the aortic valve. As for the experimental data, also the geometry is a 3D drawing again provided by Mousavi, and more details of each can be found in (Mousavi S. M., 2024a). Figure 21 represents the 3D geometry created using the software SpaceClaim 2024 R1 (Ansys 2024 R1).

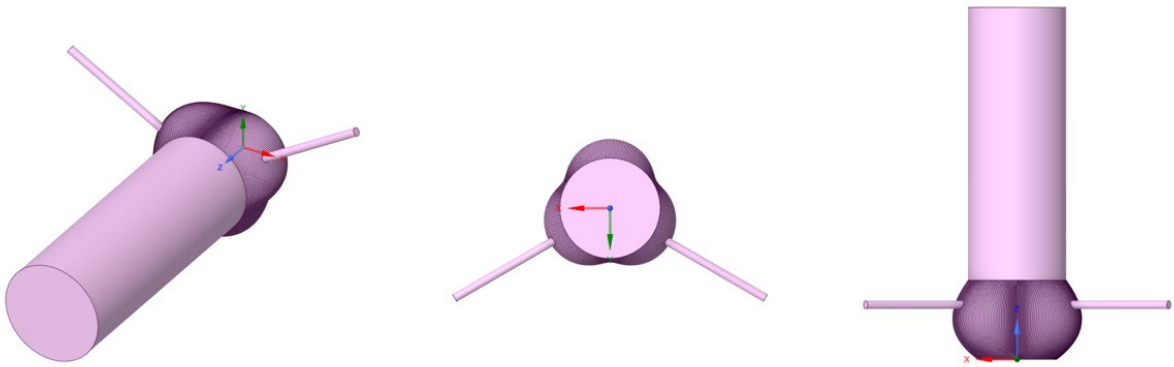

Figure 21: 3D geometry of the in-vitro model representing the ascending aortic root. First panel: an isovolumetric view of the geometry. Second panel: a top view (plain view) of the geometry. Third panel: a frontal view of the geometry (Mousavi S. M., 2024a)

Meshing

Once the geometric model of the computational domain was defined, the next step in the preprocessing phase was meshing. Meshing involved dividing the computational domain into small, geometrically defined elements or cells, in order to solve then the governing equations of the fluid flow in correspondence of each cell.

In the specific case of this project, meshing was performed in Fluent Meshing, a build-in tool already presents in Ansys Fluent 2024 R1. This tool offers robust capabilities for generating both structural (Cartesian) and unstructured meshing decided by default by the software.

- Geometry Import and Cleanup

  The geometry from the previous step was imported into Meshing Fluent tool. To follow a geometry cleanup was performed to remove any small features or defects that could bring complications in the meshing process. It included merging faces, eliminating tiny edges and ensuring the connectivity between parts.
- Defining Meshing Parameters

  The default element size was set to 9.0514×10^{-3} m (9.0514 mm) and it was selected a mesh type called hexahedral (hexes), being efficient in solving fluid dynamics problems due to their structural arrangement and ability to conform well in the computational domain.
- Mesh Generation

  Automatic Meshing Algorithm: once the parameters where set the software's automatic meshing algorithm was employed, which in an autonomous way adapted the mesh

density based on the geometry of the fluid. Resulting in a mesh of 343011 elements and 68700 nodes, ensuring a balance between computational efficiency and solution accuracy.

- Mesh Quality Improvement

  Smoothing Techniques: A medium smoothing technique was applied to improve the mesh quality, ensuring that it conforms the model geometry and provides reliable results. Smoothing remains an essential key in avoiding highly skewed or distorted elements, which can lead to numerical inaccuracies and convergence issues.

In Figure 22 is shown the meshed geometry from different point of view. Figure 23 depicts the mesh once performed a cross-section of the geometry, enhancing the visualization of its internal structure.

- Surface Meshing for Coronary Tubes

  Refinement of Surface Mesh: A targeted surface meshing was applied to the coronary tubes (Figure 24). This consisted in refining the surface mesh with an element size of 2.2629×10^{-3} m. Surface refinement is important for an accurate capturing if important flow characteristics near the walls, especially where the geometry is complex or a high gradient is to be expected. The finer the mesh resolution is the more it helps in detecting valuable flow details and ensures higher fidelity in the simulation results.

- Mesh Validation and Finalization

  Quality Check: The default quality check was performed to ensure that the mesh met the required standards. For a small number of poor- quality elements the mesh was further refined and adjusted based on the quality check results.

Finally, the choice of element size, refinement strategies play an important role as they will directly affect the resolution and accuracy of the simulation to follow. For this specific case, being a simplified representation of the real ascending aorta, the low number of cells should have a minimal influence on the final results.

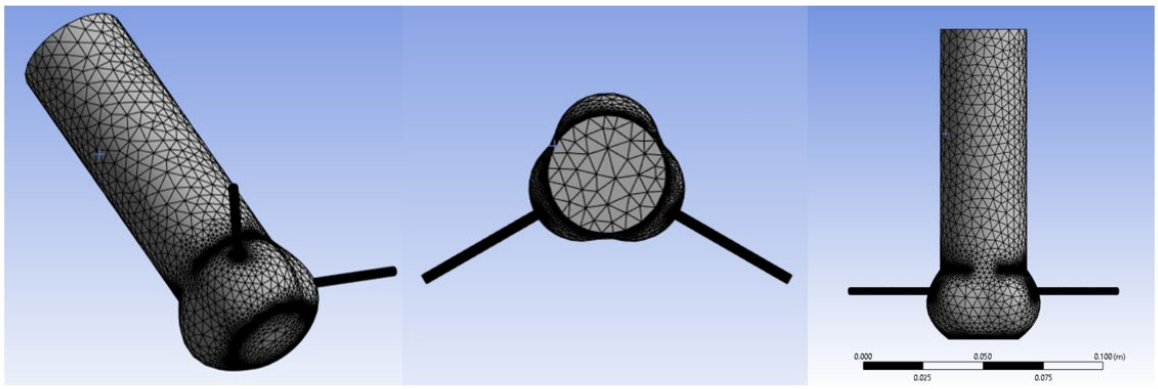

Figure 22: The meshed geometry from three different prospectives, isovolumetric view, planar view and a frontal view.

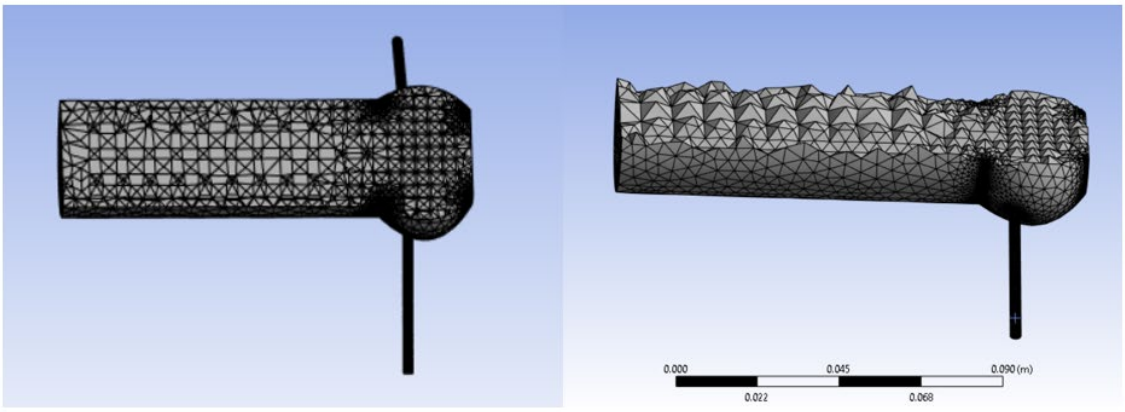

Figure 23: The first panel provides a 2D cross-section view of the meshed geometry. The second panel presents the same cross-section with a 3D representation of the cells.

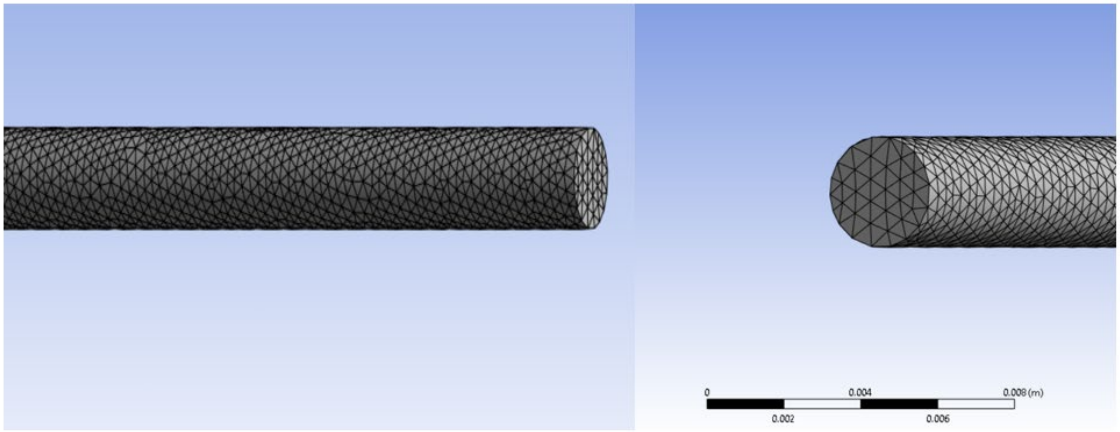

Figure 24: Both panels depict a zoomed-in view of the geometry near the coronary artery tube, highlighting the application of a surface meshing being applies.

Material Properties

In this simulation was to replicate the laboratory model of the aortic root, which works with water. The density of the material was 980 kg/m^3 and the viscosity 1.002 × 10^{-3} Pa· s at 20 degrees Celsius. These properties are available in the Fluent database under "water-liquid," and the viscosity is set to be laminar.

Boundary Conditions

The definition of the boundary conditions varies depending on the physical phenomenon being modeled. In this particular case, the phenomenon to be modelled is the behavior of fluid within the in vitro laboratory model. Therefore, the boundary conditions are defined in terms of pressure and mass flow rate. The definition of the boundary conditions plays a critical role in the computational fluid domain solver, as they provide essential information on how the fluid interacts with the surfaces within the model. In this work, two different sets of boundary conditions were defined. For the first simulation, the boundary conditions were time-series of data directly taken from the experiment. For the second simulation, proposed boundary conditions were applied at the coronary tube. The choice to use two sets of boundary conditions aimed to provide initial validation of the proposed conditions, assessing how closely they replicated the real model output.

It is important to distinguish between the inlet and outlet surfaces within the computational domain. The inlet surfaces represent the points where the fluid enters the computational domain while the outlets are where fluid exits.

1. All-measured Boundary Conditions

In the first simulation the idea was to faithfully replicate exactly the experimental scenario. So as boundary condition where used the acquired data describes in Section III (3.2).

- Inlet Face (Aorta Inlet)

  The boundary condition at the inlet face was a pressure time series corresponding to two cardiac cycles, which was measured during the data acquisition sessions (Figure 25, second panel).

- Outlet Face:
  - Aortic Root End: the boundary condition was a pressure time series that also spanned two cardiac cycles. This boundary condition ensured that

the fluid behavior at this critical exit point is accurately simulated (Figure 25, first panel).

- Coronary Tubes Ends (Two Outlets): the boundary conditions were defined based on the measured outflows during the experimental phase. To be introduced to the Fluent solver this have to be expressed in terms of mass flow rate, reflecting the mass of the fluid exiting these specific outlets over time (Figure 25, third and fourth panel).

➢ Wall (Outside of the Geometry)

The boundary condition applied was no-slip condition. This condition mandates that the fluid velocity at the walls is zero, simulating the effect of the fluid adhering to the wall surfaces and preventing any relative motion.

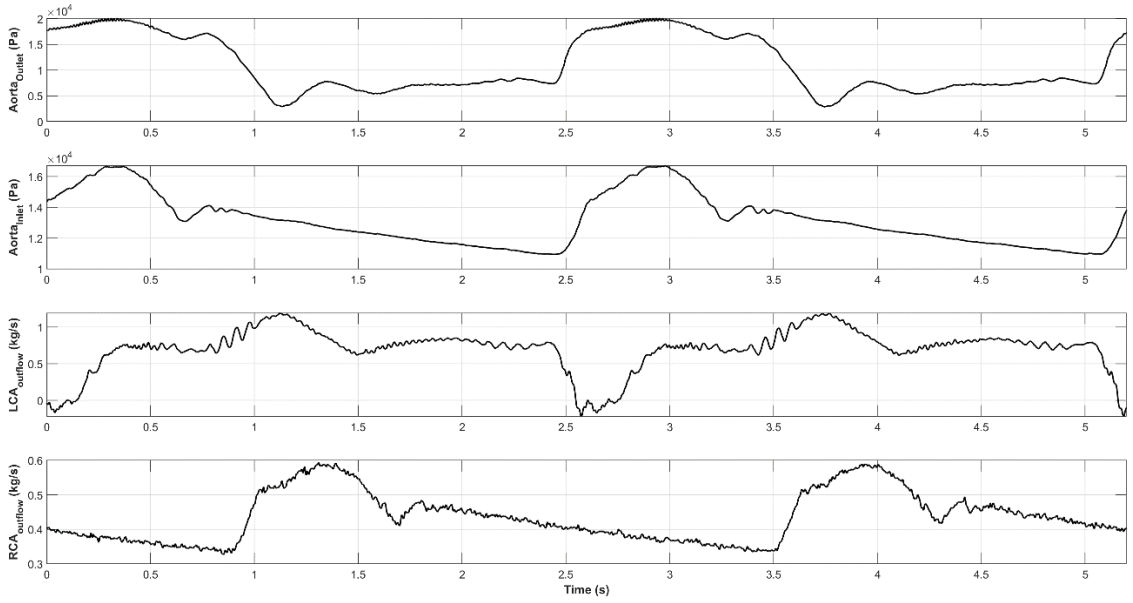

Figure 25: The time series used as boundary conditions for the first simulation. First Panel the outlet pressure at the aorta. Second Panel the inlet pressure at the aorta. The third and fourth panel show the outlet flow at the coronaries as a mass flow rate.

2. *Measured-modeled Boundary Conditions*

For the second simulation, boundary conditions at the coronaries were established based on detailed characterizations of the fluid resistance encountered within the coronary tubes, as outlined in Section III. To ensure comparability with the results from the first simulation, the boundary conditions at the inlet and aorta outlet were the acquired experimental data, maintaining consistency in their characterization (Figure 25, first and second panel). Also, the wall conditions remain unchanged. Instead, the coronary mass flow rate is derived incorporating the resistance values described in Section III, exploiting a Windkessel model both in the RCA and LCA. A detailed explanation on how the mass flow rate was derived using the Windkessel model at the RCA and LCA is provided in subsection 4.1.1.

Thus, the two key modifications in boundary conditions for this simulation pertained to the coronary tubes:

- Outlet Coronary Tube Face:

  RCA: the boundary condition applied was a mass flow rate obtained from the application of a 2-element Windkessel model. Further details regarding this modeling approach are elaborated in subsection 4.1.1.

  LCA: the boundary condition applied was a mass flow rate derived from two distinct Windkessel models:

  - A 2-element Windkessel model implemented both before and after the myocardial contraction.
  - A 3-element Windkessel model during the contraction.

  Detailed explanation of these modeling methodology is provided in subsection 4.1.1.

4.1.1 Boundary Conditions Method in the Coronary Tubes using Windkessel Model

The analysis performed using the experimental data in Section III, allows for the identification of representative, resistance values during a normalized cardiac cycle for both the LCA and RCA. The mean resistance values used are provided in Section III (3.5). The Windkessel model parameters were used to include these resistance values in the boundary conditions of coronary arteries. As explained in Section III, there is a distinction if using a single constant resistance

or two resistances, this because the behavior of the RCA requires a model with a single resistance, while the behavior of the LCA necessitates a model with two resistances.

RCA outflow boundary condition (2-element Windkessel Model)

The RCA mean resistance during both the cardiac phases was found to be representative for the whole cardiac cycle. Given this, it was deemed appropriate to represent the boundary conditions at the RCA using a 2- element Windkessel model. This model consists of a resistance ($R_{RCA,mean}$) and a compliance (C_{RCA}). This 2-element Windkessel model is used to capture the behavior of the RCA by relating the pressure (P_{RCA}) obtained from the experimental data to the flow in RCA ($Q_{RCA}\,(t)$). The electrical representing circuit is shown in Figure *26*.

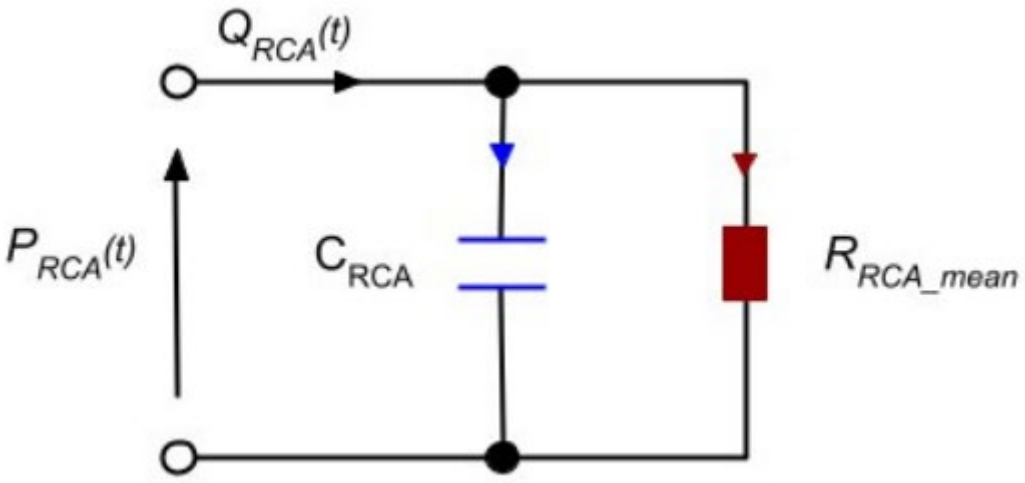

Figure 26: 2-element Windkessel model applied to the RCA during the entire cardiac cycle.

The equation for the 2-element Windkessel model is derived, starting from the 3-element Windkessel model eq. (2.11). In this model, R_{RCA_mean} is considered as the distal resistance (R_2) from the 3-element Windkessel model, while the proximal resistance (R_1) is assumed to be zero, obtaining:

$$Q_{RCA}(t) = \frac{P_{RCA}(t) - P_{RCA,out}}{R_{RCA,mean}} + C_{RCA}\frac{dP_{RCA}(t)}{dt} \tag{4.1}$$

where R_{RCA_mean} is the mean value resistance continuously acting on the experimental model, and C_{RCA} denotes the compliance in the RCA tube, P_{RCA} is the pressure measured by the sensor while P_{RCA} referred as P_4 in eq. 3.4, and $P_{RCA,out}$ is the reference pressure (P_{ref}) in eq. 3.4.

To apply this model efficiently C_{RCA} needs to be known. The method used to estimate C_{RCA} was implemented in MATLAB 2023b, for the given R_{RCA_mean} involved using a for loop to iterate C_{RCA} values ranging from 0.001 to 1 ml/mmHg, with a resolution equal to 0.001 ml/mmHg, taking as reference the physiological values provided by Chemla (Chemla, 1998). Each estimated $Q_{RCA}(t)$ was then compared with the real value from the experimental data by calculating the standard deviation of each obtained result. The value of C_{RCA} providing the lowest standard deviation was selected as the optimal compliance, which in this case was C_{RCA} = 0.6860 ml/mmHg with a standard deviation equal to 1.7013. A low standard deviation indicates that the estimated flow closely matches the real data.

The estimated $Q_{RCA}(t)$ was then evaluated using Eq. 4.1 and saved as a time series after being converted in a mass flow rate, changing from ml/min to m^3/s, and then multiplied by the density of the fluid (980 kg/m^3). This conversion ensures that the flow rate is expressed in standard units used in fluid dynamics simulations, making it compatible with other components of the model.

Figure 26 illustrates the results of this estimation, where the estimated flow using the 2-element Windkessel model is overlapped with the experimental flow. The resistance R_{RCA_mean} was found to be 2.17 mmHg/(ml/min), and the optimal C_{RCA} was 0.686 ml/mmHg.

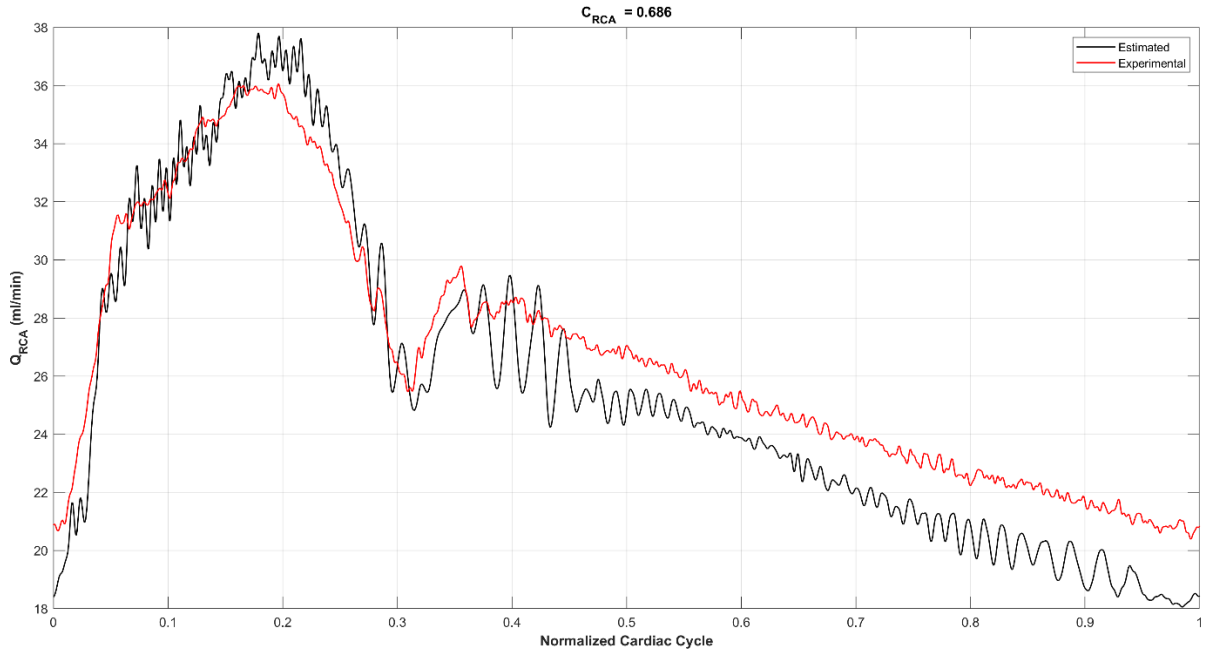

Figure 27: 2-element Windkessel model applied to the RCA before and after the myocardial contraction.

LCA outflow boundary condition (2-element and 3-element Windkessel model)

The LCA experimental data analysis (Section III) shows a consistent resistance encountered by the fluid while passing through the tube throughout part of the cardiac cycle, similar to the resistance observed in the RCA. Additionally, there is a higher resistance value during the myocardial contraction phase. Due to these observations, two different Windkessel model were applied during these two phases, unlike the RCA.

Out of the contraction phase, the mean resistance for th LCA was clearly identifiable, making the 2-element Windkessel model suitable for this part of the cardiac cycle. As with the RCA, the flow $Q_{LCA}(t)$ was estimated from the pressure data. To obtain $Q_{LCA}(t)$ a compliance value (C_{LCA}) had to be found with exactly the same approach followed in the RCA boundary condition. The equation of the 2-element Windkessel model used to obtain the flow time series at the LCA before and after the myocardial contraction is as follows:

$$Q_{LCA}(t) = \frac{P_{LCA}(t) - P_{LCA,out}}{R_{LCA,mean}} + C_{LCA}\frac{dP_{LCA}(t)}{dt} \tag{4.2}$$

where R_{LCA_mean} is the mean value resistance continuously acting on the experimental model, and C_{LCA} denotes the compliance in the LCA tube. P_{LCA} is the pressure measured by the sensor, referred to as P_3 in eq. 3.3, while $P_{LCA,out}$ is the reference pressure (P_{ref}) in eq. 3.3. The value

of C_{LCA} that provided the lowest standard deviation was 0.6 ml/mmHg with a standard deviation equal to 1.503, and R_{LCA_mean} before the contraction was 1.45 mmHg/(ml/min).

During the contraction phase, the resistance reached significantly high values, heavily influenced by the contraction. For this reason, it was deemed appropriate to use a 3-element Windkessel model to represent the LCA behavior during the contraction phase (Figure 28). In this model, derived from eq. 2.11 R_1 is assumed to be equal to the resistance due to contraction ($R_{LCA.contr}$), while R_2 corresponds to $R_{LCA,mean}$. Making the right substitutions to eq. 2.11. is obtained:

$$Q_{LCA}(t)\left(1 + \frac{R_{LCA,contr}}{R_{LCA,mean}}\right) + C_{LCA}R_{LCA,contr}\frac{dQ_{LCA}(t)}{dt} = \frac{P_{LCA}(t)-P_{LCA,out}}{R_{LCA,mean}} + C_{LCA}\frac{dP_{LCA}(t)}{dt} \quad (4.3).$$

This is a first-order differential equation where $Q_{LCA}(t)$ is the unknown function. For $R_{LCA,contr}$, was chosen the systole peak value during the contraction phase with a value of 2400 mmHg/(ml/min), as observed during the analysis performed in Section III. While $R_{LCA,mean}$ was the mean value of the resistance out of the contraction.

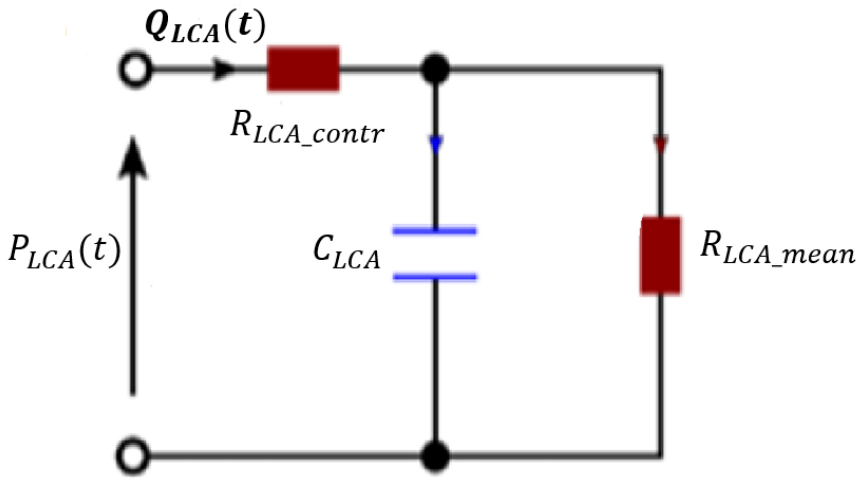

Figure 28: 3-element Windkessel model applied to the LCA during the myocardial contraction.

The estimated flow for the LCA, using the 2-element Windkessel model before and after the contraction phase and the 3-element Windkessel model during the contraction phase, is illustrated in Figure 29. The figure shows the estimated flow overlaid with the experimental flow, demonstrating the model's accuracy in capturing the LCA dynamics.

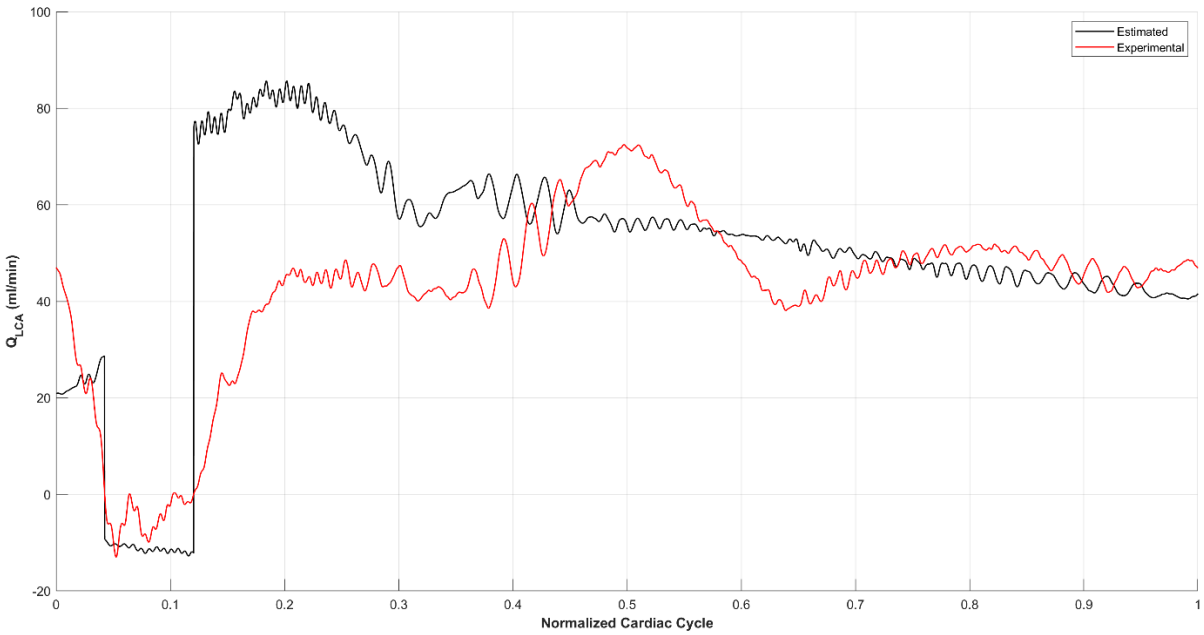

Figure 29: In black the estimated flow using the 2-element Windkessel model with the experimental flow in the right LCA during a cardiac cycle.

In Table 2 is provided aa summary of the resistances and compliances values used to estimate the outlet mass flow rate at the coronary arteries for the second simulation.

Table 2: The Windkessel Parameters used to estimate the mass flow rate in both coronaries.

LCA	Windkessel Model Parameters	Value
	$R_{LCA,mean}$	1.35 mmHg/(ml/min)
	$R_{LCA,contr}$	2400 mmHg/(ml/min)
	C_{LCA}	0.6 ml/mmHg
RCA	Windkessel Model Parameters	Value
	$R_{RCA,mean}$	2.17 mmHg/(ml/min)
	C_{RCA}	0.686 ml/mmHg

4.2 Fluent Solver: The Numerical Simulation

Once all the necessary information from the preprocessing stage was available, the numerical simulations could be executed using the Fluent Solver. A systematic approach was essential to ensure the simulations were implemented in a proper manner and had confrontable results. The key steps involved in this process are below outlined:

Boundary Conditions and Fluid Properties

The time-series data were introducing as boundary condition to accurately represent the transient nature of the simulation. As defined in the previous subsection this time-series inputs would allow for the dynamic changes in the boundary conditions throughout the simulation period. For the fluid needed to be introduced also the material properties also this explained in the previous subsection.

Convergence Criteria

The convergency criteria where strictly defined to ensure the accuracy and stability of the simulations, specifically focusing on residuals related to continuity and motion. These criteria are essential in numerical simulations to determine when the iterative solution process has sufficiently resolved the governing equation of the flow, ensuring that further iterations would not significantly alter the results. In both simulations, a residual threshold of 1e-2 was set for the mass conservation, while for momentum in the x, y, z coordinates, the residual tolerance was 1e-3. The momentum criteria are the one relative to solving the Navier-Stokes equation along the x, y and z direction. These criteria were selected based on the simulation's complexity and mesh intricacies. The lower the residuals are when the simulations run the more the solution is converging toward a steady state or a stabilized transient solution, while higher residuals suggest that the solution is still evolving significantly between iterations, potentially indicating that the convergence criteria have not been met.

Simulation Parameters

For the first simulation, 10400-time steps were performed, each with a time step of 0.0005 seconds and maximum 2 iterations per time step, in a simple or single physics simulation. A single physics simulations means that the algorithm solves only one type of physical phenomenon at a time. This setup resulted in a total simulation duration of 10400×0.0005 seconds. Similarly, for the second simulation consisted of 6240 time steps, also with a time step of 0.0005 seconds and maximum 250 iterations per time step, in coupled or multi-physics

simulation. A coupled simulation involves solving multiple interacting physical phenomena simultaneously. The total duration was of 6240×0.0005 seconds. The choice of this simulation parameters was to balance the computational efficiency with solution accuracy, taking into account the complexity of the simulations and desired level of temporal resolution.

Running the Simulations

Before starting the simulation, it was crucial to verify that all settings and parameters defined in the previous subsection (preprocessing) were correctly implemented in the Fluent. Both simulations where run in separate time and the results were saved at every 100-time steps. This periodic saving allowed for a detailed observation of the evolution of the model once the simulation was completed.

4.3 Post-Processing Analysis

With the simulations completed, the results of each simulation were thoroughly analyzed in CFD-Post 2024 R1, another tool within the Fluent Ansys 2024 R1 suite and MATLAB 2024a. Having chosen to run two simulations replication at least one cardiac cycle, an important amount of data was generated by each. For a proper analysis of the results, the simulated date from the second simulation were confronted with the experimental data. The feature considered for comparison of the results was the pressure time-series at the coronaries. Only for the second simulation pressure maps and flow profile in different planes along the geometrical model where obtained. In Figure 30 are reported in two different blue tonalities the planes used to present the results.

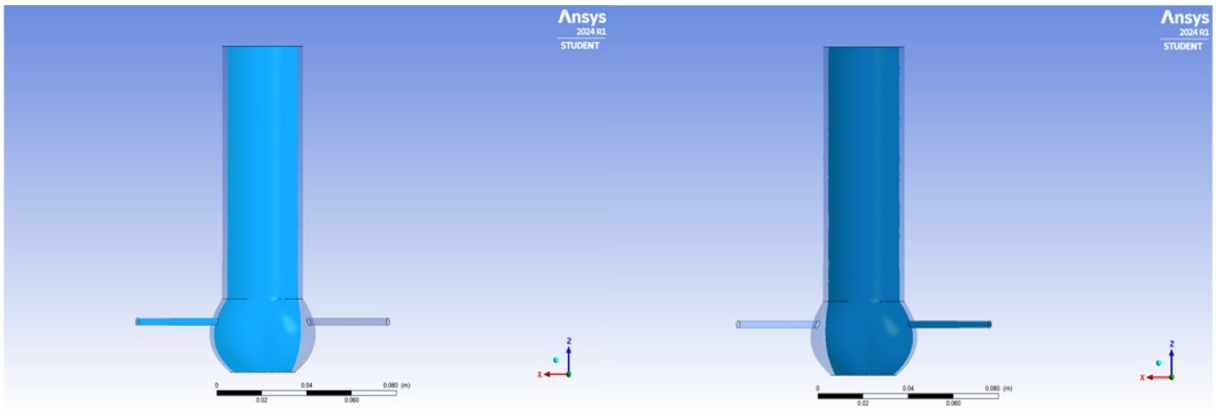

Figure 30:First Panel: Plane intersecting the geometry model, highlighting the RCA. Second Panel: Plane intersecting the geometry model, highlighting the LCA.

Pressure Profile

The pressure profile represents the temporal variation of pressure. In the RCA and LCA this quantity was not controlled at the solver level, allowing its values to be compared with the measured pressure values from the sensors during the experimental phase. For this a single cardiac cycle was considered.

Pressure Maps

The pressure maps were examined in two different planes within the geometry, with each plane was considered one of the coronaries at a time. Two different instants of time were chosen to observe how the pressure maps changed. for the RCA and LCA. The first-time instant was in correspondence of the systolic peak which was identified using Figure 28, where the first peak corresponds with 0.2 in the normalized cardiac cycle. The second time instant was during the diastole and exactly at time 0.6 of the normalized cardiac cycle (Figure 28).

Velocity Profile

In addition to the pressure maps, the velocity profiles were analyzed to gain a better understanding of the fluid dynamics in the ascending aortic tube. The velocity profiles were examined in the two planes used also for the pressure maps, in each plane was considered one of the coronaries at a time. Also. for the velocity profile the same time instants where considered.

4.3 Results

The mean pressure for the LCA and RCA obtained through computational modeling using the proposed boundary conditions (second simulation) were plotted together with pressure time series of the coronaries coming from the experimental data (Figure 31). In Figure 31, a single normalized cardiac cycle is considered, and the dashed line divides systole from the diastole. The pressure measured during the experiment for both coronaries is reported in red (LCA) and blue (RCA). As can be observed from the graphs, the pressure for both coronary arteries in the case of the experimental measurements rises sharply during systole, reaching a peak, and then gradually decreases during diastole. The same phenomenon is in details described in Section III (3.3).

The average pressure for the LCA obtained from the simulation using the proposed boundary conditions is shown in black, while the average pressure for the RCA is shown in green. The

pressure is expressed in mmHg, ranging from 0 to 144 mmHg. The experimental data for the LCA shows a significant increase in pressure during systole, peaking around the middle of this phase, followed by a gradual decrease during diastole. This trend is mirrored in the black line (average pressure LCA), although some discrepancies can be observed, indicating areas where the simulation may differ from the actual physiological measurements. There is a magnitude difference between the red and the black line that varies from 0 to 30 mmHg. While the green simulation line (average pressure RCA) exhibits minimal variations, staying in a range from 0.2 to 4 mmHg, around 0, throughout the entire cycle.

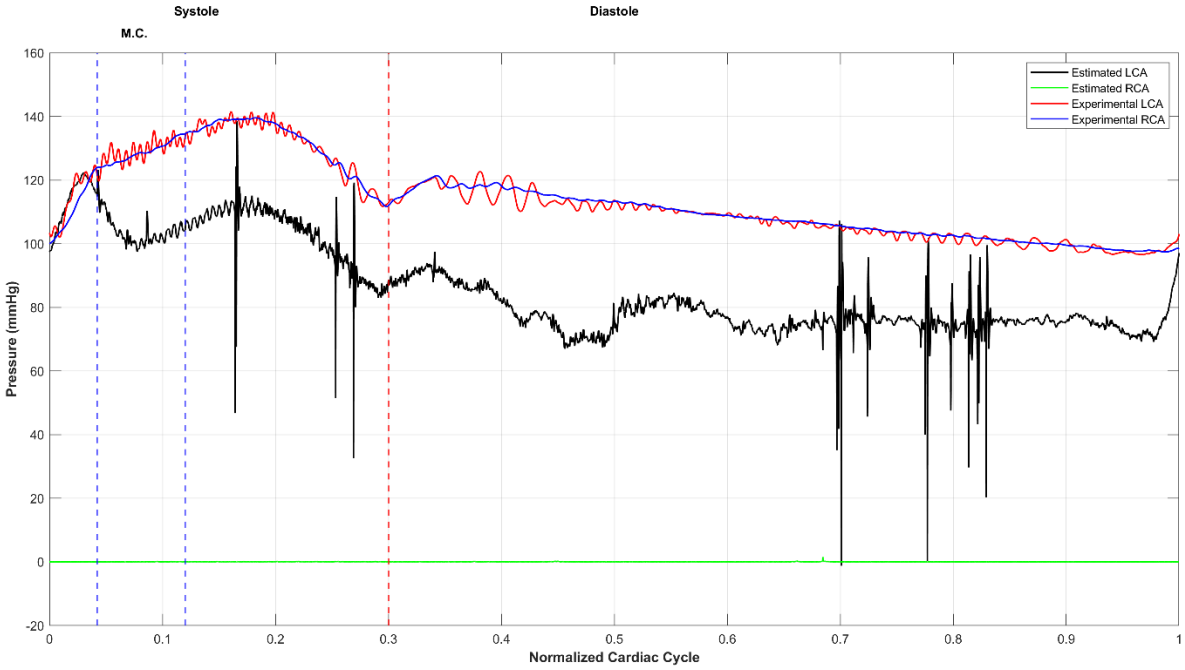

Figure 31: Pressure Profiles during a cardiac cycle. In red and blue the pressure from the experimental data for the LCA and RCA respectively. In black the estimated pressure in LCA with the proposed boundary conditions and in green the estimated pressure in RCA with the proposed boundary conditions. Red dashed line used to distinguish between systolic and diastolic phase and blue dashed lines used to restrict the myocardial contraction (M. C.) phase.

The study includes detailed pressure maps along planes intersecting the geometry, specifically focusing on regions containing one of the coronary arteries. Figure 32, Figure 33, Figure 34 and Figure 35 display these pressure maps, providing zoomed-in view in the coronary regions. Figure 32 and Figure 34 refer to the first plane that passes through the LCA, while Figure 33 and Figure 35 capture information from the second plane that passes through the RCA. Figure 32 and Figure 33 are synchronized to the same time step in the normalized cardiac cycle to systole peak exactly at time 0.2 (as illustrated Figure 31). On the other hand, Figure 34 and Figure 35 are taken at time step which falls in the diastolic phase, specifically at time 0.6 in the normalized cardiac cycle. Each of these four figures is divided into two panels:

- the upper panel presents a broader range of pressure values, spanning from 6180 Pa to 15150 Pa.
- the lower panel is focused on a narrower range of pressure values, specifically from 11310 Pa to 15150 Pa, highlighting the dominant pressure values in that range. this to emphasis the dominant pressure values.

These figures help in comparing the pressure maps at identical time instant between the two coronary tubes. Additionally, it can be examined how the pressure maps vary within the same coronary in these two different time steps that correspond to different phases of the cardiac cycle. Their comparison could provide insights into the dynamics and distribution of pressures within the coronary arteries.

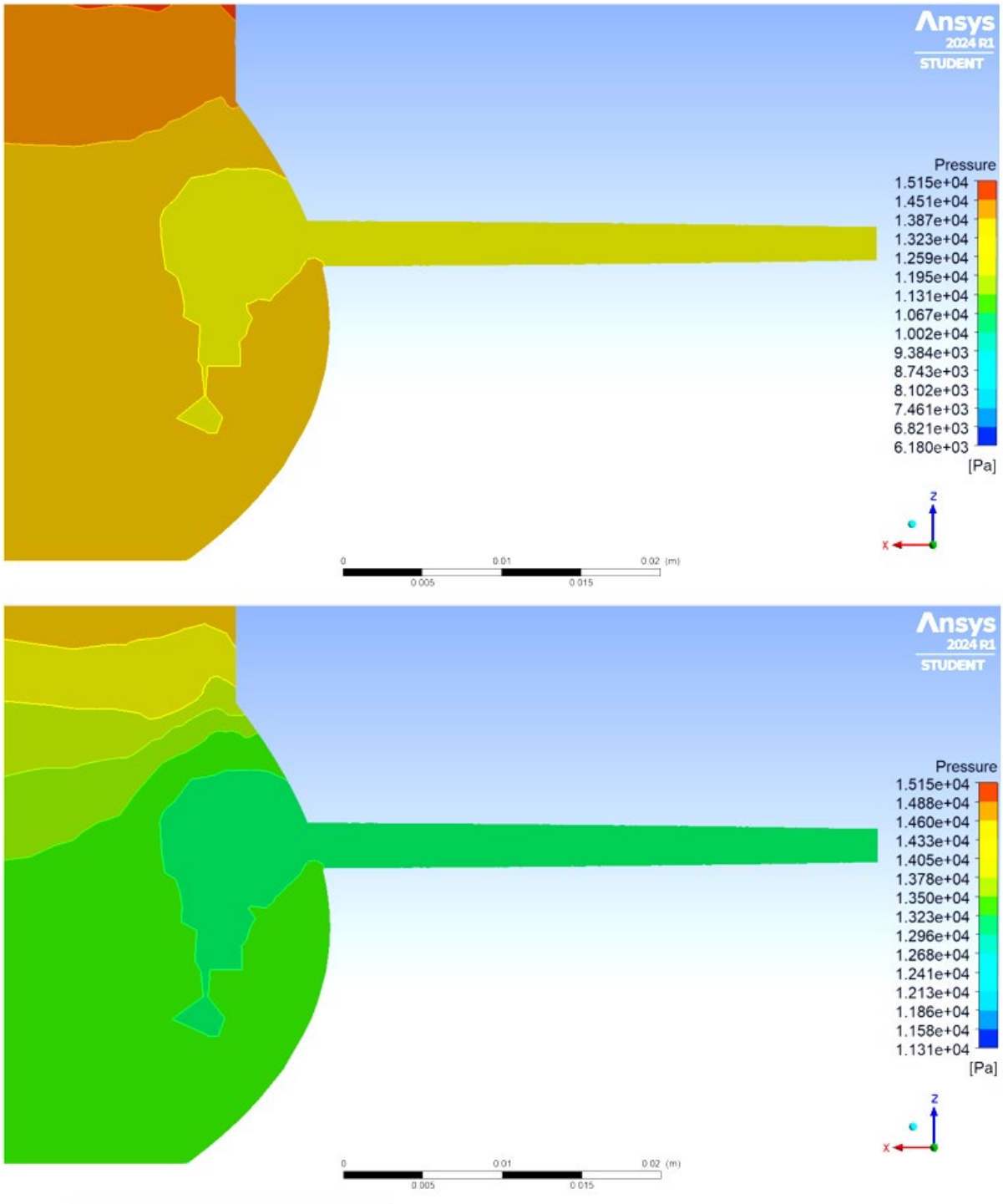

Figure 32: Both panels represent the pressure maps at time 0.2 of the normalized cardiac cycle, along the first plane, zoomed in on the area corresponding to the LCA. The upper panel shows the pressure map with a range varying from 6180 Pa to 15150 Pa. In the lower panel, the same pressure map region is shown but within a more concentrated range, from 11310 Pa to 15150 Pa.

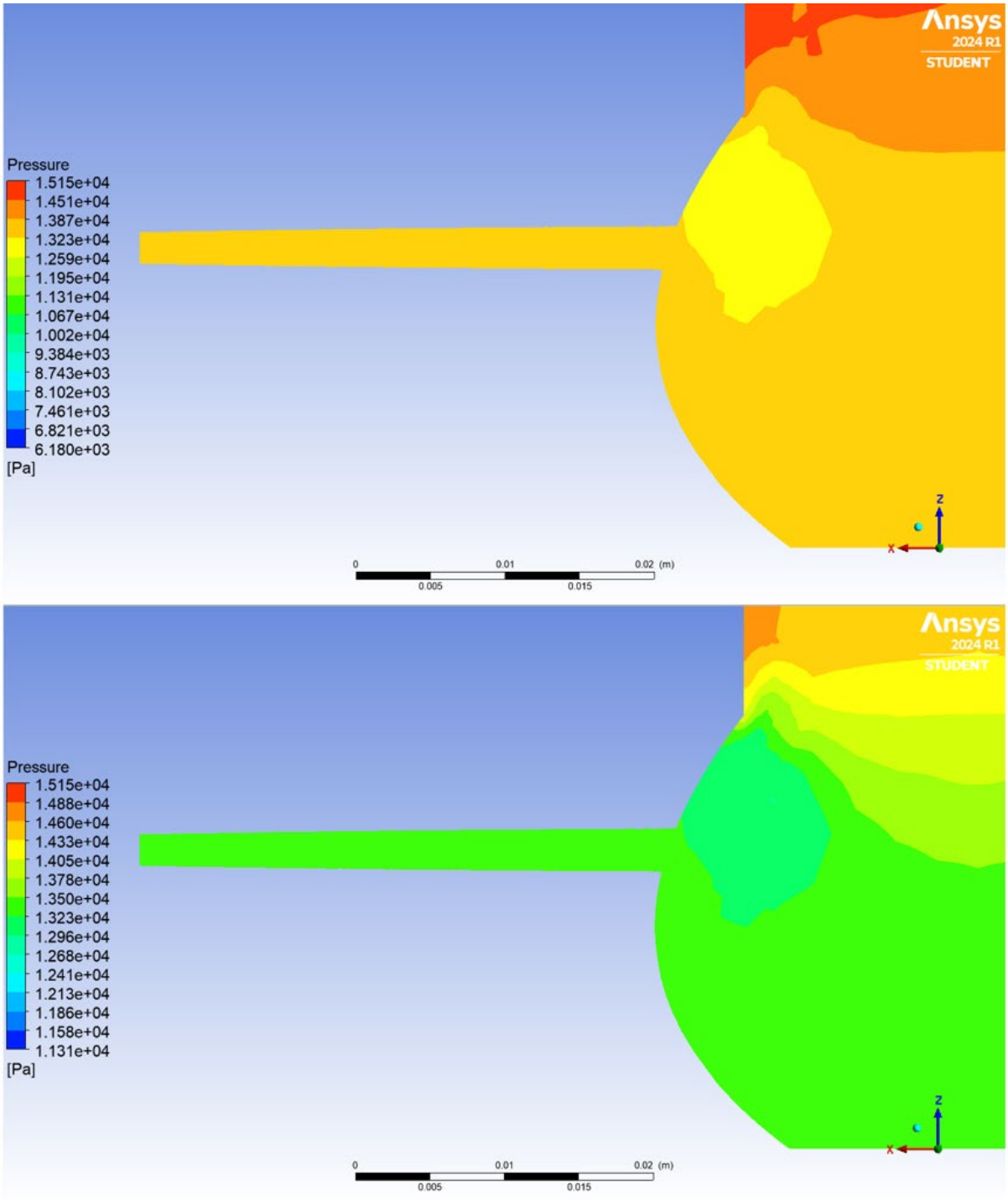

Figure 33: Both panels represent the pressure maps at time 0.2 of the normalized cardiac cycle, along the second plane zoomed in on the area corresponding to the RCA. The upper panel shows the pressure map with a range varying from 6180 Pa to 15150 Pa. In the lower panel, the same pressure map region is shown but within a more concentrated range, from 11310 Pa to 15150 Pa.

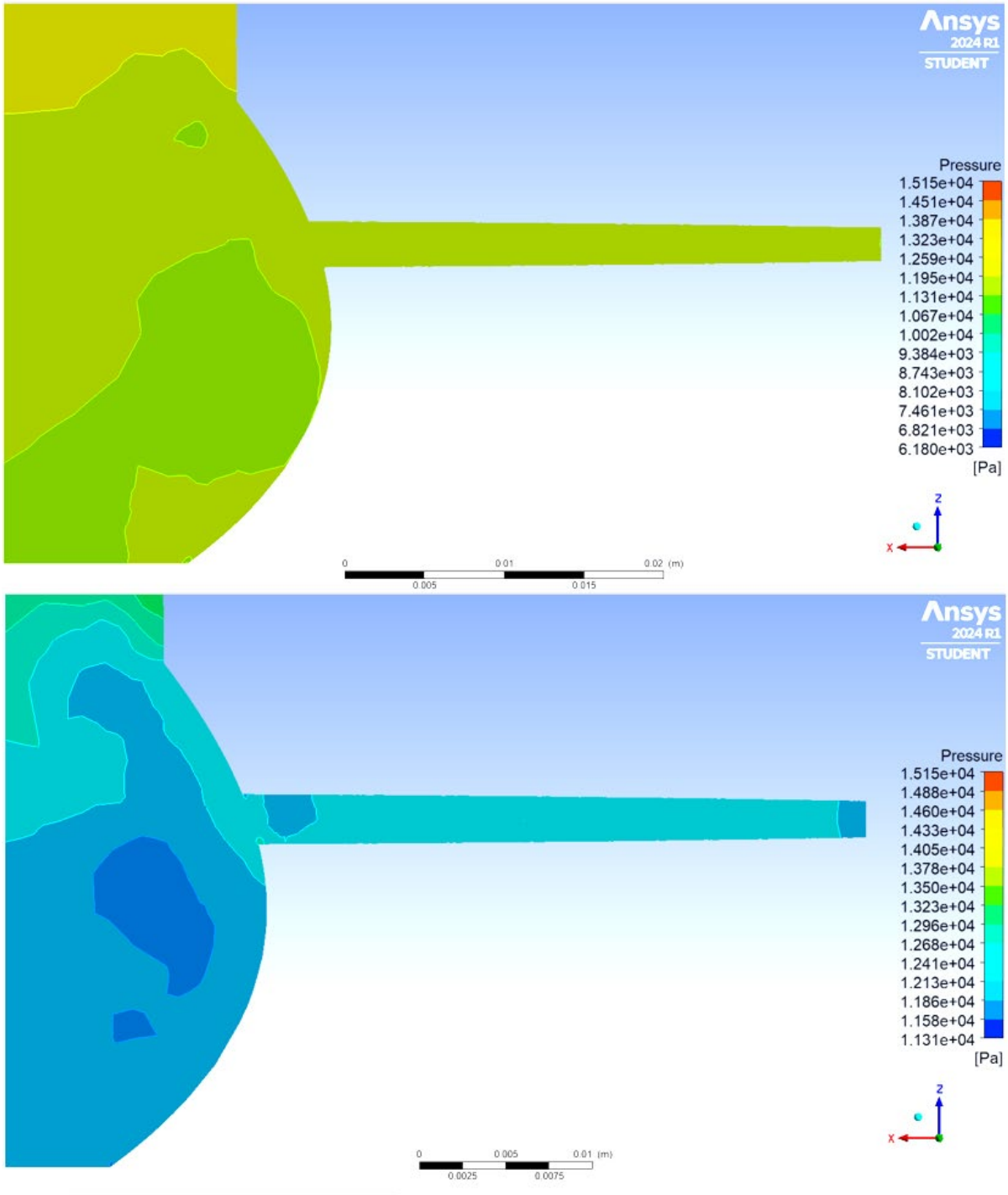

Figure 34:Both panels represent the pressure at time 0.6 of the normalized cardiac cycle, along the first plane zoomed in on the area corresponding to the LCA. The upper panel shows the pressure map with a range varying from 6180 Pa to 15150 Pa. In the lower panel, the same pressure map region is shown but within a more concentrated range, from 11310 Pa to 15150 Pa.

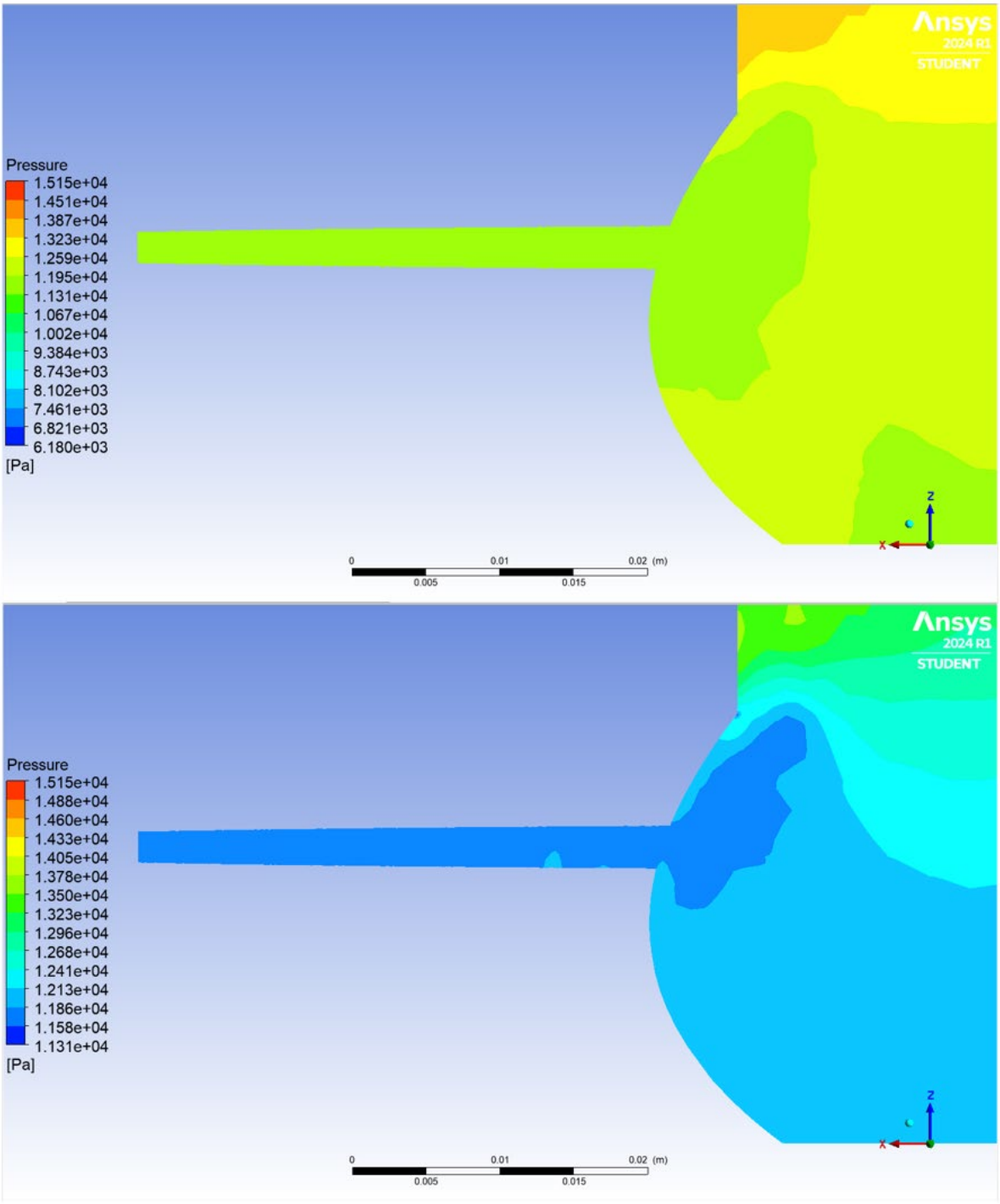

Figure 35:Both panels represent the pressure maps at time 0.6 of the normalized cardiac cycle, along the second plane zoomed in on the area corresponding to the RCA. The upper panel shows the pressure map with a range varying from 6180 Pa to 15150 Pa. In the lower panel, the same pressure map region is shown but within a more concentrated range, from 11310 Pa to 15150 Pa.

Another interesting result was the velocity profile along the same planes intersecting the geometry for the pressure maps, again focusing on the regions containing one of the coronary arteries. Figure 36, Figure 37, Figure 38 and Figure 39 display these velocity profiles, providing zoomed-in view in the coronary regions. Figure 36 and Figure 38 refer to the first plane that passes through the LCA, while Figure 37 and Figure 39 capture information from the second plane that passes through the RCA. Figure 36 and Figure 37 are synchronized to the same time step, corresponding to time step 0.2 of the normalized cardiac cycle as it was mentioned in the pressure maps. While, Figure 38 and Figure 39 are taken at time step 0.6 of the normalized cardiac cycle. Each of these four figures is divided into two panels:

- the upper panel presents a broader range of velocity values, going from 0 to 4.01 m/s.
- the lower panel is focused on a narrower range of pressure values, specifically from 0 to 0.3 m/s, this because in the coronaries the velocity of the flow is low and to better observe it a smaller range of values has to be considered.

Similar to the pressure maps, these velocity profiles facilitate comparisons of velocities at identical time instant between the two coronary tubes. Additionally, they allow examination on how these velocities change on the same coronary but in two different time instants of the normalized cardiac cycle. It is worth noticing that all velocity profiles have been overlaid tangential vectors to the plane, showing the direction and orientation of velocity vectors. This approach enables analysis of velocity as a vectorial quantity, providing insights beyond just magnitude, as depicted in the profiles.

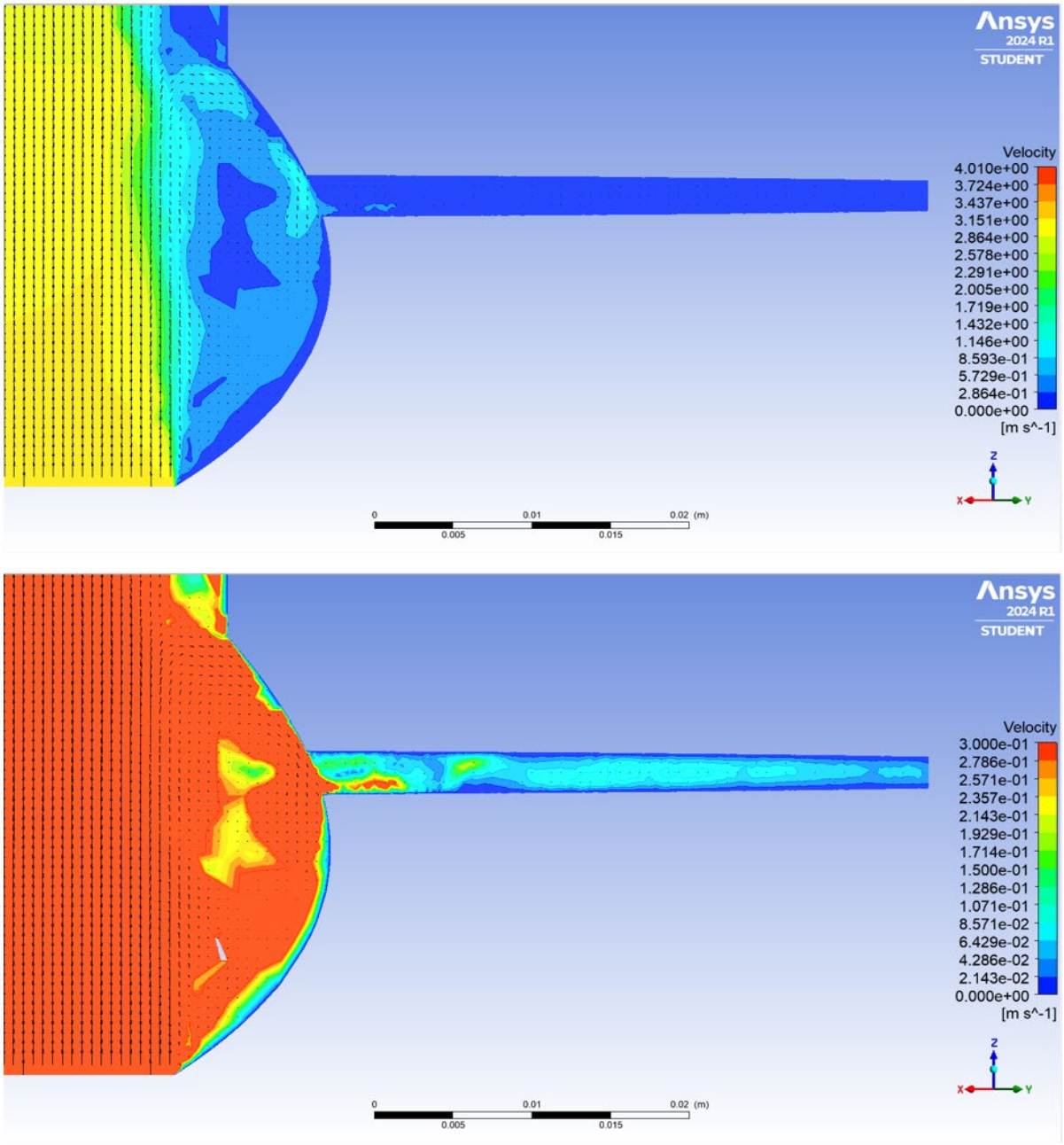

Figure 36: Both panels represent the velocity profile at time 0.2 of the normalized cardiac cycle, along the first plane zoomed in on the area corresponding to the LCA. The upper panel shows the velocity with a range varying from 0 to 4.01 m/s. In the lower panel, the same velocity region is shown but within a more concentrated range, from 0 to 0.3 m/s.

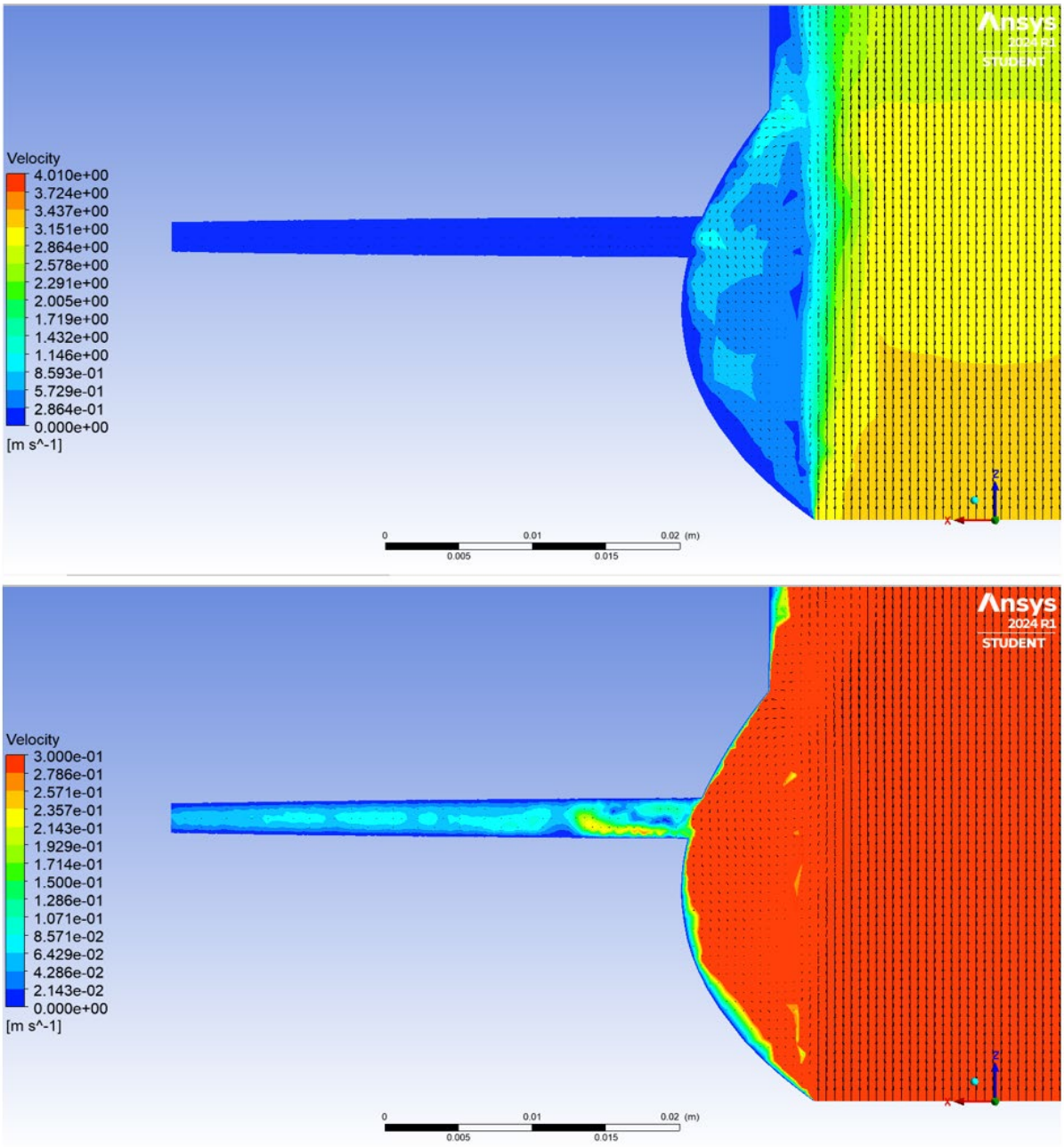

Figure 37: Both panels represent the velocity profile at time 0.2 of the normalized cardiac cycle, along the second plane zoomed in on the area corresponding to the RCA. The upper panel shows the velocity with a range varying from 0 to 4.01 m/s. In the lower panel, the same velocity region is shown but within a more concentrated range, from 0 to 0.3 m/s.

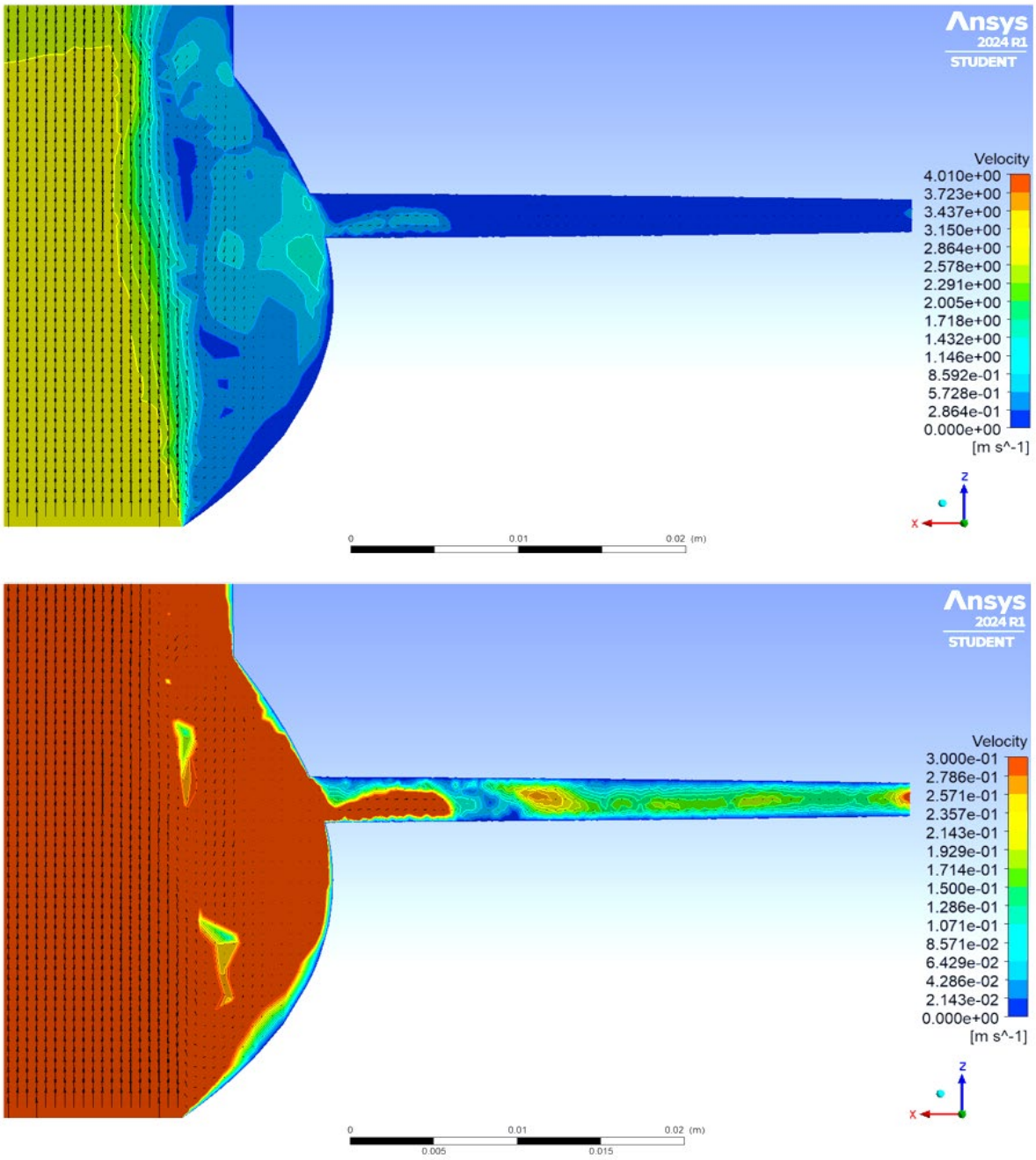

Figure 38: Both panels represent the velocity profile at time 0.6 of the normalized cardiac cycle, along the first plane zoomed in on the area corresponding to the LCA. The upper panel shows the velocity with a range varying from 0 to 4.01 m/s. In the lower panel, the same velocity region is shown but within a more concentrated range, from 0 to 0.3 m/s.

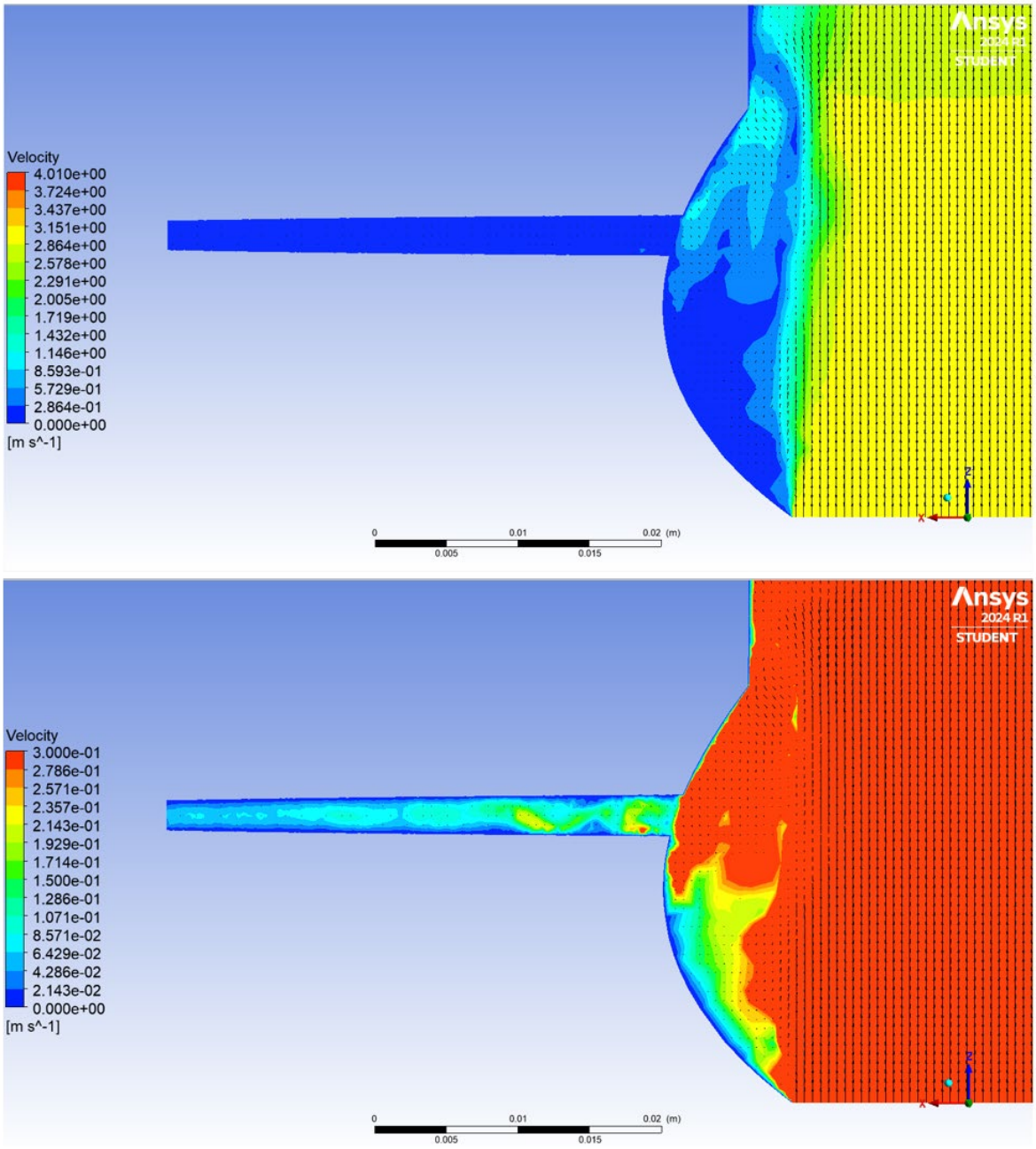

Figure 39: Both panels represent the velocity profile at time 0.6 of the normalized cardiac cycle, along the second plane zoomed in on the area corresponding to the RCA. The upper panel shows the velocity with a range varying from 0 to 4.01 m/s. In the lower panel, the same velocity region is shown but within a more concentrated range, from 0 to 0.3 m/s.

4.4 Discussion and Interpretation

The study's findings offer critical insights into the hemodynamics of coronary arteries, particularly focusing on the simulation accuracy of pressure and flow dynamics using a Windkessel model to estimate the boundary conditions at the coronary artery. This section discusses the comparison between experimental and simulated data, the implications of the observed discrepancies, and the potential for further refinement of the computational model. It also gives glimpses on how the pressure maps and velocity profiles are interpreted in two different time instants of the cardiac cycle.

In Figure 31, a graphic comparison was performed between the experimental pressure data measured in the laboratory and the simulated average pressure dynamics using mass flow rate estimated from the Windkessel model as boundary conditions for the coronaries. For the simulation were used constant resistance parameters to parameterize flow dynamics, as detailed in subsection 3.3.

A notable observation from Figure 31 is essentially the presence of around zero pressure at the RCA outlet, a critical aspect influenced by how resistance was defined for the RCA within the model. The simulation reveals a distinct pressure wave propagating upstream and a constant pressure wave downstream. During the resistance definition phase by analyzing the pressure gradient across the coronary arteries, it was thought that such difference in pressure was the one driving the fluid flow. However, it becomes evident that the pressure gradient which derives the flow in the numerical simulation is not given by the same absolute pressure measured in the experiments. This suggest that for the RCA, once the resistance parameter is accurately characterized, the necessity of knowing the reference outlet pressure diminishes, being the solution affected by the pressure gradient only.

While for what concerns the LCA outlet within the context of Figure 31, employing two Windkessel models for flow estimation shows simulated pressure closer to the experimental one even though with some discrepancies as described in the results section and a gap between the two patterns of around 30 mmHg. Notably, simulated pressure profiles at the beginning and end of the cardiac cycle closely match experimental observations. Like in the RCA, also in this case the pressure gradient which derives the flow in the numerical simulation is not given by the same absolute pressure measured in the experiments. Although in the case of LCA the obtained results are nearer to the experimental data, it means that the results are partially affected.

It is important to say that the evaluation of the flow using a Windkessel model, reveals unexcepted (Figure 31) findings. The simulation pressure reflects the reference pressure gradient and not the actual measured pressure value that was expected. This is a pure consequence of how the flow dynamics are parameterized. And as also explained for the RCA but this in reality is valid for both the coronary tubes the parametrization of the flow emphasizes the role of upstream pressure variations over downstream pressures in determining coronary flow patterns.

In summary, Figure 31 provides critical visual insights into simulated and experimental pressure dynamics in coronary arteries. Discrepancies between simulated outputs and experimental data underscore the ongoing need for refining model parameters and boundary conditions. Despite this is a good preliminary outcome in utilizing the Windkessel model to estimate boundary conditions, further improvements are essential to enhance simulation accuracy in replicating intricate pressure variations observed during the cardiac cycle.

Figure 32 and Figure 33 provide a detailed comparison of the pressure for both coronary at a time step corresponding to the systolic peak. For both the color map ranges from light green to orange and dark orange which reveal more subtle differences in pressure, particularly the pressure is concentrated medium to higher-pressure values for the indicated range. This consistent color scheme across both the upper and lower panels facilitates an easier comparison between different views and regions.

In the upper panels is given a macro-level prospective, which allows to have a look on the overall trend of pressure and how the major gradient evolves. In this specific case between the LCA and RCA there is not a visual difference while the lower-level views pinpoint to a smaller range of pressure to pinpoint specific areas of interest within the LCA, even though there are no major changes to catch attention. This similarity is supported from what is observed in the experimental data shown in Figure 31 (experimental data for LCA and RCA), where the pressure profiles for both arteries were overlaid and demonstrated comparable systolic peak values and patterns.

Shifting focus to Figure 34 and Figure 35, which represent the pressure profiles during the diastolic phase, the pressure maps show overall lower values compared to systole, with the color range shifting from light blue to green. This change is physiologically expected, as pressures typically decrease during diastole. It is interesting to notice in the lower panels that in the LCA a lower pressure is indicated with light blue than in the RC.

When comparing the LCA at two different time instants (systole in Figure 32 and diastole in Figure 34), the pressure range is evidently higher during systole, as shown by the color distribution. This observation aligns with the physiological expectation that pressures peak during systole and decrease during diastole. The same pattern is observed for the RCA when comparing (Figure 33, systole and Figure 35, diastole). In brief comprehensive visual and comparative analysis of Figure 32 and Figure 33 (during systole) and Figure 34 and Figure 35 (during diastole) offers essential insights into the pressure dynamics within the LCA and RCA.

The final but equally important results pertain to the velocity profiles along the same planes used for the pressure maps. These velocity profiles reveal how the flow velocity varies in different regions of the geometry at the same time instant. Similar to the pressure maps, we examine the coronary velocity profiles at two specific time points: once during the systolic peak (Figure 36 and Figure 37) and once during the diastolic phase (Figure 38 and Figure 39).

During the systolic peak, as shown in Figure 36 and Figure 37 , it is notable that the upper panels indicate a flow velocity that is nearly zero across both coronary arteries. However, the lower panels provide a more detailed view, revealing that there is indeed some flow, albeit minimal. In the LCA, the flow velocity can reach up to 0.3 m/s. This is not the case in the RCA, where the velocities are generally lower, but still fall within the range of 0.1 m/s to 0.3 m/s, which is expected for a healthy resting subject. This behavior aligns well with the physiological conditions being simulated. The same pattern holds true during the diastolic phase, as illustrated in Figure 38 and Figure 39.

Additionally, it is valuable to compare the velocity profiles for each coronary artery at different time instants. For the LCA, this involves examining the velocity profiles in Figure 36 and Figure 38 and for the RCA the velocity profile Figure 37 and Figure 39. Observing the lower panels of these figures, it becomes apparent that during the diastolic phase, both coronary arteries exhibit higher flow velocities than during the systolic phase. This is a crucial physiological insight, as it aligns with the expectation that coronary flow decreases during systole due to the contraction of the heart muscle, which increases pressure and restricts flow. Conversely, during diastole, the heart muscle relaxes, resulting in lower pressure and higher flow velocities.

This observed trend is consistent with the pressure maps previously discussed, where higher pressures during systole were noted due to the heart's contraction, leading to reduced flow. In contrast, the diastolic phase, characterized by lower pressure, allows for greater flow through

the coronary arteries. This cyclical variation in pressure and flow is essential for maintaining the physiological function of the heart, ensuring that adequate blood supply is delivered during each phase of the cardiac cycle.

In summary, the analysis of the velocity profiles alongside the pressure maps provides a comprehensive understanding of the hemodynamic behavior within the coronary arteries. These findings not only validate the accuracy of the simulation model in replicating physiological conditions but also highlight the intricate balance between pressure and flow that governs coronary artery function.

Conclusion

In conclusion, this work has aimed to develop a computational model that replicates the hemodynamics of the coronary arteries, leveraging experimental data to parameterize resistance at the coronaries for an accurate simulation. Through meticulous exploration of the coronary physiology and fluid dynamics modeling techniques, particularly employing the 2-element and 3-element Windkessel models, it was possible to establish a robust framework capable of simulating intricate flow pattern within coronary arteries.

The use of the in vitro model experimental data provided starting point for the quantitative resistance evaluation in the coronary arteries across important phases of the cardiac cycle. Specifically, the R_{LCA} mean value was 1.35 mmHg/(ml/min) during diastole and 2400 mmHg/(ml/min) during systole, whereas the R_{RCA} for the whole cardiac cycle, had a mean value equal to 2.17 mmHg/(ml/min). This values where used to parameterize the flow at the coronaries.

Validation of this computational model involved comparing simulations directly utilizing experimental time series data against those employing the Windkessel models with the derived resistance parameters. Although minor discrepancies were observed in the replication of outlet pressure at the coronaries, attributable to the dynamic nature of flow governed by pressure gradients and influenced by the way the resistance where modeled, the approach effectively captured critical hemodynamic structures within the Valsalva sinuses and coronary arteries.

In summary, this research underscores the significance of utilizing Windkessel-type boundary conditions based on real pressure measurements to enhance the accuracy and reliability of cardiovascular simulations. Future research efforts should focus on refining resistance parameterization methods and integrating additional physiological complexities to further improve model fidelity and practical applicability. Ultimately, this thesis provides valuable insights into coronary artery hemodynamics and the pivotal role of fluid resistance parameterization in simulation studies.

References

Abdolrazaghi, M. N. (2010). “Mathematical Modelling and Electrical Analog Equivalent of the Human Cardiovascular System”. *Springer Science+ Business Media, 10*, 45-51.

Alzhanov, N. N. (2023). “CFD Computation of Flow Fractional Reserve (FFR) in Coronary Artery Trees Using a Novel Physiologically Based Algorithm (PBA) Under 3D Steady and Pulsatile”. *MDPI Bioengineering, 10*(3).

Ansys. (n.d.). Retrieved from Fluids, CFD: https://www.ansys.com/products/fluids

BMJ. (2005). Retrieved April 4, 2023, from Biomedical Models and Healthcase Systems: https://10.1136/bmj.330.7488.419-a

Cao, H. L. (2021). “Hemodynamic Charcteristics of Patients with Suspected Coronary Heart Disease at Their Initial Visit”. *Front. Physiol., 12*.

Centers for Disease Control and Prevention. (2024). Retrieved May 7, 2024, from Coronary Artery Disease (CAD): https://www.cdc.gov/heartdisease/coronary_ad.htm#print

Chemla, D. H. (1998). "Total arterial compliance estimated by stroke volume-to-aortic pulse pressure ratio in humans". *American Journal of Physiology-Heart and Circulatory Physiology, 274*(2), H500-H505.

Chen, H. G. (2016). “Microstructure-Based Biomechanics of Coronary Arteries in Health and Disease,”. *J Biomech., 49*(12), 2548-2559.

Chen, H. G. (2016). “Microstructure-Based Biomechanics of Coronary Arteries in Health and Disease,”. *J Biomech., 49*(12), 2548-2559.

Claes, E. M. (2010). “Mechanical Properties of Human Coronary Arteries". *E. Claes, J.M. Atienza, G.V. Guinea, F.J. Rojo, J.M. Bernal, J.M. Revuelta and M. Elices, “Mechanical Propert Proceedings of the 32nd Annual International Conference of the IEEE Engineering in Medicine and Biology Society (EMBC)*, (pp. 100-105). Buenos Aries, Argentina.

Doeblin, E. (1998). *System Dynamics: Modeling, Analysis, Simulation, Design.* CRC Press.

Downey, J. M. (1975). “Inhibition of coronary blood flow by a vascular waterfall mechanism”. *36*, 753-760.

FitzHugh, R. (1961). "Electrical Models of Excitable Cells: From Basic Electrophysiology to Mathematical Modeling". *Physiological Reviews, 41*(3), 395-396.

Ghasemalizadeh, O. M. (2014). “Exact Modeling of Cardiovascular System Using Lumped Method”. *arXiv*.

Ghitti, B. T. (2020). “Nonlinear Lumped-Parameter Models for Blood Flow Simulations in Networks of Vessels.”. *ESAIM: Mathematical Modelling and Numerical Analysis, 56*(5), 1579-1672.

Gjika, M. (2022). Variazione dei Segnali Respiratorio e Electtrocardiografico dovuto all'Asma. *Thesis, Laurea Triennale in Ingegneria Biomedica,Universita Politecnica delle Marche* .

Goodwill, A. G. (2018). “Regulation of Coronary Blood Flow”. *Compr. Physiol.*, 321-382.

Gregg, D. E. (1937). "Phasic blood flow and its determinants in the right coronary artery.". *American Journal of Physiology-Legacy Content*, 580-588.

Hoffman, J. B. (1976). “Transmural variations in myocardial perfusion”. *Prog Cardiol., 5*, 37-89.

Jørgensen, L. H. (n.d.). *"Cardiovascular Biomechanics."*. Norwegian University of Science and Technology. Retrieved 06 15, 2024, from https://folk.ntnu.no/leifh/teaching/tkt4150/._main026.html.

Keramati, H. A. (2023). “Using Gaussian process for velocity reconstruction after coronary stenosis applicable in positron emission particle tracking: An in-silico study". *PLOS ONE*.

Kim, H. J.-C. (2010). “Patient- Specific Modeling of Blood Flow and Pressure in Human Coronary Arteries”. *Annals of Biomedical Engineering, 38*(10), 3195-3209.

Klabunde, R. E. (2011). *Cardiovascular Physiology Concepts, 2nd edition.* Lippincott Williams & Wilkins .

Koeppen, B. S. (2010). “Regulation of heart ans vasculature”. In *Berne and Levy Physilogy 6th edition* (pp. 370-392).

Libby, P. T. (2005). “Pathophysiology of Coronary Artery Disease”. *American Heart Association*.

Loukas, M. A. (2013). “The Clinical Anatomy of the Coronary Arteries”. *J. Cardiovasc. Trans. Res.*, 197-207.

Mirramezani, M. D. (2019). “Reduced Order Models for Transstenotic Pressure Drop in the Coronary Arteries”. *J Biomech Eng, 141*(3), 031005(11).

Morris, P. D.-K. (2016). “Computational fluid dynamics modelling in cardiovascular medicine”. *Heart, 102*, 18-28.

Mousavi, S. M. (15/09/2024-18/09/2024b). “In Vitro Study of Coronary Artery Distal Resistance”.

Mousavi, S. M. (2024a). “Experimental and Numerical Investigations in Sport-Related Cardiac Death.”. *Ph. D. dissertation, Polytechnic University of Marche, Ancona*.

Mukherjee, P. R. (2022). “Role of animal models in biomedical research:a review”. *Laboratory Animal Research*.

Netter, F. H. (2014). *Atlas of Human Anatomy, 6th edition.* Elsevier.

Niederer, S. A. (2019). “Computational models in cardiology”. *Nat Rev Cardiol., 16*(2), 100-111.

Niederer, S. A. (2019). “Computational models in cardiology”. *Nat Rev Cardiol., 16*(2), 100-111.

Obrova, J. S. (2022). “Sudden cardiac death – a known unknown?”. *Biomed Pap Med Fac Univ Palacky Olomouc Czech Repub., 166*(3), 258-266.

Pirola, S. (2019). “Patient-Specific Analysis of the Hemodynamic Performance of Surgical and Transcatheter Aortic Valve Replacements.” . *Imperial College London*.

Prinz, A. E.-P. (2023). “Models, systems, and descriptions A cross- disciplinary reflection on models". *Front. Comput. Sci., 5*, 1-19.

Romagnoli, S. (2022). Mechanoelectric phenomena contributing to sport-related sudden cardiac death. *Thesis, Corso di Laurea Magistrale in Biomedical Engineering*.

Saldin, K. (2018). Anatomy & Physiology: The Unity of Form and Function, 8th edition. *McGraw-Hill Education*.

Saxton, A. C. (2023). *Anatomy, Thotax, Heart Right Coronary Arteries.* StatPearls.

Segel, L. A. (1989). "Mathematical Models in Medicine: A Review". *SIAM Review, 31*(4), 591-634.

Seligman, H. N. (2022). "Phasic flow patterns of right versus left coronary arteries in patients undergoing clinical physiological assessment". *EuroIntervention, 16*, 1260-1270.

Stanfield, C. L. (2012). *Principals of Human Physiology, 5th edition.* Pearson.

Taegtmeyer, H. H. (2006). “Coronary blood flow and oxygen delivery to the heart in health and disease”. *J. of the American Society of Hypertension, 1*(1), 7-15.

Tortora, G. J. (2017). *Principles of Anatomy and Physiology, 15th edition.* Wiley.

Versteeg, H. K. (2007). *An Introduction to Computational Fluid Dynamics – The finite volume method 2nd.* Pearon Education Limited.

Vynnycky, E. W. (2010). *An Introduction to Infextious Disease Modelling.* Oxford University Press.

Wang, H. L. (2015). "In Vitro Models in Biomedical Research: Advantages and Limitations". *Experimental and Therapeutic Medicine, 9*(3), 707-711.

West, P. H. (2017). "Computational Models in Medicine: An Overview". *Philosophical Transactions of the Royal Society A: Mathematical, Physical and Engineering Sciences, 375*(2109).

Westerhof, N. E. (1971). “An Artificial Arterial System for Pumping Hearts.”. *Journal of Applied Physiology, 31*(5), 76-81.

Westerhof, N. S. (2010). "Snapshots of Hemodynamics: An Aid for Clinical Research and Graduate Education". *Springer Science & Business Media*.

White, F. M. (2005). *Viscous Fluid Flow, 3rd edition.* McGraw-Hill Mechanical Engineering.

Wikipedia. (2024, 05 20). Retrieved from Computational Fluid Dynamics.

Yartsev, A. (2013). “Coronary blood flow". *Deranged Physilogy CIMC Primary Exam Cardiovascular system*.

Zhang, Y. L. (2017). "Imaging-Based Computational Modeling in Bioengineering". *Computational and Mathematical Methods in Medicine*.

Zhonghua, S. L. (2014). “Computational fluid dynamics in coronary artery disease”. *Computerized Medical Imaging and Graphics, 38*(8), 651-663.

Zitti, G. M. (2023). Cardiac and Vascular Modeling in Sport. In L. C. Burattini, *The Bioengineering of Sport* (pp. 171-188). Bologna: Patron.

Acknowledgment

I would like to express my sincere gratitude to all those who have contributed to the completion of this thesis.

Firstly, I am deeply grateful to my advisor, Professor Gianluca Zitti, for his unwavering support during the planning and execution of this thesis. His dedication and guidance through every step of this process have been invaluable. I also want to thank him for the opportunity he provided by securing me an internship abroad, which greatly enriched my research experience.

I extend my heartfelt thanks to my first co-advisor, Professor Laura Burattini, for her support not only during the thesis but throughout my entire Master's Program. Her advice and guidance have always been crucial to me.

Lastly, I would like to thank my second co-supervisor, Dott. Seyyed Mahmoud Mousavi, for his support, availability, and willingness to assist me whenever needed, in addition to providing the experimental model data that were important for my research.

To all of you, my most sincere and profound thanks.